Satellite Moisture Profiling of the Tropical Eastern Pacific Convergence Zone

by
Christopher E. Lietzke

Department of Atmospheric Science
Colorado State University
Fort Collins, Colorado

Colorado State University

Department of Atmospheric Science

Paper No. 646

SATELLITE MOISTURE PROFILING OF THE TROPICAL EASTERN PACIFIC CONVERGENCE ZONE

by

Christopher E. Lietzke

Department of Atmospheric Science

Spring 1998

ABSTRACT OF DISSERTATION

SATELLITE MOISTURE PROFILING OF THE
TROPICAL EASTERN PACIFIC CONVERGENCE ZONE

Tropospheric relative humidity profiles and cloud water information retrieved from satellite observations along with other climate analyses are used to study the evolutionary structure of the intertropical convergence zone during the boreal spring. First, the effectiveness of combining satellite observations from an infrared imager, the Geostationary Operational Environmental Satellite-8, with a microwave moisture sounder, the Special Sensor Microwave/Temperature-2, to retrieve water vapor profiles and cloud properties is evaluated. Retrieved water vapor profiles are compared to radiosonde measurements to assess the overall performance of a microwave sounder based retrieval system with and without the addition of infrared radiances. The addition of infrared radiances improves the accuracy of the water vapor profile retrieval over land in cloudy skies, however, no increase in retrieval performance was realized over the ocean. The temporal variability of radiosonde humidity measurements is shown to be large for many of the collocated cases, indicating that the value of the comparisons in many cases is inadequate.

The algorithm was then used to retrieve relative humidity profiles and cloud water path from microwave moisture sounder observations over the central and eastern tropical Pacific ocean. These data, along with other observational and model analyses, are used to study the moisture profile and cloud structure of the intertropical convergence zone

during the boreal spring. For a limited period during the boreal spring, the intertropical convergence zone is observed to form two troughs quasi-symmetrically situated about the equator, but only during years when the sea surface temperature on the equator is cold. The presence or absence of the equatorial cold tongue in the sea surface temperature field is observed to be the determining factor in the formation of a double intertropical convergence zone in the eastern Pacific. The forcing mechanisms for atmospheric convection in the tropical Pacific are discussed. During the equinoctial periods, it is shown that sea surface temperature is the controlling mechanism in the eastern Pacific, whereas large scale low level mass divergence is the controlling mechanism in the western Pacific.

ACKNOWLEDGEMENTS

This research was funded by the Center for Geosciences, Phase II at CIRA/CSU under Department of Defense grant #DAAH04-94-G-0420 and by NASA grant #NAG5-3449.

TABLE OF CONTENTS

LIST OF TABLES

LIST OF FIGURES

1 Introduction

The earth's climate system is primarily controlled by ocean-atmosphere interaction in the tropics. Much research has been accomplished in order to better understand the effects of the tropical ocean-atmosphere circulation on the earth's weather and climate. For most of the year, the source of the thermally direct atmospheric circulation, the intertropical convergence zone (ITCZ), forms in a single band encompassing the earth. For a short period of time during the boreal vernal equinox, the ITCZ has been observed to form in two distinct bands, quasi-symmetrically situated about the equator in the tropical eastern Pacific. This infrequent annual occurrence is used to study the effects of air-sea interaction on atmospheric convection. The spatial and temporal evolution of the eastern Pacific intertropical convergence zone is investigated using a variety of climate data. In order to describe the vertical structure of the moisture and cloud water profile in the region, it was necessary to produce a new data set. Profiles of relative humidity and cloud liquid and ice water were retrieved from satellite observed microwave radiances.

A need for further research in moisture profiling remote sensing and its application to better quantify hydrologic processes in data sparse regions is given in this chapter. A description of the retrieval algorithm and its evaluation follow in chapters 2 and 3. The data set produced to better study the intertropical convergence zone is described in chapter 4. An analysis of the intertropical convergence zone in the eastern Pacific using observations is given in chapter 5. Chapter 6 evaluates the observations and presents a hypothesis regarding the important mechanisms forcing atmospheric convection in the region. Finally, a short summary is given in chapter 7.

1.1 Outline of observational and modeling studies in the tropical eastern Pacific

Attempting to understand atmospheric convection mechanisms in tropical oceanic regions has been and continues to be an area of frequent research. Recently, the western Pacific warm pool region was the subject of a field campaign, the Tropical Ocean Global Atmosphere Coupled Ocean Atmosphere Response Experiment (TOGA COARE), which has yielded no less than 129 publications (source: MGA, November 8, 1997). Currently, eastern Pacific forcing of the North American monsoon system is the subject of the Pan-American Climate Studies (PACS) program. The goal of many observational and modeling studies has been to better understand the controlling mechanisms of the Pacific intertropical convergence zone (ITCZ). Early observational studies of the eastern Pacific wind field documented the presence of a double ITCZ structure, defined by convergence zones north and south of the equator, during the boreal spring (Alpert, 1945). Major Leo Alpert, a United States Army Air Corps officer, compiled aircraft data recorded during World War II to make the first known observation of a double ITCZ in the eastern Pacific. The occurrence of the double ITCZ was revisited in the late 1960's when the first experimental meteorological satellites were launched by the Environmental Space Services Administration (ESSA). A double ITCZ in the eastern Pacific was observed in the cloud field recorded by ESSA III and V visible sensors (Kornfield *et al.*, 1967). Further satellite studies using the ESSA satellites (Hubert *et al.*, 1969; Winston, 1971; Gruber, 1972; Musk, 1976) confirmed that the double ITCZ structure was only present in the eastern Pacific for a limited time during the boreal spring. More recently, the frequency and intensity of the global ITCZ has been studied by Waliser and Gautier (1993). They used the Highly Reflective Cloud (HRC) data set (Garcia, 1985) which is based on visible observations from the Television and Infrared Observational Satellite (TIROS) series. Although this work focused almost exclusively on the global aspects of

the ITCZ, it does mention the existence of a double ITCZ in the eastern Pacific during the boreal spring. The vertical moisture and temperature structure of the eastern Pacific ITCZ was documented by Fernandez-Partagas and Estoque (1985) using radiosonde and drop sonde data recorded in June 1979. Although the double ITCZ is a temporally and spatially limited phenomenon of the global climate system, its evolutionary vertical structure has received little observational study. This is probably due to the paucity of data within the vast eastern Pacific region.

Numerical modeling studies which have attempted to describe the spatial structure of tropical convection and hence the position of the ITCZ began in earnest soon after the ESSA observations. Charney (1971) described how conditional instability of the second kind (CISK) is responsible for tropical cyclogenesis and the intertropical convergence zone. Pike (1971) used an axially symmetric coupled atmosphere-ocean model to investigate the latitudinal preference of the ITCZ based on meridional sea surface temperature (SST) profiles. Holton *et al.* (1971) showed that the position of the ITCZ is determined by easterly wave propagation. Lindzen (1974) used wave-CISK theory to assign a latitudinal preference to the ITCZ. More recently, Waliser and Somerville (1994) have shown, using an axially symmetric primitive equation model, that the ITCZ has a latitudinal preference regardless of where the meridional SST maximum is located. Philander *et al.* (1996) showed, using his model, that the ITCZ is mostly north of the equator because of continental effects. Accurately representing the ITCZ in a numerical model is far from complete. The presence of a double ITCZ year round is a common error produced by many coupled atmosphere-ocean general circulation models (GCMs). These models have a difficult time accurately representing the strength and position of the ITCZ (Mechoso *et al.*, 1995). This problem is so persistent that it is referred to as the coupled GCM *double ITCZ syndrome* (Ma *et al.*, 1996). This brief summary indicates that one, we are not sure how the ITCZ works, and two, we do not know how to

accurately represent the ITCZ in our numerical models. This leads us to two questions. First, what are the primary mechanisms responsible for convection in the tropical Pacific? If we can answer this question, we may be able to address a second: What are the assumptions made in numerical modeling which prevent us from accurately simulating the ITCZ? Using profiles of relative humidity and cloud water retrieved from satellite measured radiances along with other observational data, the mechanisms of convection in the tropical Pacific will be discussed and from those results, a hypothesis formed regarding the relative importance of those mechanisms to numerical modeling of the tropical atmosphere.

1.2 Assessment of tropospheric moisture retrievals

The role of water vapor and clouds in the global climate system is a research topic that has recently enjoyed increased attention. Various researchers in the climate community state a need to establish global observations of water vapor and clouds (Chahine, 1992; Coughlan and Avissar, 1996). Due to gaseous absorption, vertical profiles of tropospheric water vapor are necessary to quantify atmospheric radiative forcing. Furthermore, the relatively large amount of energy stored in atmospheric water vapor in the form of latent heat makes knowledge of its vertical and horizontal distribution important to the understanding of the global energy budget. Observations of tropospheric moisture are also necessary to initialize numerical weather prediction (NWP) models. Accurate initialization of the water vapor field in NWP models is important for the prediction of cloud formation and subsequent precipitation. Satellite data has been shown to improve NWP (Kashiwagi, 1987) and reanalysis data assimilation efforts (Mo *et al.*, 1995). Knowledge of global atmospheric moisture profiles and clouds is also necessary to validate general circulation and climate models. Satellite remote

sensing is currently the only method that can provide the dense, global coverage necessary for these applications.

Methods of retrieving water vapor profiles from infrared or microwave sounders have been developed and several are in operational use. Any retrieval method suffers from a variety of limitations due to the spectral interval at which the sensor is sounding or imaging the atmosphere. Since the infrared optical depth of clouds is usually large, infrared sensors can not retrieve moisture in cloudy areas and thus must operate on cloud cleared radiances. Clouds also affect microwave sensors. Since the microwave optical depth of clouds is usually not large, retrieval methods may use these sensors to retrieve moisture profiles in the presence of clouds as well as the cloud liquid and or ice water contents. However, sub-field-of-view size clouds may not be properly identified, causing errors in the radiative transfer calculation (Greenwald *et al.*, 1997). Retrieval methods can avoid this problem by using completely cloudy or completely clear microwave radiances. Since the microwave sensor field of view is large, many regions of the globe that are fractionally cloudy at that sensor's resolution are improperly retrieved or not retrieved at all.

The Advanced Microwave Sounding Unit (AMSU) will be the primary microwave observing instrument on future National Oceanic and Atmospheric Administration (NOAA) polar orbiting satellites. Although future efforts to retrieve water vapor profiles propose using a combined infrared and microwave system, little work evaluating such a system has been published. The need for a combined infrared-microwave satellite retrieval system has been recognized (Eyre, 1989, 1990). Apart from a few simulation studies using AMSU and High Resolution Infrared Sounder (HIRS) channels (Eyre, 1990; Muller *et al.*, 1994), the literature is void of any work showing real evidence that a combined microwave-infrared water vapor profile retrieval system is beneficial. Currently, the only microwave instrument capable of being used for retrieving soundings

of tropospheric moisture is the Special Sensor Microwave/Temperature-2 (SSM/T-2). The SSM/T-2 is a five channel total power microwave radiometer aboard the Defense Meteorological Satellite Program (DMSP) polar orbiting satellites. This sensor measures the upwelling radiation near the 183.31 GHz water vapor absorption line. Many researchers have shown that moisture profiles can be retrieved using radiances measured near the 183 GHz line. (Kakar, 1983; Wilheit, 1990; Lutz *et al.*, 1991; Kuo *et al.*, 1994; Wang *et al.*, 1995). Wang *et al.* (1995) evaluated the performance of the Microwave Imaging Radiometer (MIR), which is an airborne radiometer with a spectral response similar to that of the SSM/T-2, using radiosonde and Raman LIDAR measurements. Currently published work using SSM/T-2 observations is limited in that little attempt to evaluate retrieval performance against *in situ* (radiosonde) moisture profiles has been made. Furthermore, the effect of clouds on the retrieval process has yet to be assessed using observations.

1.3 Evaluation and application of the algorithm

The work presented here evaluates a combined infrared-microwave retrieval system. Geostationary Operational Environment Satellite-8 (GOES-8) imager infrared observations at 10.7 and 12.0 μm, and SSM/T-2 microwave observations at 91.655, 150.0, 183.31 +/-7, +/-3 , +/-1 GHz (hereafter referred to as 92, 150, 176, 180, 182 GHz), are used to retrieve a tropospheric relative humidity profile, cloud liquid and ice water, cloud top height and surface temperature. The hypothesis of using the infrared imager in addition to the microwave sounder is that the infrared imager could potentially add up to four useful pieces of information: boundary layer moisture content, surface temperature, cloud top temperature, and cloud fraction within the microwave sounder's field of view. This additional information should be vital to the accuracy of microwave radiative transfer calculations in the presence of clouds. Microwave sounder partial beam filling

by clouds can be accounted for, as well as, establishing the height of the cloud and thereby giving some indication of whether the cloud is absorbing (liquid cloud) or scattering (ice cloud) microwave radiation. Determining the usefulness of adding the infrared radiances to the retrieval mechanism is also important in terms of computational expense. Infrared radiative transfer calculations are typically more computationally expensive than the microwave calculations, thus minimizing the number of frequencies for which a radiance must be calculated by the forward model is important. This work describes the methods used in such a retrieval system and evaluates its performance using *in situ* data. Retrievals on simulated data are used to illustrate the extent to which adding the infrared radiances may improve the moisture profile retrieval in fractionally cloudy regions. An assessment of the effect of neglecting ice clouds on the microwave retrieval of moisture profiles is also made using simulated data. Moisture profiles retrieved over continental and oceanic surfaces under clear, fractionally cloudy, and cloudy sky conditions are compared to nearby radiosonde measurements. Chapter 2 gives a description of the retrieval algorithm, while chapter 3 evaluates the retrieval system using simulated data and compares retrieved profiles from satellite observations to radiosonde measurements.

The retrieval algorithm is then used to produce a data set to investigate the evolution of the intertropical convergence zone in the eastern Pacific during boreal spring. Chapter 4 describes vital characteristics of this data set and compares various retrieved parameters to other data sets derived from other remote sensors, model output, or radiosondes. An assessment of the intra-seasonal and inter-annual variability of this and other data sets used to observe the evolution of the eastern Pacific ITCZ is shown in chapter 5. Furthermore, these data are used to objectively define the presence or absence of the double ITCZ in the central and eastern Pacific. Chapter 6 summarizes the relative importance of some convection forcing mechanisms, like sea surface temperature and

mass convergence, in the central and eastern Pacific. Additionally, hypotheses are made about how each mechanism contributes to the evolutionary structure of the ITCZ during the warm season. Finally, chapter 7 gives a brief summary of the entire work.

2 Description of the Retrieval Algorithm

Since water vapor profiles can be highly structured, especially in the presence of clouds, and the number of independent observations is much less than the number of retrieved variables, the inversion process (retrieval) must be constrained in order to obtain a solution. Using Bayes theorem allows for the introduction of prior information about the atmospheric state which constrains the solution in a mathematically sound manner. The Bayesian Water vapor Retrieval (BWR) algorithm consists of three modules: the Inputs Module, the Radiative Transfer Module, and the Optimization Module. The Inputs Module defines all the information required by the algorithm. The Radiative Transfer Module simulates the observations based on the user specified atmospheric structure. The Optimization Module works to find the best solution to the atmospheric structure given the observations and prior information. Any number of observations can be used to retrieve any number of atmospheric state variables. Of course the accuracy, or reliability of the atmospheric state solution, depends on the quality and quantity of the observations. Since the Optimization Module is a function of the Inputs and Radiative Transfer Modules, it is described first.

2.1 Optimization module

Bayes theorem has been used to retrieve temperature and moisture (Eyre, 1989) or precipitation (Evans *et al.*, 1995a) from passive radiometric observations. Bayes theorem, as applied to moisture profile retrieval, states

$$P(x|y) = a\, P(y|x)\, P(x) \tag{1}$$

where P(x|y) is the posterior probability given the atmospheric state, x (moisture profile to be retrieved) and the observations, y (satellite brightness temperatures). P(y|x) is the conditional probability, P(x) is the prior probability, and *a* is a normalization constant. Assuming a multivariate normal distribution,

$$P(y|x) = \exp\left[- (y - y(x))^T C_y^{-1} (y - y(x)) / 2 \right] \tag{2}$$

$$P(x) = \exp\left[- (x - x_m)^T C_x^{-1} (x - x_m) / 2 \right] \tag{3}$$

where y(x) is the simulated observation (brightness temperature) based on a forward model calculation using the retrieved moisture profile, x; C_y is the combined error covariance of the observing system (satellite sensor) and the forward model; x_m is the prior (climatological mean) profile; and C_x is the prior covariance. In their application of Bayes theorem to the inversion problem, Eyre (1989) and Evans *et al.* (1995a) used model output to form the prior distribution. In this work, the prior distribution is described by observations from other observing systems: *in situ* sensors and remote sensors. The goal is to choose the atmospheric profile, x such that P(x|y) is a global maximum. This can be accomplished by finding the global minimum of

$$J(x) = (y - y(x))^T C_y^{-1} (y - y(x)) + (x - x_m)^T C_x^{-1} (x - x_m) \tag{4}$$

The Optimization Module is where the BWR algorithm attempts to minimize J(x), and thus finds the maximum posterior probability, P(x|y) for a given set of observations, y.

The value of the atmospheric state vector, x, which does this, produces a solution to this inversion problem. Although analysis of radiosonde profiles indicated that the prior may be represented by the beta distribution, it was not chosen for this work. Since the parent distributions for the conditional and prior are not known, the normal distribution was chosen because finding its maximum is the equivalent of minimizing a weighted distance function. The Powell Direction Set Method (e.g., Press *et al.*, 1992) was used to minimize (4). This method has the advantage of not having to calculate a multivariate gradient. Specification of the prior mean profile, x_m and the covariance matrices, C_y and C_x is critical to the success of the inversion process. The values of the C_y, C_x, and x_m used in the minimization process (equation 4) for ocean surfaces are explicitly given in Table 2.5 and for land surfaces in Table 2.6. The methods and data used to calculate these components will be discussed in later in this chapter. Regardless of the method chosen for minimization, the possibility of obtaining a solution which is a local minimum rather than the global minimum still exists. Results (not shown) indicate that a given profile may have several mathematically valid solutions depending on the initial guess. A number of different initial guesses were used, and it was found that although the initial guesses differed significantly, the solution returned by the algorithm varied little.

2.2 Inputs module

The Inputs Module within the BWR algorithm consists of three basic parts: the atmospheric structure, the prior information, and the observations. The user defined atmospheric structure is flexible, but for clarity, the structure used for the evaluation process will be described here. The structure specifies the variables to be retrieved and the auxiliary information which is assumed known. The variables retrieved and the auxiliary information for the evaluation process is presented in Table 2.1. The vertical coordinate for the relative humidity profile was specified by height above the surface in

kilometers. These levels roughly correspond to the upper air mandatory reporting levels at the surface, 850 mb, 700 mb, 500 mb, 400 mb, and 300 mb. Any number of levels may be chosen, however, given that the number of independent observations is fixed, the degree to which the variables retrieved at those levels are independent (contain more information about the atmospheric state than the prior information) decreases as the number chosen increases. The variables retrieved were: surface temperature, relative humidity at the first six levels, cloud liquid water content, liquid cloud top height, cloud ice water content, ice cloud top height, and microwave surface emissivity parameter-1 (MSEP1). The MSEP1 accounts for changes in the surface emissivity due to variations in the ocean surface winds or changes soil moisture (see section 2.3 for more detail). The height of the first level and the temperature at each level coordinate above the surface were given as auxiliary information, therefore, the temperature profile was not retrieved. A combined retrieval of temperature and moisture would be possible if Special Sensor Microwave/Temperature (SSM/T) data were used along with the SSM/T-2 radiances. Since the vertical and horizontal resolution of the SSM/T is poor (four channels are sensitive to tropospheric temperature at ~200 km horizontal resolution), nearby radiosonde temperature profiles were used to avoid any additional error incurred by attempting to retrieve the temperature profile. Additionally, the ice cloud fraction (liquid cloud fraction assumed to be the same) was given as auxiliary information for the combined microwave-infrared (MW+IR) retrieval, but was set to unity for the microwave-only (MW-only) method. Other auxiliary inputs necessary for the radiative transfer calculations, but not retrieved, were held constant, those were: ice and liquid cloud thickness, liquid cloud droplet effective radius, ice cloud particle median volume diameter, total column ozone concentration, and surface emissivity parameters for microwave and infrared radiative transfer (see for example Table 2.2). The BWR algorithm used this structure to set up the retrieval mechanism.

The prior information is that which is used to constrain the inversion problem. Typically, the climatological mean, and its covariance, x_m and C_x from (4), are used to constrain the solution (Eyre, 1989), and that is what was done in the present work. The methods and data used are described in section 2.4.

Any number of observations may be used by the BWR algorithm. Within the Inputs Module, a description of each observation must be given. This includes: the type of each observation (specified as: microwave, infrared-cloudy, or infrared-clear), the frequency and polarization (microwave only) of the observation, and the combined "instrument-forward model" noise associated with each observation. All observations are assumed to be brightness temperature in Kelvin. The observations used in this work are listed in Table 2.3. The microwave observations were those of the SSM/T-2 with its five unpolarized (polarization actually rotates with scan angle, however for radiative transfer purposes it was assumed to be unpolarized) channels at 91.6, 150.0, 176.3, 180.3, 182.3 GHz. The infrared observations were those of the GOES-8 imager channels 4 and 5 at 935 and 835 cm^{-1} (10.7 and 12.0 μm), respectively. Both the mean clear and mean cloudy infrared radiances, spatially contained within the larger SSM/T-2 pixel, were converted to brightness temperature. Over the ocean, each channel was assigned a noise level of 1.0 K. The noise level assignments were given by the sum of the instrument noise, approximately 0.5 K, and the forward model error which was assumed to be of equal or greater value. The surface viewing microwave channels, over land, had their noise increased to 10.0 K, effectively removing them from the optimization process (see for example, Table 2.3). Initially, the surface viewing channels had smaller noise assignments, but contributed negatively in the optimization process. It is believed that the algorithm was unable to accurately assign the microwave surface emissivity over land due to observation frequency and field of view (pixel size) differences. In all, there were

up to nine observations used: five from the SSM/T-2 and two to four from the GOES-8 imager (clear and/or cloudy for each of the two channels used).

2.3 Radiative transfer module

The Radiative Transfer Module consists of several different parts. The primary component is the integration procedure. The integration procedure calculates the simulated observations based on the given atmospheric state (retrieved variables) and auxiliary information. The integration procedure includes the processes of microwave absorption due to gases and liquid clouds, infrared absorption due to gases and liquid clouds, and infrared and microwave scattering and absorption by ice cloud particles. The integration procedure calculates simulated top of the atmosphere (TOA) brightness temperatures for all observational frequencies specified in the observation file. These simulated brightness temperatures are then passed to the Optimization Module along with the observed brightness temperatures and the calculation of the conditional probability is made. The various procedures within the Radiative Transfer Module are now discussed in greater detail.

The integration procedure constructs a fine resolution, one-dimensional layered model atmosphere within which all observations are to be simulated. The model atmosphere is initialized with the US standard atmospheric profile for temperature, relative humidity, and ozone. Profiles of temperature and relative humidity, which were derived from the auxiliary information and the initial guess profile, replace the US standard atmosphere values. Then the emittance from each layer of the model atmosphere and from the surface are calculated. Calculations are done separately for clear sky and cloudy sky for each observation (frequency). If the observation is at a microwave frequency, then the clear and cloudy sky radiances are summed with their weights given by the cloud fraction. The layer emittance is then integrated from the TOA

down to the surface, specularly reflected, and integrated upwards along the satellite viewing angle to the top of the model atmosphere producing a TOA radiance.

The microwave absorption for gases and clouds is based on an updated version of the Millimeter wave Propagation Model (Liebe, 1989). The infrared absorption by gases is calculated for all layers using the correlated-k distribution method (Kratz, 1995). Infrared absorption by clouds is done separately for layers that contain clouds using the geometric optics approximation for highly absorbing media ($\tau_{abs}=3/4*lwp/r_{eff}$). Eddington's Second Approximation (Deeter and Evans, 1997) is used to compute the radiative transfer of (scattering) ice clouds. This radiative transfer scheme assumes a one-dimensional, single-layer, homogeneously scattering ice cloud. The necessary optical properties: single scatter albedo, extinction, and asymmetry parameter are calculated off-line by Mie code for spherical particles and by Discrete Dipole Approximation methods for non-spherical ice particles (Evans *et al.*, 1995b). The surface emissivity for the microwave channels is specified separately for land and ocean. The ocean surface microwave emissivity is assumed to be the product of the Fresnel emissivity of calm water and MSEP1 (Table 2.1). Allowing for changes in the emissivity of the ocean surface, through the retrieval of MSEP1, accounts for any surface emissivity increases due to winds at the surface. The land emissivity is given by the formula (after Grody, 1988),

$$\text{emissivity} = [\text{MSEP1} + \text{MSEP2}\ (\text{FREQ}/\text{MSEP3})^{\text{MSEP4}}]/ [1 + (\text{FREQ}/\text{MSEP3})^{\text{MSEP4}}] \quad (5)$$

where MSEP2 - MSEP4 are specified in Table 2.2, and FREQ is the frequency of the observation in GHz.

2.4 Data preprocessing

The BWR Inputs Module requires various types of input data. Satellite brightness temperatures were used as the observational inputs. Auxiliary input data included cloud fraction within the SSM/T-2 pixel calculated from higher resolution GOES-8 infrared observations and temperature profiles from radiosonde measurements or model analysis. The prior mean and covariance for the surface temperature and the relative humidity at all retrieved levels was calculated using several years of historical nearby radiosonde profiles for each month in the evaluation period (August and September). The cloud liquid water mean and variance were derived from Special Sensor Microwave/Imager (SSM/I) liquid water path measurements given by the NASA water vapor data set (Randel *et al.*, 1996). Ice cloud water content mean and variance were derived from First International Satellite Cloud Climatology Project (ISCCP) Regional Experiment (FIRE-II) data and Complex Layer cloud Experiment (CLEX) data. The mean cloud tops (ice and liquid), as well as the microwave surface emissivity factor (MSEP1) were chosen arbitrarily and given large variances. The values of the Combined Error Covariance (C_y), Prior Covariance (C_x), and Prior Mean (x_m) used in the minimization process (equation 4) for ocean surfaces are explicitly given in Table 2.5 and for land surfaces in Table 2.6.

Collocation of the infrared and microwave satellite radiances is important to the outcome of the retrieval process. The SSM/T-2 data was the spatial and temporal basis set for all other input data. The Polar Orbiter Remapping and Transformation Application Library (PORTAL) software package (Jones *et al.*, 1995) was used to spatially remap the GOES-8 infrared radiances to the SSM/T-2 image space. It should be noted that the SSM/T-2 pixel size changes with frequency and zenith angle. At nadir, the field of view diameter (pixel size) of the 182, 180, and 176 GHz channels is ~48 km, however, the pixel size for the 150 GHz channel is ~54 km and the 92 GHz pixel size is ~84 km (Falcone *et al.*, 1992). These pixel sizes increase as the instrument scans away

from nadir. The PORTAL algorithm used the higher resolution latitude and longitude coordinates (~48 km) to do the remapping of the GOES imager data.

Prior to the remapping, the collocated full-resolution GOES-8 images were flagged pixel-by-pixel as cloud/no-cloud using an infrared radiance threshold method on GOES-8 channel 4 imagery. A background image was generated using thirty images. The GOES-8 imager records an image of the Northern Hemisphere every 30 minutes; therefore the infrared data was temporally collocated within 15 minutes of the SSM/T-2 measurements used in this study. The time of the GOES image that was temporally closest to the SSM/T-2 measurement was designated as the *measurement time*. Images recorded at the same time of day as the *measurement time*, as well as the images recorded just before and just after the *measurement time*, for ten consecutive days, were used to form the background image. The background image was created by taking the warmest pixel of the 30 images at each pixel location. By comparison with coincident visible imagery, it was determined that 10 days of infrared imagery was sufficient to obtain clear pixels in the regions used for the evaluation process. This, of course, may not be true in other locations (i.e., off the coast of California in June). The *measurement time* image was then compared to the background image; pixels with brightness temperatures 7 K below the background image were flagged as cloudy. By comparison to visible imagery, it was determined that a 7 K threshold was sufficient to identify clouds in the regions used for evaluation of the BWR algorithm.

The PORTAL software was then used to calculate mean clear and mean cloudy radiances, as well as cloud fraction, within the lower resolution SSM/T-2 pixel. Since the nominal pixel size of GOES-8 imager channel 4 is 4 km and the nominal size of the SSM/T-2 pixel is 48 km, there are 144 GOES-8 pixels within one SSM/T-2 pixel. Assuming that the threshold cloud identification was working properly, the data-preprocessing module calculated the cloud fraction to one part in 144 or 0.7%. The lower

frequency SSM/T-2 observations will have additional error in the cloud fraction introduced since those channels have over sampled the atmosphere and surface. The satellite data preprocessed for use in the retrieval algorithm is shown in Table 2.4.

The remainder of the auxiliary data, the temperature profile collocated to the SSM/T-2 observation, came from model analysis or radiosonde measurements. Radiosonde measurements were used for the evaluation process (section 3.2), whereas, model analysis was used for the retrieval on simulated data (section 3.1) and for the study of the tropical eastern Pacific (chapter 4 and following). The model analysis temperature fields were linearly interpolated horizontally to SSM/T-2 observation point and vertically to the level coordinates specified in Table 2.1.

The radiosonde temperature profiles were linearly interpolated vertically to the level coordinates. No horizontal interpolation was done as only the nearest neighbor pixels were used in the evaluation process.

Table 2.1. List of retrieved Variables and Auxiliary Data. The mean and standard deviation of the prior profile used in the evaluation process (chapter 3.2) is also shown.

Height (km)	Variable	Mean ocean/land	Std Deviation ocean/land		Auxiliary
-	Liquid Cloud Water (g m^{-3})	0.2 / 0.2	0.4 / 0.4		-
-	Liquid Cloud Height (km)	2.5 / 2.5	4.0 / 4.0		-
-					Cloud Fraction
-	Ice Cloud Water (g m^{-3})	0.05 / 0.05	0.4 / 0.4		-
-	Ice Cloud Height (km)	8.0 / 8.0	4.0 / 4.0		-
-	Microwave Emis. Param. 1	1.0 / 0.98	0.2 / 0.2		-
0.0	Surface Temperature (K)	299 / 301	2 / 6		-
0.0	Relative Humidity (%)	86 / 59	9 / 21		Height (km)
1.5	Relative Humidity (%)	72 / 62	16 / 14		Temperature (K)
3.0	Relative Humidity (%)	54 / 58	19 / 21		Temperature (K)
5.5	Relative Humidity (%)	41 / 40	23 / 23		Temperature (K)
7.5	Relative Humidity (%)	35 / 30	22 / 21		Temperature (K)
9.5	Relative Humidity (%)	31 / 30	17 / 17		Temperature (K)
12.0	-				Temperature (K)

Table 2.2. List of auxiliary inputs assumed to be constant.

Constant Auxiliary Inputs	Land surface value	Ocean surface value
Liquid Cloud Thickness (km)	1.0	1.0
Ice Cloud Thickness (km)	1.0	1.0
Liquid Cloud Droplet Radius (μm)	20	20
Ice Cloud Particle Median Diameter (μm)	200	200
Total Column Ozone (Dobson units)	350	350
Infrared Surface Emissivity	0.96	0.98
Microwave Surface Emissivity Parameters (2, 3, 4)	0.98, 91.6, 0	0, 91.6, 0

Table 2.3. Observation frequencies {wave numbers} used with assigned noise values.

Observation Type	**Frequency (GHz) / { Wave number (cm^{-1}) }**	**Noise (K) over land**	**Noise (K) over ocean**
Microwave	91.65	10.0	1.0
Microwave	150.0	10.0	1.0
Microwave	176.3	1.0	1.0
Microwave	180.3	1.0	1.0
Microwave	182.3	1.0	1.0
Infrared Clear	{935}	1.0	1.0
Infrared Cloud	{935}	1.0	1.0
Infrared Clear	{835}	1.0	1.0
Infrared Cloud	{835}	1.0	1.0

Table 2.4. List of data written to file by the satellite preprocessing algorithm.

Land mask designator
Latitude
Longitude
SSM/T-2 zenith angle
SSM/T-2 brightness temperatures (5)
GOES-8 zenith angle
Clear GOES-8 brightness temperatures(2)
CloudyGOES-8 brightness temperatures(2)
Cloud fraction within each SSM/T-2 pixel

Table 2.5. Combined Error Covariance (C_y), Prior Covariance (C_x), and Prior Mean (x_m) used in the minimization process (equation 4) for ocean surfaces.

Combined Error Covariance (C_y) Matrix:

Frequency (GHz) {Wavenumber (cm^{-1})}									
Microwave 91.65	1.0	0	0	0	0	0	0	0	0
150.0	0	1.0	0	0	0	0	0	0	0
176.3	0	0	1.0	0	0	0	0	0	0
180.3	0	0	0	1.0	0	0	0	0	0
182.3	0	0	0	0	1.0	0	0	0	0
Infrared {935} - clear	0	0	0	0	0	1.0	0	0	0
{935} - cloud	0	0	0	0	0	0	1.0	0	0
{835} - clear	0	0	0	0	0	0	0	1.0	0
{835} - cloud	0	0	0	0	0	0	0	0	1.0

Prior Mean (x_m) Vector [left] and Prior Covariance (C_x) Matrix [right]

x_m	variable	C_x											
0.2	Liquid Water Content (g m^{-3})	0.16	0	0	0	0	0	0	0	0	0	0	0
2.5	Liquid Cloud Top Height (km)	0	16.0	0	0	0	0	0	0	0	0	0	0
0.05	Ice water Content (g m^{-3})	0	0	0.16	0	0	0	0	0	0	0	0	0
8.0	Ice Cloud Top Height (km)	0	0	0	16.0	0	0	0	0	0	0	0	0
1.0	MSEP-1	0	0	0	0	0.04	0	0	0	0	0	0	0
299	Surface Temperature (K)	0	0	0	0	0	3.02	-10.3	-0.37	-3.78	-3.78	-2.04	-0.45
85.6	Relative Humidity (%) at 0.0 km	0	0	0	0	0	-10.3	78.1	15.5	25.0	25.0	11.9	1.94
72.2	Relative Humidity (%) at 1.5 km	0	0	0	0	0	-0.37	15.5	245	128	71.0	48.1	36.5
54.0	Relative Humidity (%) at 3.0 km	0	0	0	0	0	-3.78	25.0	128	352	208	116	63.4
41.0	Relative Humidity (%) at 5.5 km	0	0	0	0	0	-3.78	25.0	71.0	208	518	291	135
35.3	Relative Humidity (%) at 7.5 km	0	0	0	0	0	-2.04	11.9	48.1	116	291	497	218
31.3	Relative Humidity (%) at 9.5 km	0	0	0	0	0	-0.45	1.94	36.5	63.4	135	218	305

Table 2.6. Combined Error Covariance (C_y), Prior Covariance (C_x), and Prior Mean (x_m) used in the minimization process (equation 4) for land surfaces.

Combined Error Covariance (C_y) Matrix:

Frequency (GHz) {Wavenumber (cm^{-1})}									
Microwave 91.65	100.0	0	0	0	0	0	0	0	0
150.0	0	100.0	0	0	0	0	0	0	0
176.3	0	0	1.0	0	0	0	0	0	0
180.3	0	0	0	1.0	0	0	0	0	0
182.3	0	0	0	0	1.0	0	0	0	0
Infrared {935} - clear	0	0	0	0	0	1.0	0	0	0
{935} - cloud	0	0	0	0	0	0	1.0	0	0
{835} - clear	0	0	0	0	0	0	0	1.0	0
{835} - cloud	0	0	0	0	0	0	0	0	1.0

Prior Mean (x_m) Vector [left] and Prior Covariance (C_x) Matrix [right]

x_m	variable	C_x											
0.2	Liquid Water Content (g m^{-3})	0.16	0	0	0	0	0	0	0	0	0	0	0
2.5	Liquid Cloud Top Height (km)	0	16.0	0	0	0	0	0	0	0	0	0	0
0.05	Ice water Content (g m^{-3})	0	0	0.16	0	0	0	0	0	0	0	0	0
8.0	Ice Cloud Top Height (km)	0	0	0	16.0	0	0	0	0	0	0	0	0
0.98	MSEP-1	0	0	0	0	0.04	0	0	0	0	0	0	0
301	Surface Temperature (K)	0	0	0	0	0	35.0	-111	-18.7	-16.4	-17.1	-14.0	-15.9
59.1	Relative Humidity (%) at 0.0 km	0	0	0	0	0	-111	455	116	87.3	95.0	47.4	49.3
61.5	Relative Humidity (%) at 1.5 km	0	0	0	0	0	-18.7	116	208	77.7	68.3	44.7	18.6
57.7	Relative Humidity (%) at 3.0 km	0	0	0	0	0	-16.4	87.3	77.7	426	225	109	64.1
39.7	Relative Humidity (%) at 5.5 km	0	0	0	0	0	-17.1	95.0	68.3	225	549	263	111
30.3	Relative Humidity (%) at 7.5 km	0	0	0	0	0	-14.0	47.4	44.7	109	263	427	199
29.8	Relative Humidity (%) at 9.5 km	0	0	0	0	0	-15.9	49.3	18.6	64.1	111	199	302

3 Evaluation of the Retrieval Algorithm

The retrieval algorithm described in chapter 2 is now evaluated. This process includes an assessment of the effects of ice cloud scattering on moisture profile retrieval using simulated microwave radiances. Ice clouds with large particle sizes and water paths are found to significantly degrade retrieval performance if not accounted for in the radiative transfer calculation. Retrievals on simulated clear sky radiances with appropriate noise added are found to have approximately 12% RMS error. The error is larger in the presence of simulated clouds, but is found to be significantly reduced when using the combined microwave-infrared retrieval. Moisture profiles retrieved from F12 SSM/T-2 radiances are compared to nearby radiosonde measured profiles. The combined microwave-infrared retrieval is shown to beneficial in cloudy skies over land surfaces. Finally, the natural variability of the moisture profile is shown to frequently be large, making retrieval validation efforts difficult.

3.1 Characteristics of the retrieval system using simulated data

3.1.1 Sensitivity to the moisture profile

Fundamental understanding of the retrieval system can be achieved using the methods described by Rodgers (1990). It is important to know how much the radiance, measured by the satellite sensor, changes for a given change in the atmospheric state. To investigate this sensitivity, a mean atmospheric state was assumed and simulated brightness temperatures were calculated with no noise added. Then the state variables

were perturbed independently at each level specified in the structure file, brightness temperatures calculated, and then differenced from the mean state brightness temperatures. Since surface emissivity is important for surface viewing microwave channels, this procedure was done for both surface types: land and ocean. The sensitivity tests presented here were for clear sky conditions only.

Figure 3.1 shows the two different mean moisture profiles that were used to characterize the sensitivity of the instruments. Figure 3.2 and Figure 3.3 show the modeled sensitivity of both instruments used, to a 10% change in relative humidity at the given level. Figure 3.2a, Figure 3.2b, and Figure 3.3a illustrate the modeled sensitivity of the sensor for dry upper tropospheric conditions, whereas Figure 3.2c, Figure 3.2d, and Figure 3.3b show the modeled sensitivity for a moist upper troposphere. Comparison of Figure 3.2a and Figure 3.2c, Figure 3.2b and Figure 3.2d, and Figure 3.3a and Figure 3.3b indicates that the modeled sensitivity of a given sensor to changes in the relative humidity profile at a given level depends on the mean state profile. Comparison of the modeled sensitivity between upper atmospheric moisture types indicates that the SSM/T-2 is less sensitive to moisture changes at all levels when larger values of upper level moisture are present. Figure 3.3 shows that the modeled sensitivity of the GOES-8 imager channels 4 and 5 is affected little by the upper level moisture. For microwave sensors, surface emissivity is even more important. For high surface emissivity (dry land emissivity = 0.98), the SSM/T-2 is insensitive to 10% changes in the relative humidity moisture profile below 3 km for a dry upper troposphere (Figure 3.2a) and below 5 km for a moist upper troposphere (Figure 3.2c). The instrument noise for the SSM/T-2 is nominally 0.5 K for each channel, thus over land, the SSM/T-2 can not measure a 10% relative humidity change at any level below 10 km in a moist upper troposphere. The nominal instrument noise for the GOES-8 channels 4 and 5 is 0.2 K. Therefore, channel 5 is sensitive to a 10% relative humidity change, whereas, channel 4 is not. The profiles in

Figure 3.2 and Figure 3.3 represent the expected response of the instrument to the moisture profile. In this way, they are similar to the classic transmission weighting functions. However, Figure 3.2 and Figure 3.3 provide some important information that classical transmission weighting functions do not. Due to the high surface emissivity of the land surface, Figure 3.2a and Figure 3.2c illustrate that the SSM/T-2 is not very sensitive to lower level moisture over land. From this result, even if the surface emissivity could be specified with no error, it is expected that retrieved low level humidity values over land will largely depend on the prior information. This result could not be inferred from the classical transmission weighting functions.

3.1.2 Expected performance of a combined retrieval system

Profile retrieval using simulated data is a satisfactory way to assess the ability of the retrieval algorithm's numerical optimization scheme as well as gain some understanding of how the atmospheric profile affects the retrieval mechanism. Simulated observations were produced using 200 temperature and moisture profiles from the National Centers for Environmental Prediction (NCEP)/ National Center for Atmospheric Research (NCAR) Reanalysis data set in the forward model. Random noise (-1.0 to 1.0 K) was added to the simulated brightness temperatures. The optimal characteristics of the retrieval system were tested in both clear and cloudy sky conditions over ocean using the MW+IR and the MW-only methods. Then the BWR algorithm was used to retrieve the moisture profiles from this synthetic data set. No simulated noise was given to the temperature profiles or the cloud fraction. This procedure was done for clear sky, fractionally cloudy sky, and completely cloudy sky conditions. The relative humidity at the simulated cloud level was adjusted to 95%. To assess the performance of the BWR system on these synthetic data, the root mean square (RMS) of the known profile-retrieved profile difference, as well as, the bias, defined as the difference of the mean

known and mean retrieved profiles were calculated. Figure 3.4 and Figure 3.5 show the RMS and bias for relative humidity (RH) profile retrievals using synthetic data with liquid cloud fraction and ice cloud fraction set equal to 0.5 and 0.0, and 0.0 and 0.5, respectively. The MW+IR retrieval method out performs the MW-only retrieval method in terms of both RH profile RMS and bias in the presence of fractionally covered liquid or ice cloud skies. The surface type for the results presented here was ocean (lower microwave emissivity), however similar results were obtained over land (higher microwave emissivity). The greatest improvement, in terms of a reduced RH profile RMS and bias, occurred in the liquid cloud case. This was to be expected as the microwave channels are more sensitive to the simulated liquid clouds than to the simulated ice clouds. The cloud water and cloud top height RMS and bias for both cloud types and methods is shown in Table 3.1. The MW+IR and MW-only methods perform equally poorly in the liquid cloud case (large RMS), but the MW+IR method performs much better than the MW-only method in the ice cloud case. For the cases of clear sky and completely overcast sky (not shown), little improvement was recognized when using the MW+IR method. Therefore, it would be expected that the MW+IR method should outperform the MW-only method in fractional cloud cover over any surface in terms of RH profile retrieval performance.

3.1.3 Sensitivity to ice clouds

Synthetic data, simulated radiances calculated by the forward model using a known moisture/cloud profile, is useful in determining how well we can expect the retrieval system to perform. Figure 3.6 shows the RMS and bias for the retrieval of clear sky moisture profiles over the tropical Atlantic where the simulated radiances were calculated using 200 NCEP/NCAR Reanalysis data moisture and temperature profiles. The mean relative humidity profile is a moist over dry over moist scenario typical in the tropics (see

Figure 3.1) and, due to reduced sensitivity (section 3.1.1), more difficult to retrieve than the typical dry over moist environment in the subtropics and mid-latitudes. This result shows the RMS and bias to be less than 15% at all levels regardless of whether or not the cloud radiative transfer was enabled. Although there were no clouds simulated for this case, the combination of high moisture present at the upper levels and simulated sensor noise caused the BWR algorithm to retrieve ice cloud water content in some pixels. Hence, the RH profile RMS and bias for this clear sky case where the cloud radiative transfer was enabled is slightly higher than when it was disabled. Figure 3.6 shows that the RMS of the known profile - climatological mean profile difference (hereafter denoted as *ClimMean*) was small at lower levels and large at upper levels. Comparing the ClimMean RMS (dashed line) with the retrieved profile RMS (solid line) shows how much improvement in the knowledge of the moisture profiles the retrieval system provides over a climatological mean profile assumption. In this case, at upper levels the improvement is a factor of four, whereas at lower levels, there is no improvement in terms of RH profile RMS. Due to instrument and forward model noise, the retrieval system's minimum RH profile RMS was found to be approximately 10% in relative humidity units at all levels when the ClimMean RMS is greater than 10%, and is equal to the ClimMean RMS when the ClimMean RMS is less than 10%. In addition, the bias for these clear sky retrievals on synthetic data range from –15% to +10% in relative humidity units, where positive values indicate that the retrieved moisture profile is more moist than the known profile. The RH profile RMS plot in Figure 3.6 indicates that the prior information, mean and covariance, is driving the solution in the lower levels, whereas the observations (simulated radiances in this case) are driving the solution in the upper levels. This is coincident with the fact that the known profiles are moister in the upper levels than the climatological mean and about equal to that mean in the lower levels as seen in the bias plot of Figure 3.6 (dashed line).

The synthetic data also allow for a simulated study of how we would expect the retrieved moisture profile to be affected by an ice cloud. Currently, there exists little observational evidence regarding the effects of ice clouds on SSM/T-2 measured radiances. Perhaps as a result, some moisture profile retrieval algorithms using the SSM/T-2 sounder neglect the effects of ice clouds. Figure 3.7 shows the RMS and bias for the 0 km to 10 km layer average as a function of ice particle median volume diameter and ice water content when no attempt to retrieve ice cloud properties is made. Calculations for spherical and 5-column rosette ice particles are shown. This figure illustrates that a water vapor retrieval system using the SSM/T-2 sounder incurs increasingly more error as the particle size and or ice water path increases. Since ice clouds typically have median volume diameters up to and exceeding 200 μm, neglecting this component could potentially introduce large errors in retrieved water vapor profiles at all levels. Therefore, based on these simulations, clouds with smaller particle sizes and moderate ice water paths would be expected to introduce little error. For example, cirrus clouds with a median volume diameter of 100 μm and an ice water path of 0.10 kg m^{-2} would introduce less than 10% RMS error. However, ice clouds like thunderstorm cirrus anvils with large ice water paths (e.g. 0.3 kg m^{-2}) and large particle sizes (e.g. 300 μm) would be expected to introduce large error (e.g. 30% RMS) if not accounted for in the radiative transfer calculation.

3.2 Comparisons of retrieved and radiosonde measured moisture profiles

The retrieval of the atmospheric state using observed satellite radiances and its subsequent validation is the best assessment of how well we can remotely sense the moisture in atmosphere. Simulated radiances do not provide for this assessment. Moisture profiles over land and ocean were retrieved and compared to radiosonde data. The temporal collocation between available radiosonde profile data and the polar orbiting

SSM/T-2 within the GOES-8 view of the earth is quite poor for validation studies. As for the global synoptic network, where sondes are launched nominally at 0000 UTC and 1200 UTC, the SSM/T-2 sensor on the DMSP F12 is at approximately 40 degrees west longitude where no radiosonde sites are present. The F11 SSM/T-2 sensor, which is in a 'better' orbit for comparisons to radiosonde data, was not used because the 150 GHz channel was inoperable. Thus for any validation using the global synoptic network, we must rely on the F12 overpass of the Caribbean region nominally at 0200 UTC and 1400 UTC. Therefore the temporal collocation bias is on the order of +2.0 hours. Nine radiosonde sites on western North Atlantic islands were used to evaluate the BWR algorithm's performance over the ocean. Table 3.2 lists the ocean sites used for this study. Validation over land was done using radiosonde data from the Atmospheric Radiation Measurement (ARM) program. The F12 satellite ascending overpass of the ARM site is nominally at 0330 UTC. The ARM site launches radiosondes at 2330 UTC and 0530 UTC. Therefore the temporal collocation bias is -4.0 hours and +2.0 hours. A limited number of launches were made at 0230 UTC, giving the best temporal coincidence of -1.0 hour. The F12 descending overpass of the ARM site is at 1530 UTC. The ARM site launches radiosondes at 1430 UTC and 1730 UTC giving a collocation bias of -1.0 hours and +2.0 hours. Comparison difficulties increase when the point measurement made by the radiosonde is not reflective of the volume measurement made by the satellite. The radiosonde data allow for validation of the relative humidity profile, however due to lack of cloud water measurements by *in situ* and other remote sensors, no effort was made to validate the retrieved cloud properties. Since the major point of this work was to quantify the extent to which a combined microwave-infrared retrieval system improves our ability to retrieve atmospheric moisture profiles over a microwave only retrieval system, it was necessary to compare retrieved RH profiles to *in situ* (radiosonde)

moisture profile data regardless of the errors incurred due to spatial or temporal variability in the actual moisture profile.

Since the MW-only method can not make use of the infrared sensor to calculate cloud fraction, this method assigned a constant cloud fraction of unity. Table 2.1, Table 2.2, and Table 2.3 show the variables, constants, and observations used for the MW+IR and MW-only methods. The time period for validation was August and September of 1996. During this period a total of 256 coincident profiles among the nine island sites were retrieved and 52 coincident profiles near the ARM site were retrieved. The RH RMS and bias were calculated using the two retrieved moisture profiles nearest the radiosonde moisture profile for both methods, MW+IR and MW-only.

3.2.1 Comparisons with the ARM radiosonde

Comparisons of the performance of the BWR algorithm operating in the MW+IR or MW-only modes over a land surface, near the ARM site in central Oklahoma, for various cloud conditions are shown in Figure 3.8 through Figure 3.11. These figures indicate that the MW+IR mode slightly outperforms the MW-only mode for all sky conditions (Figure 3.8) in terms of RH profile RMS and bias at most levels. Both methods perform better than climatology (dashed line), and the MW+IR method performs better than the CAL-VAL statistical retrieval method. Again, climatology is meant to refer to the RMS difference between the radiosonde moisture sounding and the monthly radiosonde climatological mean moisture sounding (ClimMean). The CAL-VAL RMS and bias results, a product of the DOD's effort to evaluate the performance of the DMSP SSM/T-2 sensor on the F11 satellite (Falcone *et al.*, 1992), are given as a reference point for evaluation. The CAL-VAL retrieved moisture profile-coincident radiosonde profile difference RMS and bias were reported for both land and ocean surfaces. The CAL-VAL results were produced using a statistical retrieval method which is conceptually very

different than the present method. It is important to note that the CAL-VAL results come from a different sensor with a different equatorial crossing time than that used in this work.

The MW-only mode does better in the lower levels than the MW+IR mode for clear sky conditions (Figure 3.9), however neither is any better than climatology except at the upper most level. Note that the MW+IR method does significantly worse at the surface (RH RMS = 23%, RH bias = -22%). The RMS and bias of the retrieved surface temperature were 7.5 K and +6.4 K, respectively. Large surface temperature changes in time and the temporal collocation error are believed to be responsible for these poor results. Poor surface temperature retrieval translates to poor relative humidity retrievals at and near the surface. The optimization scheme tries to balance the spuriously high surface temperatures retrieved by assigning low moisture values at or near the surface in order to satisfy the radiative transfer equation. The MW+IR method outperforms the MW-only method for completely cloudy sky cases (Figure 3.10). The MW+IR method also outperforms the ClimMean RMS by 5 to 10% at all levels. Additionally, the RH bias is less than 10% at all levels. The RMS and bias for retrieved surface temperature are 3.6 K and +0.7 K, respectively, indicating that little surface temperature error was present because, due to the presence of completely cloud covered skies, the IR channels were unable to view the ground. The RMS and bias results for fractionally cloudy skies, shown in Figure 3.11, indicate that the MW+IR is only slightly better in the lower and mid-levels. The overall result, for retrieved moisture profiles near the ARM site, is that the MW+IR method slightly outperforms the MW-only method. The strength of the MW+IR method is improvement in the retrieved moisture profile in cloud covered skies. This statement is tempered by the fact that the sample size is small (N~100), and therefore, the sampling error (10%) is in many cases larger than the difference between

the MW+IR and the MW-only results. It should be noted that this result was not expected from the simulation study (section 3.1.2).

3.2.2 Comparisons with the Barbados radiosonde

Although retrievals were completed for nine North Atlantic Ocean island sites, only one is presented here, Barbados. The RMS and bias results at Barbados are similar to the other 8 Caribbean sites. Out of the nine sites, Barbados had the greatest number of coincident profiles, 41. Furthermore, since the application (chapter 5) is carried out in a tropical environment and Barbados is the most tropical of the locations, it was used here. Overall, the MW+IR mode does no better than, and sometimes worse than, the MW-only mode in terms of RH profile RMS and bias statistics (Figure 3.12). Figure 3.13 indicates that under clear sky conditions, the MW-only retrieval method slightly out performs the MW+IR method. Contrary to the results at the ARM site, the MW-only method does significantly better in cloudy skies than the MW+IR method near Barbados. Figure 3.14 illustrates the retrieval performance for completely cloud covered skies and Figure 3.15 for fractionally cloudy skies. The MW+IR method fails at upper levels, doing worse than climatology. The MW-only method tends to have a small bias and usually meets or exceeds the ClimMean and CAL-VAL standards. Since the MW-only RMS of the Barbados comparison for all sky conditions is less than 20% at all levels and the bias is less than 5%, this method should be adequate for applications in the tropics. On the other hand, the performance of the MW+IR method is unacceptable. A possible explanation is that the MW+IR method is identifying thin high clouds as thick midlevel clouds based on the GOES-8 observed infrared brightness temperatures. The spurious identification of thin high clouds as thicker mid-level clouds critically affects the radiative transfer calculations. The large positive bias in cloudy retrievals near Barbados is evidence of this problem. Of the set of cloudy pixel retrievals, there were several profiles for which

the MW+IR retrieval did particularly poorly. Many of these were seen to have optically thin clouds present in the visible GOES imagery, however no objective method to screen out these profiles was accomplished. At this point, the MW+IR method described herein is not a viable option in regions where infrared optically thin clouds are frequently present. Use of an infrared sounder instrument, like that on the GOES-8 satellite, could possibly reduce the cloud height error. The advantage of the MW-only retrieval is that it is computationally much less expensive and is less sensitive to error introduced by high and mid level thin clouds.

3.2.3 Variability of water vapor profiles at the ARM site

When attempting to use radiosonde measurements to validate a retrieval method, it is important to consider the spatial and temporal variability of the actual water vapor/cloud water profile. With the data available, it is not possible to quantify the error incurred in these comparisons due to spatial variability. Some error is expected as the radiosonde measures a point value and the satellite retrieval measures a volume element. Estimating the temporal variability of the water vapor profile at the ARM site is possible, and was accomplished by calculating the RMS of the difference between two consecutive RH profile measurements. Since the F12 satellite passes over the ARM site at ~0330 and ~1530 UTC, the ARM radiosonde measurements taken at 0230 and 0530 UTC, as well as those taken at 1430 and 1730 UTC were used to calculate this RMS. These RMS profiles are shown in Figure 3.16. The 0230 – 0530 UTC RMS varies from 6% to 22%, whereas the 1430 – 1730 UTC RMS varies from 14% to 24% in relative humidity units. This analysis indicates that the temporal variability of the water vapor profile, as measured by the ARM sonde, over central Oklahoma is quite significant. In fact, this large variability indicates the RMS and bias calculations in sections 3.2.1 and 3.2.2 may not be very meaningful in judging the overall performance of the BWR algorithm. Similar analysis

on the radiosonde reported temperature profile showed low variability at mid and upper levels (RMS ~1 K), but large variability at the surface with the surface temperature RMS equal to 2.4 K and 5.1 K for the 0230-0530 UTC and 1430-1730 UTC time periods, respectively. This large variability could significantly degrade retrieval performance as the radiosonde reported temperature profile was used in the radiative transfer calculation as auxiliary data. In order to assess the effect of this temporal variability on the validation effort, a 'reduced set' of comparisons was made. The RMS and bias between the retrieved and radiosonde profiles was calculated for only those relative humidity profiles where consecutive ARM radiosonde measurements differed by less than 20% (in absolute relative humidity units) at all levels. These results are shown in Figure 3.17 for the MW+IR method, and in Figure 3.18 for the MW-only method. It is clear that the reduced set comparisons are much more favorable, producing lower RMS and bias statistics. Comparison of Figure 3.17 and Figure 3.18 shows that for this limited set (N=13) that the MW+IR and MW-only methods are doing equally well. The reduced set comparisons were not all clear sky comparisons as might be believed. Of the 13 profiles (26 retrievals used to calculate the RMS and bias), 20% were clear sky, 30% were completely cloud covered and 50% were fractionally cloud covered. Since the Barbados radiosonde (as well as the other North Atlantic island sites) is only launched twice per day, a similar comparison over an ocean surface was not possible. It is believed that the moisture profile over Barbados would exhibit similar behavior, although the surface effects should be considerably smaller.

3.3 Summary of the evaluation process

Microwave sounder and infrared imager data from different satellite platforms have been used together to retrieve water vapor profiles and cloud properties over land and ocean. The application of Bayes theorem has allowed for the inclusion of climatological

prior information derived from different observation systems to constrain the inversion problem in a mathematically sound manner. The quantitative advantage of the using both GOES-8 imager and SSM/T-2 microwave sounder radiances together to retrieve moisture profiles was investigated. It was found that the SSM/T-2 was less sensitive to the entire tropospheric moisture profile when high upper tropospheric humidity values were present. More importantly, it was shown that the SSM/T-2 is insensitive to boundary layer water vapor over a high emissivity surface like dry land. In tests using simulated data, ice clouds with large ice water paths and large particle sizes were found to degrade retrieval performance significantly if not accounted for in the radiative transfer calculation. Comparisons of retrieved and radiosonde measured RH profiles at the ARM site showed that the combined microwave-infrared retrieval system out performed the microwave-only retrieval system during cloudy sky conditions. An analysis of relative humidity profiles measured by radiosondes at the ARM site showed large temporal variability at all levels. Comparisons of retrieved profiles with a limited set of radiosonde profiles, in which the temporal variability was known *a priori* to be low, showed that both retrieval methods compared much more favorably to the radiosonde profiles, reducing the RMS at all levels by up to a factor of two. Retrievals on simulated data with appropriate noise added indicate that the retrieval algorithm error is on the order of 10 to 15% in RMS relative humidity units under clear sky conditions. The MW+IR method has the ability to maintain that performance under fractionally cloudy skies. The estimated error under completely cloudy skies for both methods is approximately 20 to 30% in relative humidity units. Comparisons with the reduced set of radiosondes, under all sky conditions, show that both the MW+IR and MW-only methods have RMS errors ranging from 8 to 20 % depending on the vertical coordinate. For discussion purposes, the error will be assigned a nominal value of 20% at all levels with the understanding that it may in fact be less in many cases. The microwave only method was shown to perform

better than the combined system when clouds were present near the Barbados radiosonde site in the western tropical Atlantic. It is believed that the combined retrieval system is unable to accurately assign cloud top height for infrared optically thin clouds, thus introducing large error into the retrieved profile. Due to the large computational expense of data remapping and infrared radiative transfer in the inversion process, a microwave only retrieval process could be computationally advantageous. Although a modest increase in performance, as measured by comparisons with radiosonde data, was achieved using the combined infrared-microwave retrieval, the subtleties of infrared radiative transfer in cloudy regions prevented the realization of the expected outcome predicted by simulations. Further work, combining the GOES infrared sounder with the SSM/T-2 or using the NOAA-K AMSU and HIRS instruments together, as proposed by Eyre (1990), might improve the results as the multiple channels of an infrared sounder may be able to accurately assign a cloud top height to infrared optically thin clouds.

Table 3.1. RMS and bias for retrieval of simulated cloud properties. Liquid Water Content (LWC) (g m^{-3}), Liquid Cloud Top height (LCT) (km), Ice Water Content (IWC) (g m^{-3}), and Ice Cloud Top height (ICT) (km) for both the MW+IR and MW only methods are shown.

	LWC RMS	LWC bias	LCT RMS	LCT bias
MW+IR	0.21	0.06	0.61	-0.35
Mwonly	0.21	-0.01	0.96	-0.36

	IWC RMS	IWC bias	ICT RMS	ICT bias
MW+IR	0.03	-0.02	2.81	2.09
Mwonly	0.20	0.15	2.24	1.84

Table 3.2. List of the ocean radiosonde sites used in the validation study. Barbados (BDI), used in the present evaluation, is shown in boldface typeset.

ID	WMO#	lat (°W)	lon (°N)	Location
ACC	78988	12.18	68.97	Curacao / Willemstad, NA
ACM	78866	18.05	63.12	St. Martin / Juliana, NA
BDI	**78954**	**13.07**	**59.50**	**Seawell Apt, BA**
FFR	78897	16.27	61.52	Point A Pitre / Raizet, GU
JSJ	78526	18.43	66.00	San Juan / Isla Verde, PR
KJP	78397	17.93	76.78	Kingston / Palisades, JA
KPP	78970	10.58	61.35	Trinidad / Piarco IAP, TR
SDQ	78486	18.47	69.88	Santo Domingo, DR
XKF	78016	32.27	64.85	Bermuda /St. George, BE

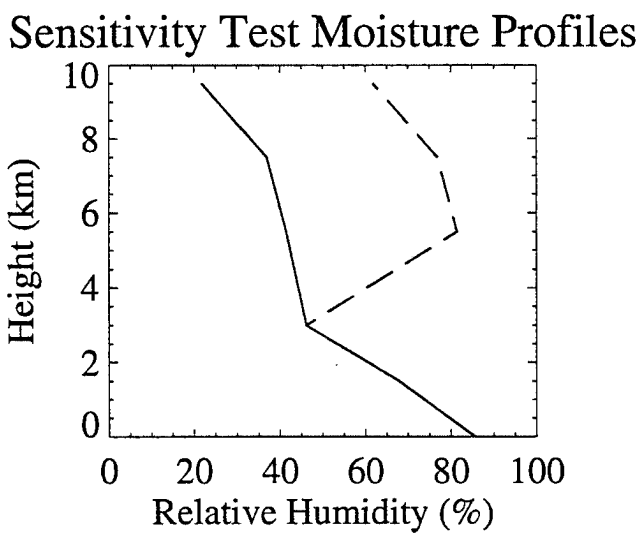

Figure 3.1. Moisture profiles used in sensitivity tests: dry upper tropospheric humidity (solid) and moist upper tropospheric humidity (dash).

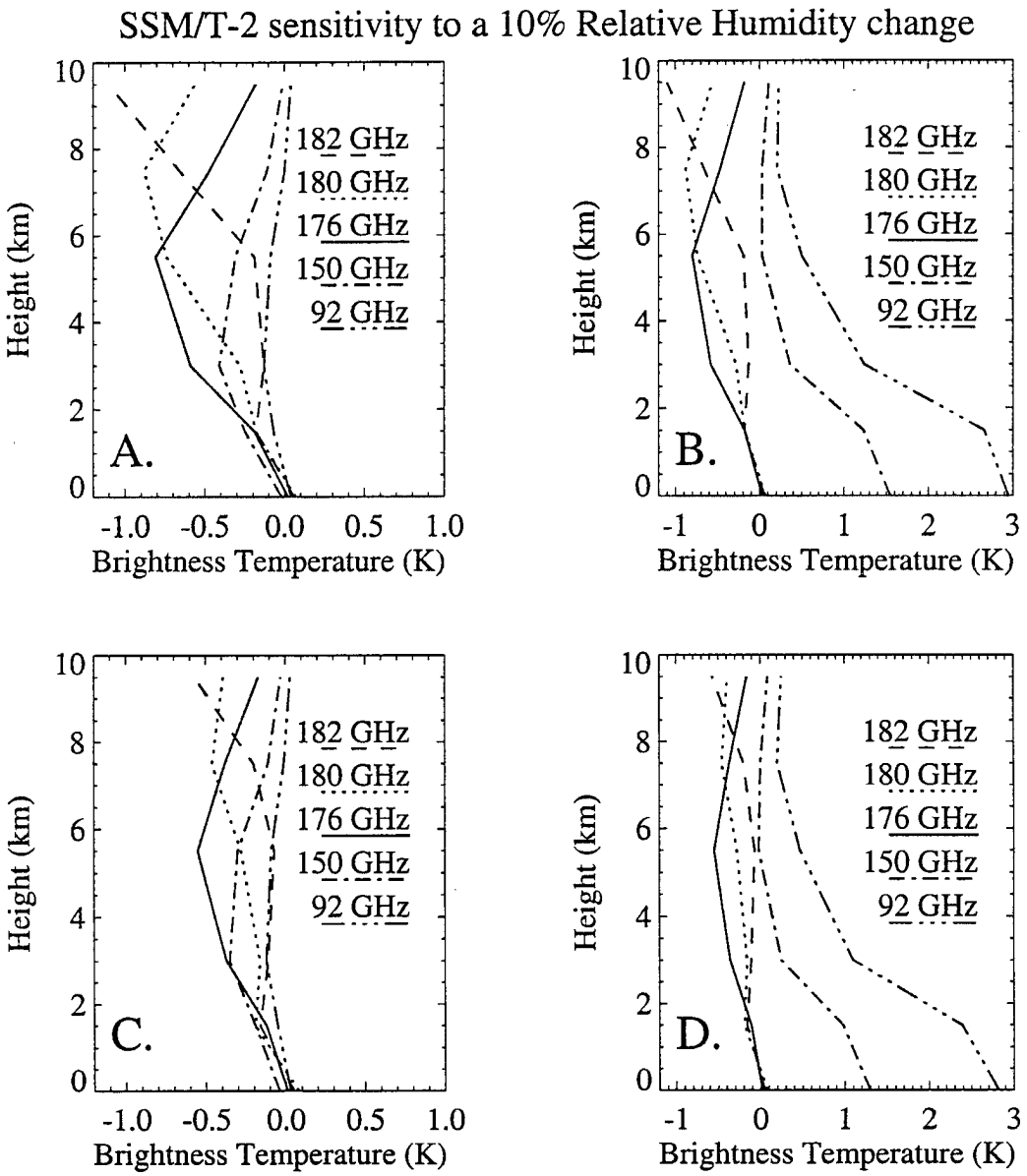

Figure 3.2. Brightness temperature change in response to a 10% relative humidity increase at the corresponding level for the SSM/T-2 sounder. (A.) dry upper troposphere over land, (B.) dry upper troposphere over ocean, (C.) moist upper troposphere over land, (D.) moist upper troposphere over ocean.

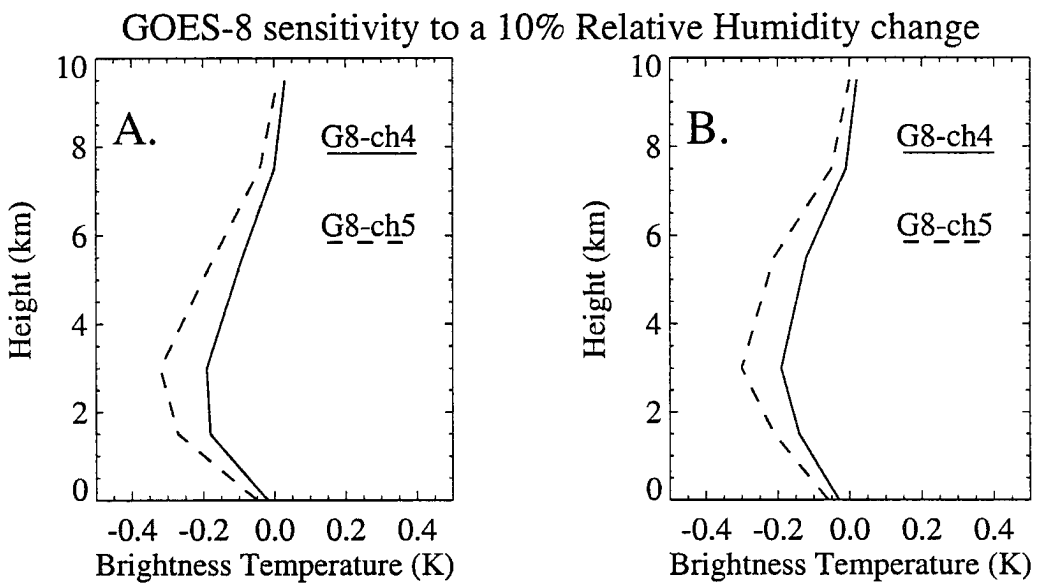

Figure 3.3. Brightness temperature change in response to a 10% relative humidity increase at the corresponding level for the GOES-8 imager channels 4 and 5. (A.) dry upper troposphere (B.) moist upper troposphere.

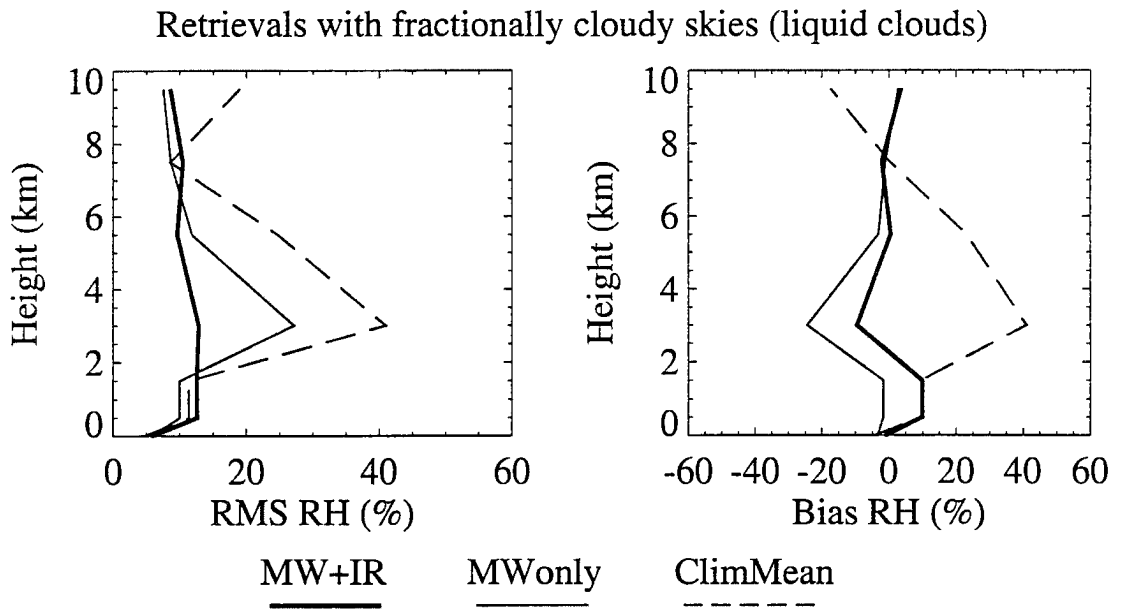

Figure 3.4. RMS and Bias for MW+IR and MW-only retrievals using synthetic data: Cloud liquid water = 0.4 g m^{-3}, Cloud top height = 4.0 km, Cloud thickness = 1.0 km, Cloud fraction = 0.5.

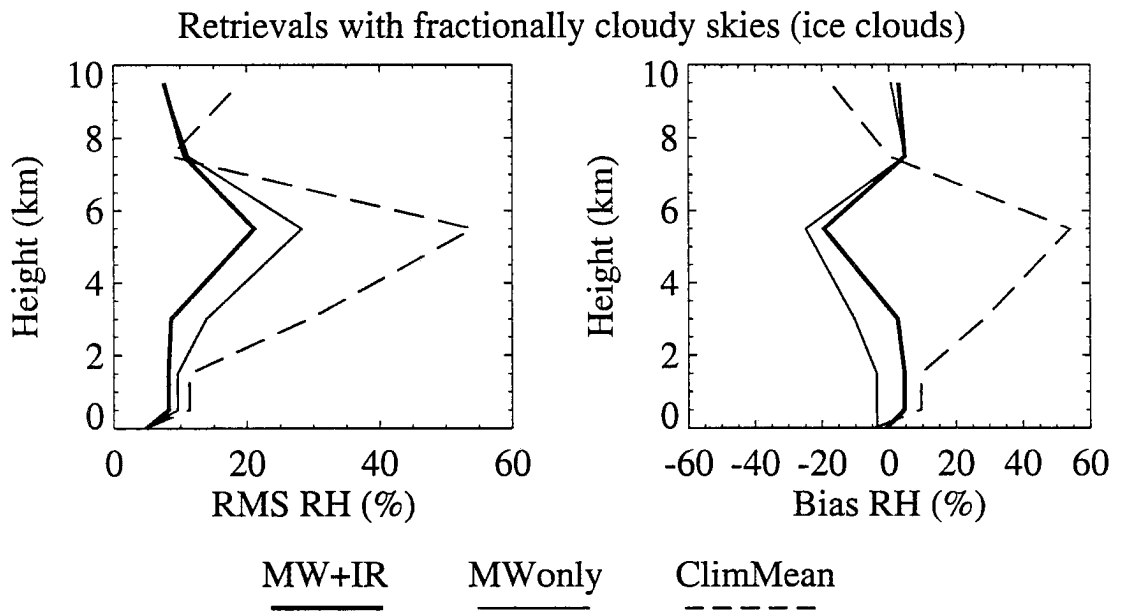

Figure 3.5. RMS and Bias for MW+IR and MW-only retrievals using synthetic data: Cloud ice water = 0.04 g m^{-3}, Cloud top height = 6.0 km, Cloud thickness = 1.0 km, Cloud fraction =0.5.

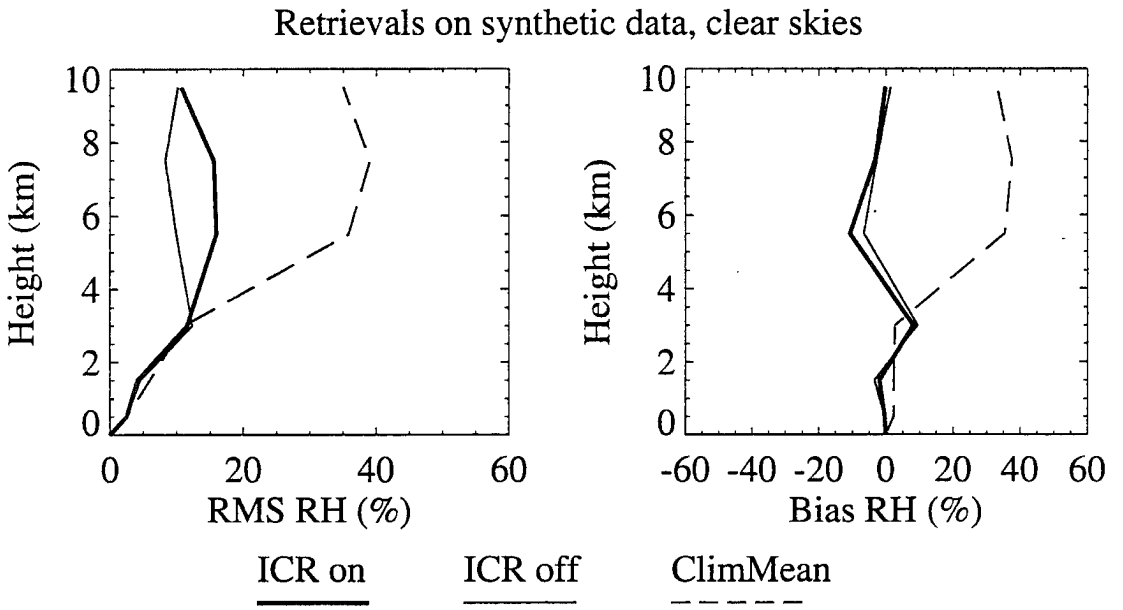

Figure 3.6. RMS and Bias for MW-only retrievals using synthetic data over ocean. Simulated condition is clear sky with high upper tropospheric humidity. Ice Cloud Retrieval (ICR) enabled (heavy solid) and disabled (thin solid). Also plotted are the RMS and bias for the truth-climatological mean difference (dash).

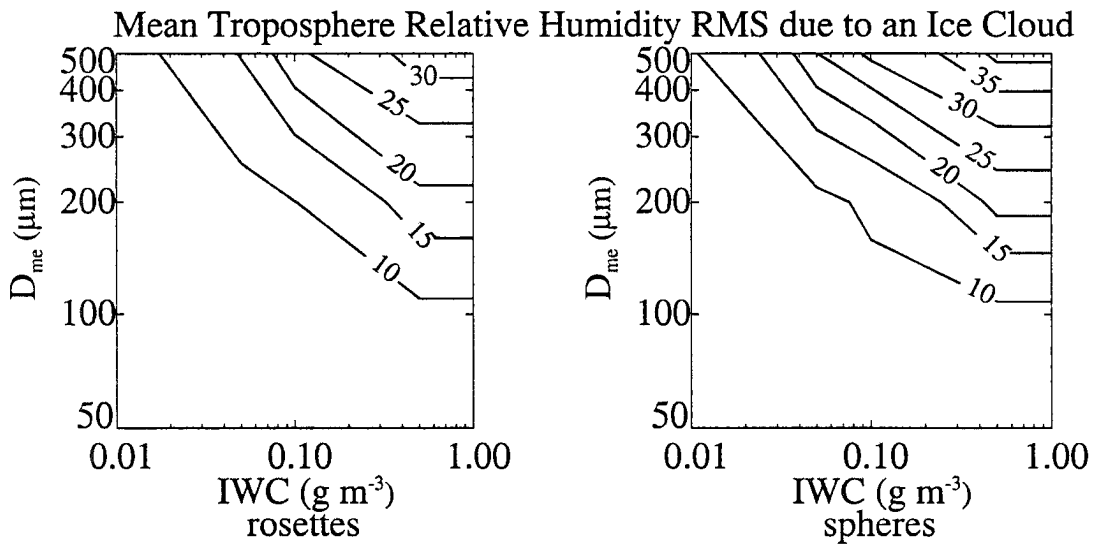

Figure 3.7. RMS for the 0-10 km layer average as a function of IWC and D_{me} for the MW-only retrieval using synthetic data over ocean. Simulated condition is cloudy sky: ice cloud (IC) fraction = 1.0, IC top = 9.0 km, IC thickness = 1.0 km. Ice Cloud Retrieval is *disabled*. Calculations for 5-column rosettes and for spheres are shown.

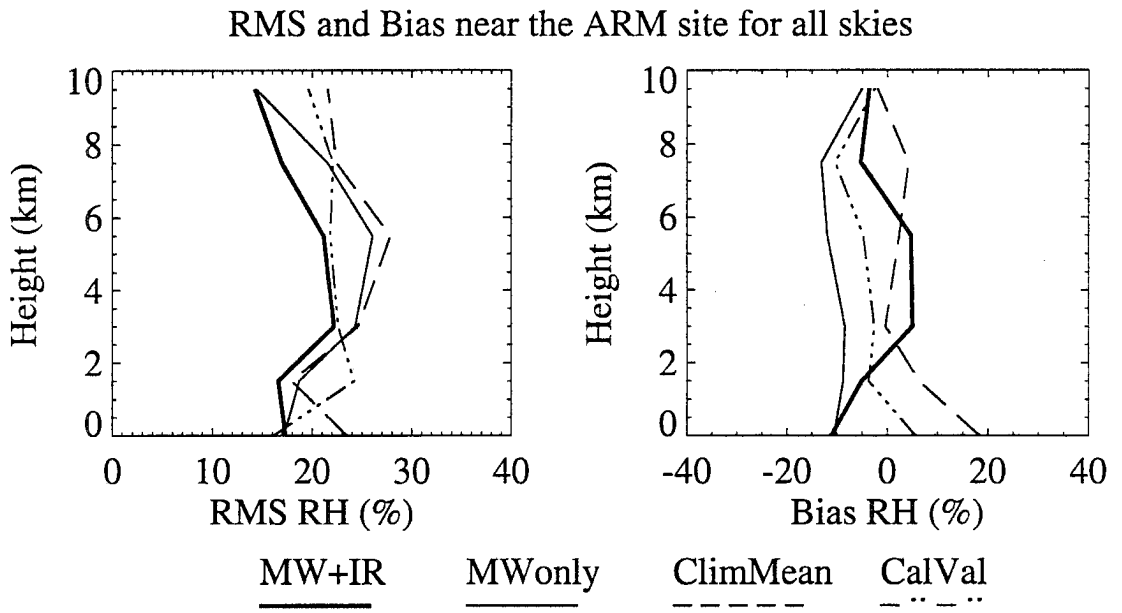

Figure 3.8. RMS and Bias for MW+IR (heavy solid) and MW-only (thin solid) moisture profile retrievals near the ARM site during all sky conditions. Also plotted are the RMS and Bias for the RAOB-climatological mean difference (dash), and the CalVal RMS and Bias (dash-3dot).

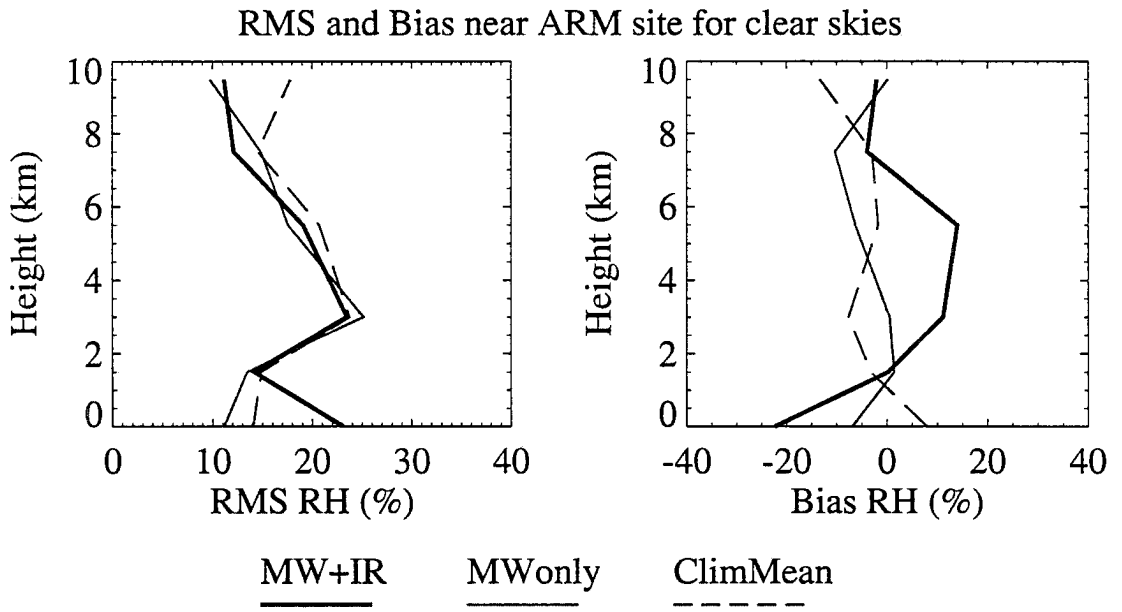

Figure 3.9. Same as Figure 3.8, but during clear sky conditions.

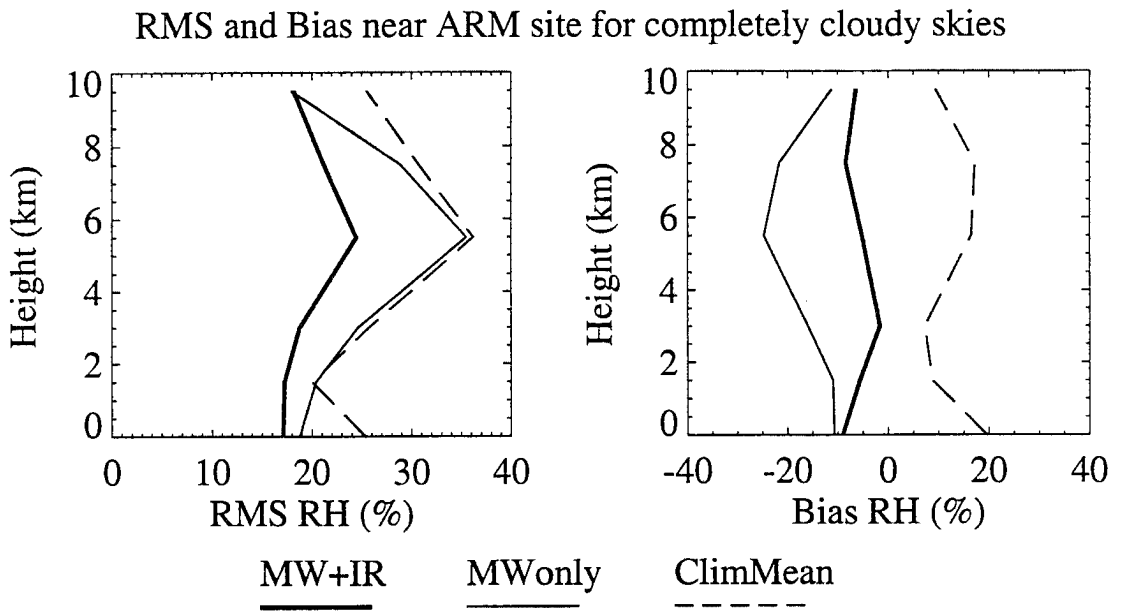

Figure 3.10. Same as Figure 3.8, but during completely cloudy sky conditions.

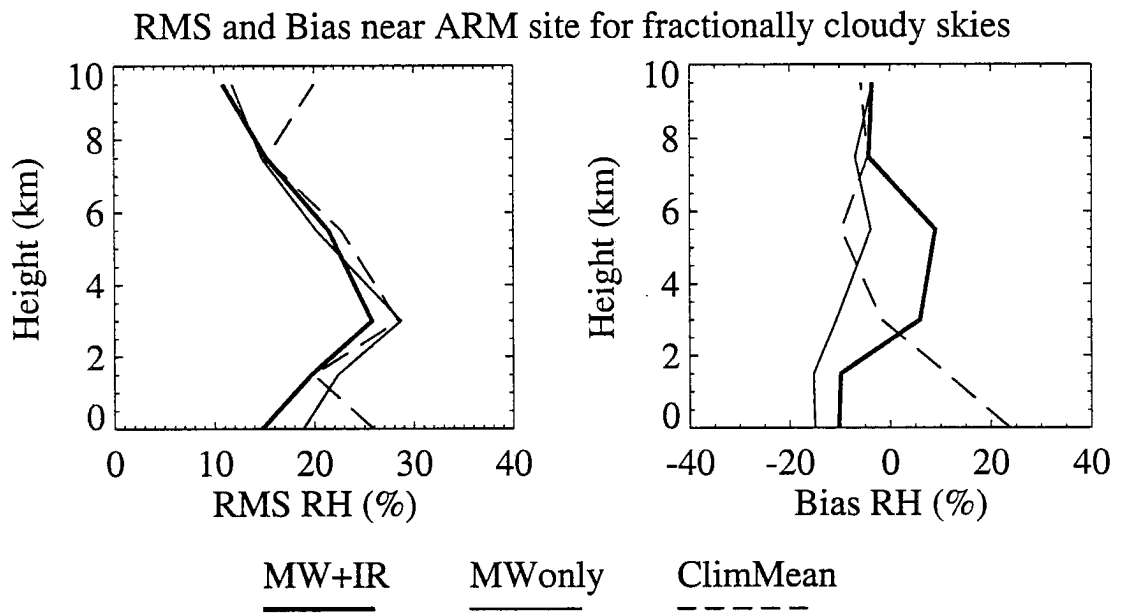

Figure 3.11. Same as Figure 3.8, but during fractionally cloudy sky conditions.

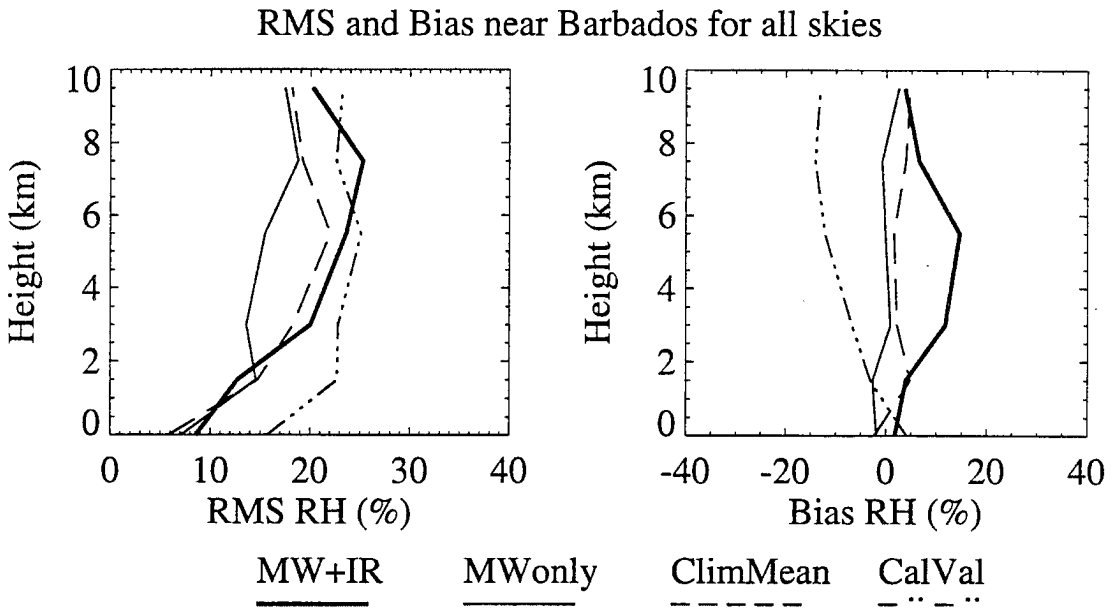

Figure 3.12. RMS and Bias for MW+IR (heavy solid) and MW-only (thin solid) moisture profile retrievals near Barbados during all sky conditions. Also plotted are the RMS and Bias for the RAOB-climatological mean difference (dash), and the CalVal RMS and Bias (dash-3dot).

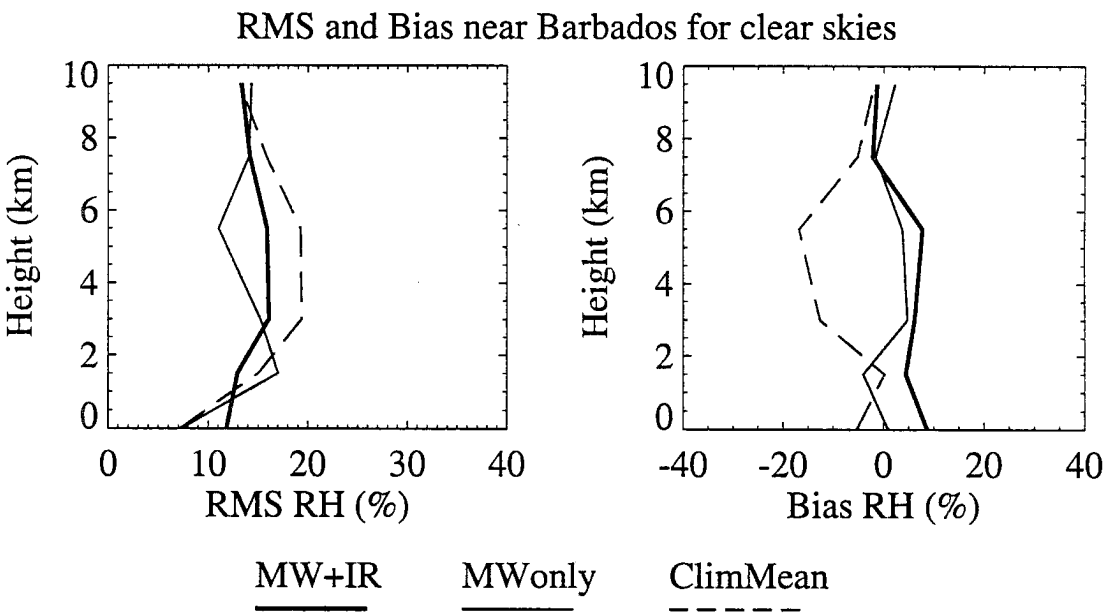

Figure 3.13. Same as Figure 3.12, but during clear sky conditions.

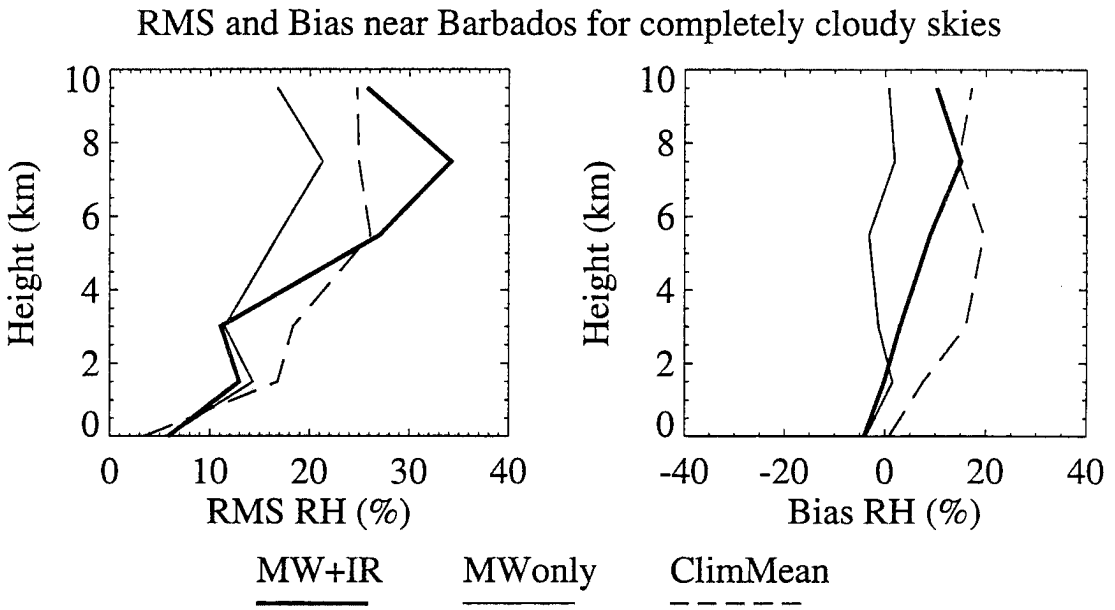

Figure 3.14. Same as Figure 3.12, but during completely cloudy sky conditions.

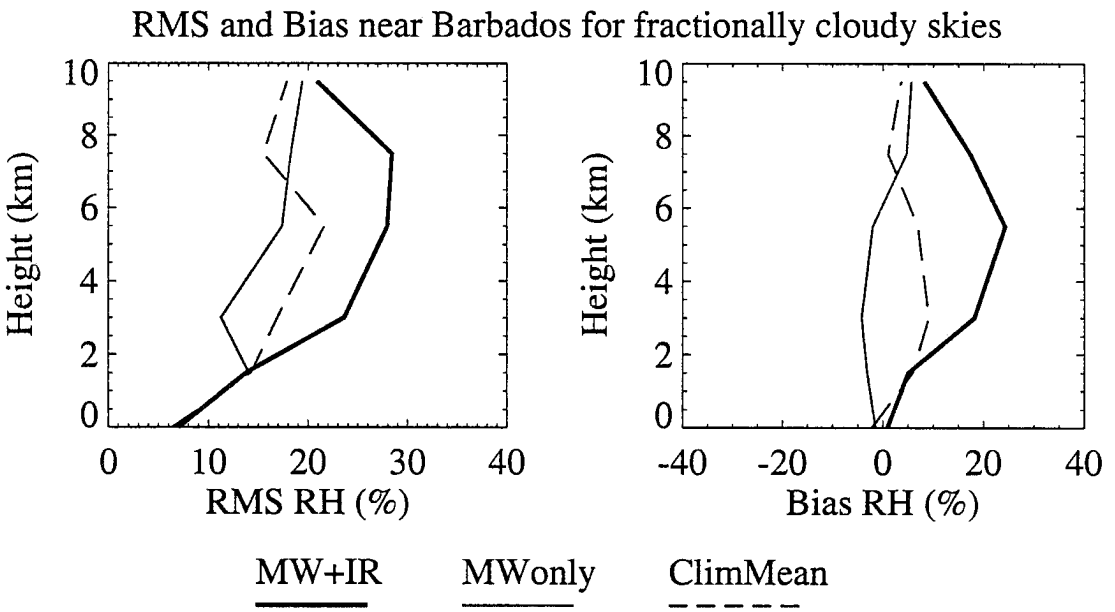

Figure 3.15. Same as Figure 3.12, but during fractionally cloudy sky conditions.

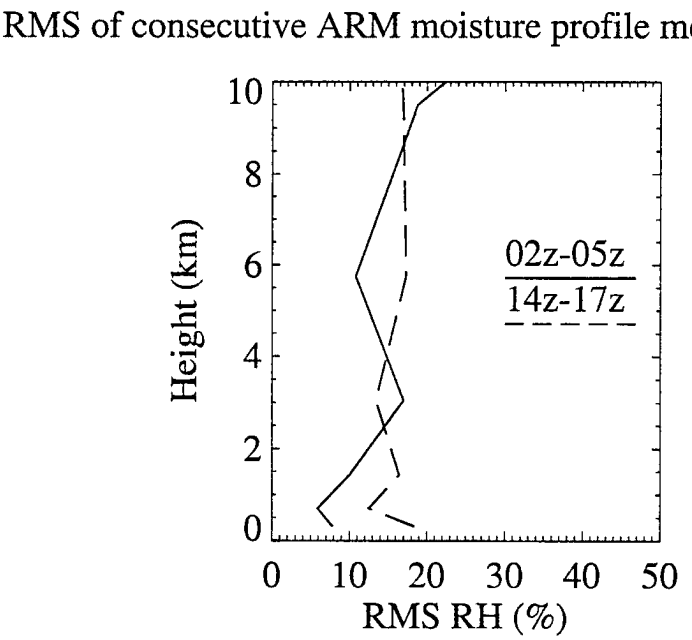

Figure 3.16. RMS of the difference of consecutive ARM relative humidity profile measurements: 0230-0530 UTC (solid) and 1430-1730 UTC (dash).

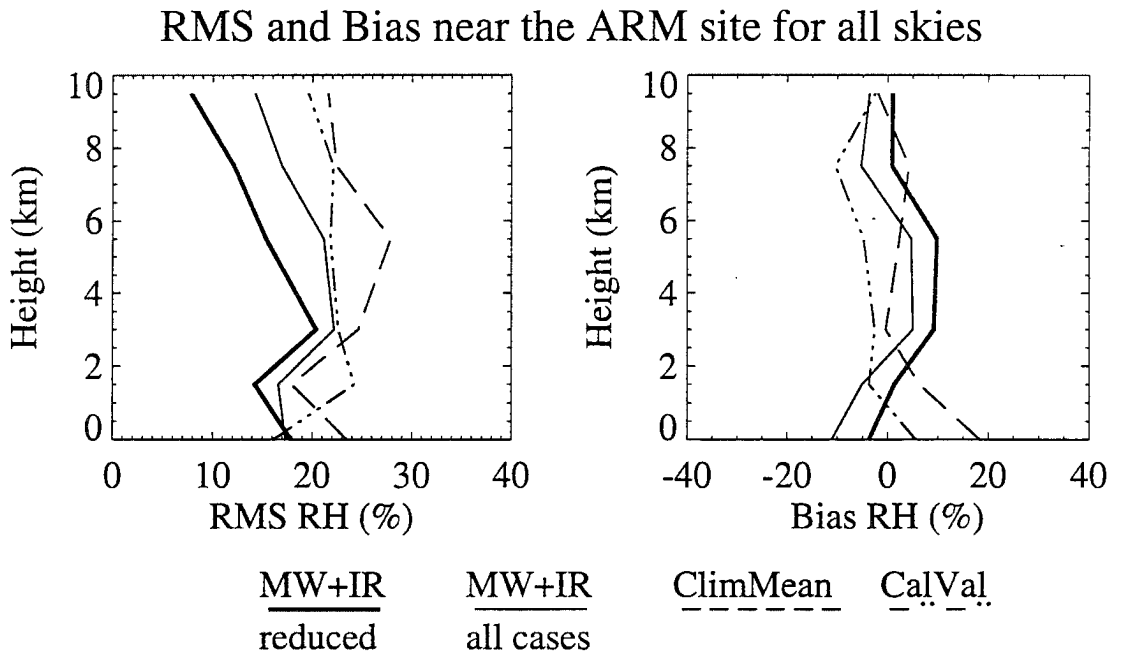

Figure 3.17. RMS and Bias for MW+IR reduced set (heavy solid) and MW+IR all cases (thin solid) moisture profile retrievals near the ARM site during all sky conditions. The reduced set contains those soundings with lower variability (see text).

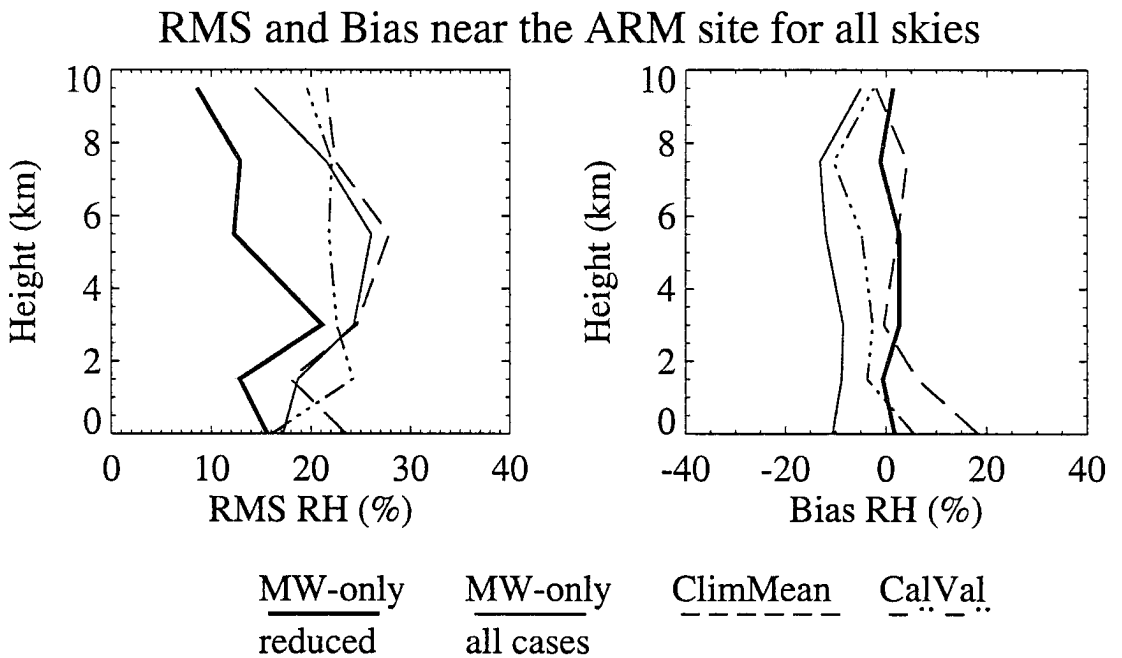

Figure 3.18. Same as Figure 3.17 but for MW-only reduced set (heavy solid) and MW-only all cases (thin solid).

4 Moisture Product Description

A moisture profile and cloud water product was produced using the BWR algorithm in the microwave-only mode. This data set was developed to study the spatial and temporal evolution of the intertropical convergence zone in the eastern Pacific during the boreal spring. The methods and input data used to produce this product are described. The mean state and variability of the retrieved moisture profile and cloud water is also documented. Various elements of the retrieved product are compared to other data available for climate studies in the eastern Pacific. Finally, the vertical variability of the relative humidity profile in the eastern Pacific is quantified using radiosonde, BWR retrieved, and NCEP reanalysis moisture profiles. The primary purpose of this chapter is to show that the moisture profile/cloud product produced using the BWR algorithm is consistent with other data and capable of capturing the natural variability of the non-precipitating atmospheric hydrologic cycle within the tropical eastern Pacific.

4.1 General description

The microwave-only version of the BWR algorithm, described in chapter 2 and evaluated in chapter 3, was used to produce a moisture profile product to examine the hydrologic cycle of the eastern Pacific ITCZ. NCEP/NCAR Reanalysis daily averaged temperature profiles were used as the auxiliary temperature data and F12 SSM/T-2 microwave sounder brightness temperatures were used as the observations. The relative humidity profile prior probability distribution was calculated from thirty days of

NCEP/NCAR Reanalysis relative humidity profiles for each month: March, April, and May, within each year, 1995 through 1997. The relative humidity at six levels (0.0 1.5, 3.0, 5.5, 7.5, and 9.5 km) as well as cloud liquid water content, liquid cloud top height, cloud ice water content, ice cloud top height, and microwave surface emissivity parameter-1 were retrieved over the ocean for the region: 15° N to 15° S, 165° W to 75° W. The assumptions about cloud thickness and particle size, as well as other auxiliary inputs, were the same as those used for the evaluation process (Table 2.2). A profile was retrieved for each SSM/T-2 observation within the region for the time period: March 1 through May 31 for the years 1995, 1996, and 1997. Due to missing data from the SSM/T-2, there is a 17 day gap in the retrievals from May 11 to May 27, 1997. The 50 km resolution, twice daily retrieved profiles were then averaged spatially and temporally to daily, one degree latitude-longitude grids. This moisture product, named *BWRT2*, serves as the basis for the investigation of the evolution of the ITCZ complex during the warm season in the tropical eastern Pacific. The remainder of this chapter quantifies the mean state and variability of the BWRT2 moisture product and compares it to other observations and analyses.

4.2 Mean state and variability of the moisture profile

Since the mean state and variance of the three dimensional structure of the moisture field in the tropical eastern Pacific has not been documented, it is important to show some of the climatological features captured by the BWRT2 retrieval. Monthly and seasonal means and their temporal standard deviations illustrate the basic state and variability of the atmospheric moisture and cloud fields. Examining the variability of the moisture field in both the horizontal and vertical coordinates can provide insight on the maintenance of atmospheric moisture within the tropical general circulation. A description of the mean state and temporal variability of the BWRT2 relative humidity

profile is illustrated by height-latitude and height-longitude cross sectional means and temporal standard deviations. Figure 4.1 shows height-latitude cross sections of the relative humidity mean and temporal standard deviation for April 1996 and April 1997 at 110° W. Figure 4.2 shows similar cross sections for the March through May time period. These cross sections illustrate the retrieved mean state relative humidity profile and its temporal variability as a function of latitude. These figures also show how the mean state humidity profile changes from year to year and from monthly to seasonal. The standard deviation cross sections illustrate the highly variable free tropospheric humidity, $\sigma > 15\%$ for most of the mid and upper levels in these cross sections, and the low variability of the boundary layer moisture , $\sigma \sim 5\text{-}10\%$, on both monthly and seasonal time scales. The ITCZ is located north of the equator most of the time during this analysis as seen in the height-latitude cross sections—elevated humidity values are the norm at 10° N, whereas suppressed humidity values are present at 10° S. Similarly, some evidence of the Walker circulation is present—elevated humidity values at 160° W and suppressed humidity values at 100° W as shown in the height-longitude cross sections of Figure 4.3 and Figure 4.4. Comparing seasons (MAM) from year to year (1996 to 1997) indicates that the moisture profile in the upper levels is drier and less variable in 1996 than in 1997. This would tend to indicate that the convection (using elevated values of upper level moisture as an indicator) in the eastern tropical Pacific during MAM was more frequent in 1997 than in 1996. Using the same indicator, the height-longitude cross section shows that the Walker Cell was stronger (more convection at 160° W, stronger subsidence at 110 ° W) in 1996 than in 1997. Figure 4.5 shows height-time cross sections of the weekly mean relative humidity profile at 8° N, 110° W and 8° S, 110° W. These plots illustrate the temporal variability of the moisture profile at two locations as a function of time for two sequential MAM seasons (1996, 1997). It is clear that the temporal variability of the relative humidity profile at these two locations is disparate. Figure 4.5 indicates that the

onset of convection at 8° N, 110° W occurred during the first week of April, 1996 (week 4), as the mid and upper tropospheric relative humidity values became quite elevated. The height-time cross sections at 8° S, 110° W are considerably different than those at 8° N. The mid and upper troposphere is more moist in the south than in the north during March for both 1996 and 1997. It appears that a 30 day wave is discernable by elevated humidity levels in the south, but not apparent (probably masked by the convective activity) in the north. These height-time cross sections show that, using SSM/T-2 observations, the BWR algorithm is able to capture the variability of the moisture profile in the eastern tropical Pacific as a function of time and space without any sophisticated statistical measures. A more extensive analysis of convection will be presented in chapters 5 and 6.

In addition to relative humidity profiles, the BWRT2 product calculates a cloud liquid water and a cloud ice water product. Although the cloud liquid water product is not new, it is necessary to retrieve cloud liquid water in order to get the relative humidity profile in cloudy regions. As will be seen in section 4.3.1, the cloud liquid water product retrieved by the BWR algorithm is in general agreement with that of an SSM/I derived product. The cloud ice water product is new, and together the BWRT2 cloud water products can be used to infer the areal extent and depth of convection within the central and eastern tropical Pacific region. Since the ice water retrievals are based on very simplistic assumptions concerning cloud thickness and particle size and shape, and since retrieval validation was not possible, the ice water content presented here should be viewed only qualitatively. Figure 4.6 shows the mean and temporal standard deviation of the cloud liquid water content as a function of latitude and longitude for April 1996 and 1997. Similar plots of ice water content are shown in Figure 4.7. Figure 4.8 and Figure 4.9 show the same quantities for the MAM time period. Since the cloud water contents were retrieved assuming a 1.0 km thick cloud, the values for liquid and ice water content

($g\ m^{-3}$) and liquid and ice water path ($kg\ m^{-2}$) are interchangeable. As seen in these plots, the April mean cloud liquid and ice water are significantly different from 1996 to 1997. Furthermore, the standard deviation of the cloud liquid and ice water contents for April are also very different between years. The same assessment holds true for the cloud liquid and ice water contents during the MAM time period. These figures illustrate the variability of the retrieved cloud water properties. The simple comparison of monthly and seasonal means and their standard deviations between consecutive years shows that the BWRT2 product is quite capable of capturing the variability of several components of the atmospheric hydrologic cycle in the eastern and central tropical Pacific region.

4.3 Comparison with other products and analyses

4.3.1 SSM/I derived cloud liquid water

Since the temporal collocation of coincident SSM/I (F11 and F13, no SSM/I instrument is operational on the F12 satellite) derived liquid water measurements and SSM/T-2 (F12) derived liquid water measurements (BWRT2) is poor (~4 hours), no effort was made to validate the liquid water retrieved by the BWR algorithm using the SSM/I cloud water product. Although not suitable for cross-sensor/algorithm validation, a comparison of the BWRT2 and SSM/I derived cloud liquid water estimates is worthwhile. A favorable comparison might extend the BWRT2 CLW product from qualitative to quantitative. SSM/I derived cloud liquid water measurements (Greenwald *et al.*, 1995) for April 1, 1996 are compared to BWRT2 cloud liquid water measurements for the same day in Figure 4.10a. This scatter plot, with a linear correlation coefficient of 0.60, shows that the two independent measurements are in agreement. Many factors could be contributing to the spread in this scatter plot. For example, the SSM/I derived liquid water was calculated using radiances measured by the DMSP F13 satellite ,

whereas the BWRT2 product used the F12 satellite. These satellites have equatorial crossing times that differ by approximately 3.5 hours. Additionally, the field of view sizes for the SSM/I and SSM/T-2, as well as the scan angles are very different. The cloud water data that are plotted in Figure 4.10 are a one degree latitude-longitude average of the original retrievals which also may have introduced error. For April 1, 1996, the mean cloud liquid water path for data points with a value greater than 0.01 kg m^{-2} from the SSM/I product was 0.11 kg m^{-2} and for the BWRT2 product it was 0.12 kg m^{-2}. The RMS of the difference between the two products was 0.003 kg m^{-2}. Figure 4.10b shows a scatter plot of the SSM/I derived liquid water on April 25, 1996, and the BWRT2 liquid water on April 1, 1996. This plot, with a correlation coefficient of 0.13 shows that the SSM/I product and the BWRT2 product are not in agreement when they are not supposed to be. The degree of the lack of correlation in Figure 4.10b gives some credence to the degree of correlation in Figure 4.10a. The results from the comparison of cloud liquid water indicate that the BWRT2 algorithm and SSM/I algorithm (Greenwald *et al.*, 1995) are in agreement.

4.3.2 Reanalysis relative humidity profiles

Until now, the reanalysis and operational analysis products available from the major forecast centers, like NCEP and ECMWF, were the only atmospheric moisture profile products available in data sparse, cloudy regions like the tropical Pacific. Many researchers have used these analyses to describe various aspects of the climate system. Therefore, it would be remiss not to compare the BWRT2 moisture profile to at least one of the reanalysis products. Both the NCEP and ECMWF assimilate TOVS radiances into their analyses in order to improve the product in data sparse regions. Since the tropical Pacific is frequently cloudy, the infrared sounder used to estimate water vapor profiles is expected to be of little use. Since the BWR algorithm used NCEP temperature profiles as

auxiliary data and NCEP relative humidity profiles for the prior distribution, it is appropriate to compare the BWRT2 product to the NCEP reanalysis relative humidity profiles. It might be expected that since the BWR algorithm used the NCEP moisture profiles to calculate the prior probability distribution that the NCEP moisture profiles would compare favorably to the retrieved profiles. This is not the case. A comparison of the BWRT2 relative humidity profiles and the NCEP Reanalysis relative humidity profiles illustrates some significant differences. Figure 4.11 and Figure 4.12 show the relative humidity RMS for the BWRT2-NCEP difference as well as the mean profile for each. These figures illustrate that there is a significant disagreement between the retrieved humidity and the reanalysis humidity especially at the upper levels of the troposphere. RMS and bias of 40% in relative humidity units are not uncommon at 9.0 km. Even though the NCEP relative humidity profiles are effectively constraining the inversion, the retrieved humidity profiles are significantly different (RMS > 20%) above 2 km. Analysis of radiosonde data (not shown) indicates that the boundary layer moisture content has little variability over tropical oceanic regions. The standard deviation of the surface relative humidity is about 6%. The NCEP Reanalysis humidity profiles also reflect this fact. Therefore, due to the large constraint put on the inversion by the prior distribution, it is expected that the variability of retrieved humidity near the surface will be minimal. Above 2 km, however, the BWR algorithm, using the SSM/T-2 observations, is clearly measuring some that the model analysis is incapable of resolving. The model is consistently too moist at the upper levels in nearly all regions of the central and eastern tropical Pacific. A possible explanation for the disagreement between the NCEP and BWRT2 moisture profiles lies in the assumed temperature profile. As stated earlier, NCEP temperature profile analyses are used in the retrieval process and assumed to be known. Sensitivity studies (not shown) indicate that a 2 K error in the temperature profile at a given level will translate into about a 10% error in the relative humidity at that

level. The radiosonde and drop sonde analysis of the intertropical convergence zone made during FGGE (Fernandez-Partagas and Estoque, 1985) shows the temperature change across the trough to be less than 2 K at all tropospheric levels. A limited comparison of radiosonde and NCEP temperature profiles indicates that the NCEP profiles were consistent with the observations to less than 2 K RMS. With this in mind and considering the results to be presented in section 4.3.4, it is believed that the disagreement between the NCEP and BWRT2 moisture profiles is real and not an artifact of temperature profile error.

4.3.3 Ice water content and outgoing long-wave radiation

Since there are no ice water path measurements in the tropical eastern Pacific available to validate the BWRT2 algorithm, the ice water content produced by the algorithm should be viewed as an index of the presence of cloud ice and nothing more. An interesting comparison of monthly mean AVHRR derived outgoing long wave radiation and BWRT2 monthly mean IWC for April 1996 and 1997 is shown in Figure 4.13. This figure indicates that the outgoing long wave radiation (OLR) and cloud ice water path are very much correlated in a monthly mean sense. A linear regression fit gives the following relationships:

$$OLR = 264 - 404 * IWP \qquad \text{(April 1996)}$$

$$OLR = 270 - 434 * IWP \qquad \text{(April 1997)}$$

The OLR-IWP relationship shown here is only used to aid in the estimate of an IWP threshold for the identification of deep convection (section 6.1). Further investigation of the OLR-IWP relationship is beyond the scope of this work.

4.3.4 Radiosonde measurements

Although it was shown that the BWR algorithm was able to retrieve relative humidity profiles over a tropical ocean environment (near Barbados, section 3.2.2), it is still useful to show any comparisons which are able to be made for the region in which the BWRT2 product was developed, namely the tropical eastern Pacific. Since the overpass of the F12 satellite near the Pacific coasts of Central and South America is nominally at 0230 and 1430 UTC, the global synoptic upper air sounding network would not be temporally close enough to add any confidence in the retrieval method over that achieved using Caribbean soundings. A very small number of sondes were launched from Cocos Island (5.54° N, 87.05° W) between 1330 and 1400 UTC during May 1997 as part of the PACS program. Figure 4.14 shows the relative humidity profiles retrieved by the BWR algorithm and measured by the Cocos Island sonde. These three plots show that the retrieved profile is much closer to the sonde profile than is the NCEP profile. The NCEP profile consistently has a dry bias at 7.5 km (400 mb). Although this very small number of comparisons does not constitute validation, it is encouraging to see that the BWR algorithm is able to retrieve the moisture profile under a variety of conditions.

A qualitative comparison of relative humidity profiles in and around the ITCZ is shown in Figure 4.15. This figure shows the mean relative humidity for the ITCZ and environs measured by 62 radiosonde and drop sonde measurements during the first week in June 1979. The contour plot was formed using the mean temperature and dew point depression data in the ITCZ region, as well as the northern and southern environs reported by Fernandez-Partagas and Estoque (1985). Also shown is the mean relative humidity height-latitude cross section at 100° W for the last week in May 1996, from the BWRT2 product. Although the retrieved humidity at the upper levels is somewhat higher inside the ITCZ, the general behavior of the ITCZ and environs in terms of relative humidity is similar between sonde measurements in 1979 and retrieved profiles in 1996.

4.4 Relative humidity level correlation

A test for any remote sensing algorithm is: How well does the retrieved quantity represent the natural variability of the actual quantity? A simple way to gain some insight on the ability of the BWR algorithm to represent vertical moisture profile variability is to calculate the temporal linear correlation (Press *et al.*, 1992) of the relative humidity between retrieved levels and compare that to the same calculation using nearby radiosonde measured profiles. Due to the lack of radiosondes in the eastern Pacific, no spatial linear correlation between levels is possible using radiosondes, therefore NCEP reanalysis are used for comparison.

To make an assessment of how well the BWRT2 product represents the vertical variability of the moisture profile in time, temporal level linear correlation matrices were calculated for the BWRT2 product and the Balboa (Panama) radiosonde. Table 4.1 shows temporal linear correlation of relative humidity between upper air mandatory levels from the Balboa radiosonde for March 1, 1997 through May 31, 1997. As seen in this table, the lower levels are not correlated in time with any other level, whereas the mid and upper levels tend to be somewhat correlated with nearby levels. Table 4.2 shows the temporal correlation for BWRT2 retrieved relative humidity levels off the coast of Balboa for the same time period. Here we see that the mid and upper levels tend to have a correlation pattern similar to that of the radiosonde, however, the lower levels in the BWRT2 data also tend to be more correlated. The SSM/T-2 is not able to resolve fine structure in the vertical and therefore this result is to be expected. Since the BWRT2 and radiosonde level correlation are similar, except in the boundary layer, it would be appropriate to state that the BWRT2 product captures most of the temporal vertical variability. The spatial variability of the vertical relative humidity profile for one day (April 1, 1997) is presented in Table 4.3 for the NCEP Reanalysis and in Table 4.4 for the BWRT2 product. The NCEP analysis has little correlation between levels in the

troposphere. On the other hand, the BWRT2 spatial level correlation is very similar in structure to the BWRT2 temporal level correlation, showing some correlation between nearby levels. Since the BWRT2 spatial level correlation looks similar to the temporal level correlation and that a spatial level correlation of Caribbean radiosonde data (not shown) depicts similar structure, it is believed that the BWRT2 relative humidity product is capturing most of the spatial vertical variability in the moisture field.

Table 4.1. Temporal level correlation (x100) of the Balboa, Panama upper air mandatory level relative humidity for MAM 1996. Shaded values represent greater than 60% linear correlation.

6	**25**	**18**	**37**	**60**	**70**	**100**
5	**27**	**18**	**48**	**78**	**100**	**70**
4	**36**	**31**	**52**	**100**	**78**	**60**
3	**36**	**30**	**100**	**52**	**48**	**37**
2	**07**	**100**	**30**	**31**	**18**	**18**
1	**100**	**07**	**36**	**36**	**27**	**25**
Level	**1**	**2**	**3**	**4**	**5**	**6**

Table 4.2. Temporal level correlation (x100) of the BWRT2 relative humidity near Balboa, Panama for MAM 1996. Shaded values represent greater than 60% linear correlation.

6	**25**	**49**	**20**	**68**	**91**	**100**
5	**32**	**55**	**36**	**84**	**100**	**91**
4	**48**	**50**	**65**	**100**	**84**	**68**
3	**48**	**38**	**100**	**65**	**36**	**20**
2	**66**	**100**	**38**	**50**	**55**	**49**
1	**100**	**66**	**48**	**48**	**32**	**25**
Level	**1**	**2**	**3**	**4**	**5**	**6**

Table 4.3. Spatial level correlation (x100) of the NCEP Reanalysis relative humidity for April 1, 1997 in the eastern tropical Pacific. Shaded values represent greater than 60% linear correlation.

6	09	17	43	41	67	100
5	10	12	57	64	100	67
4	06	30	59	100	64	41
3	17	41	100	59	57	43
2	12	100	41	30	12	17
1	100	12	17	06	10	09
Level	1	2	3	4	5	6

Table 4.4. Spatial level correlation (x100) of the BWRT2 relative humidity for April 1, 1997 in the eastern tropical Pacific. Shaded values represent greater than 60% linear correlation.

6	02	00	16	44	80	100
5	08	10	34	72	100	80
4	11	10	60	100	72	44
3	03	15	100	60	34	16
2	62	100	15	10	10	00
1	100	62	03	11	08	02
Level	1	2	3	4	5	6

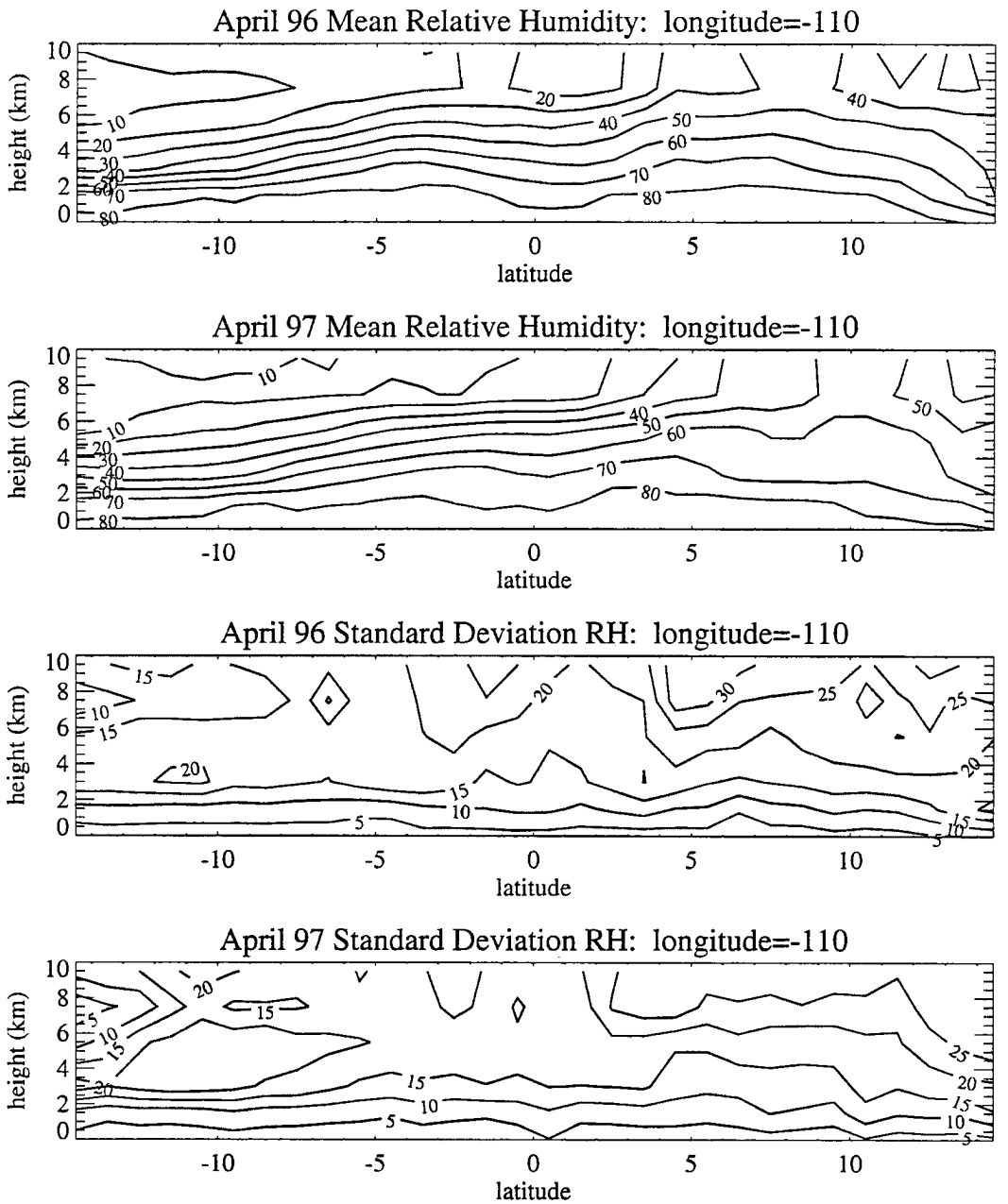

Figure 4.1. Height-Latitude cross sections of the mean relative humidity and temporal standard deviation for April 1996 and April 1997.

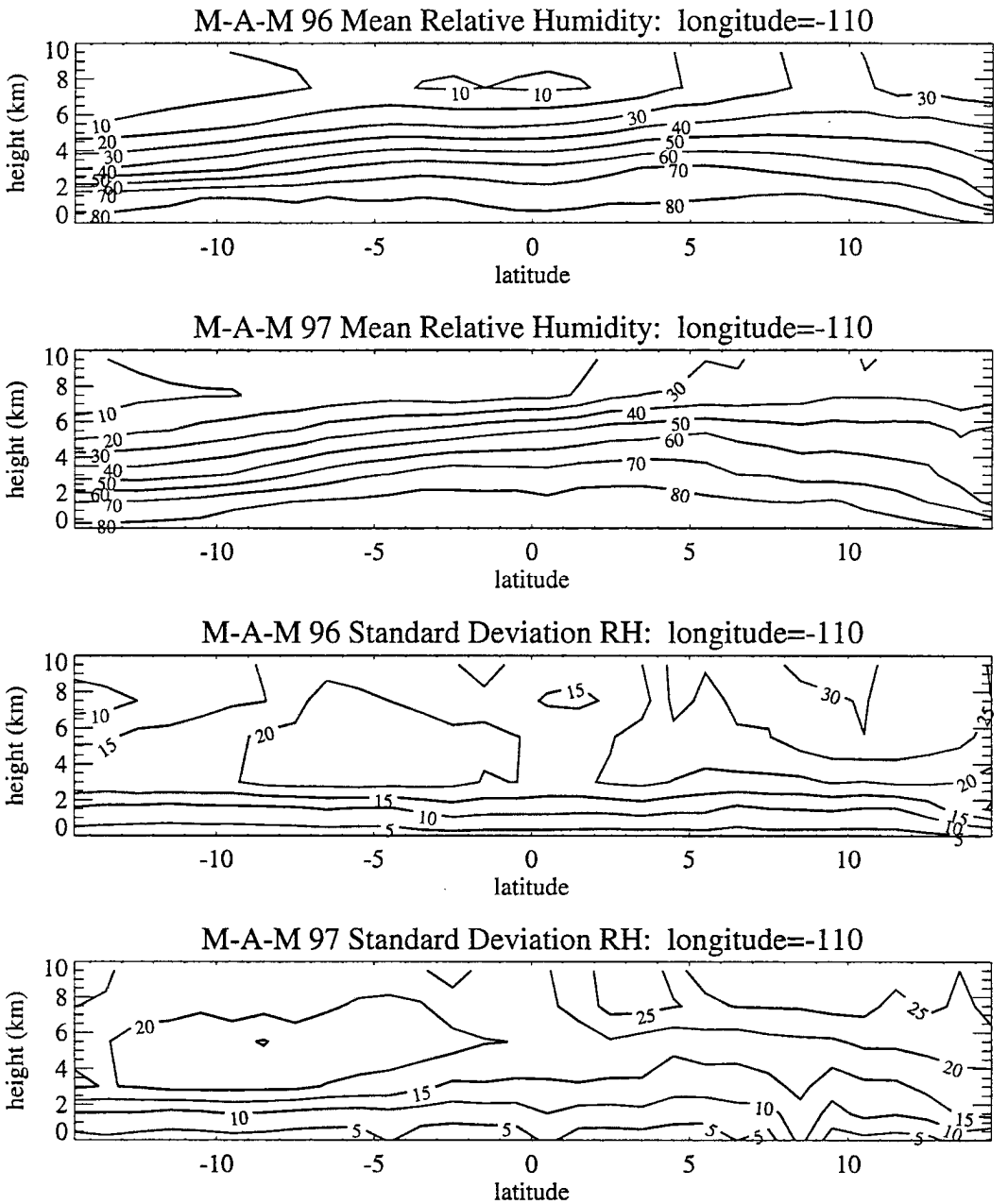

Figure 4.2. Height-Latitude cross sections of the mean relative humidity and temporal standard deviation for March-April-May 1996 and March-April-May 1997.

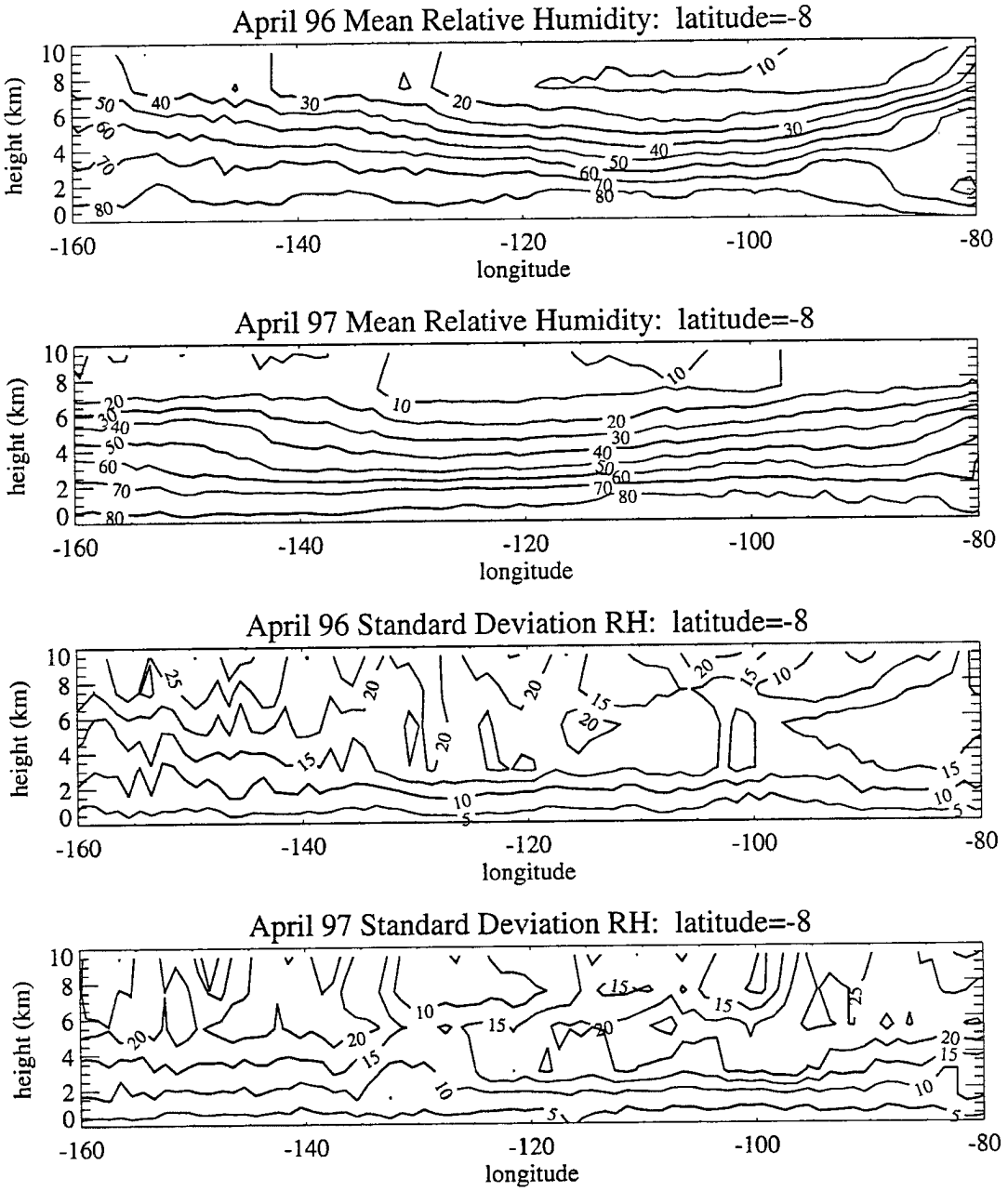

Figure 4.3. Height-Longitude cross sections of the mean relative humidity and temporal standard deviation for April 1996 and April 1997.

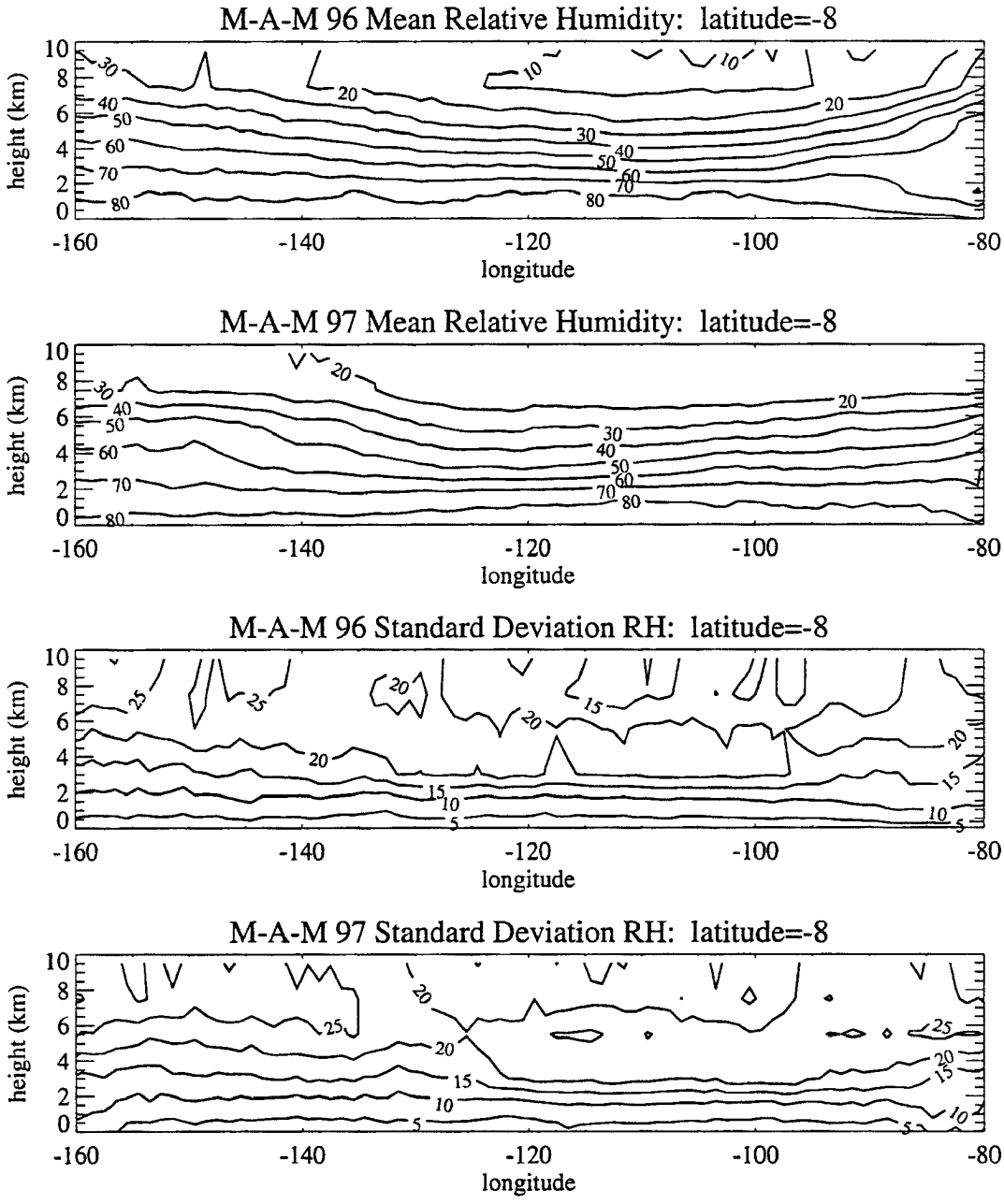

Figure 4.4. Height-Longitude cross sections of the mean relative humidity and temporal standard deviation for March-April-May 1996 and March-April-May 1997.

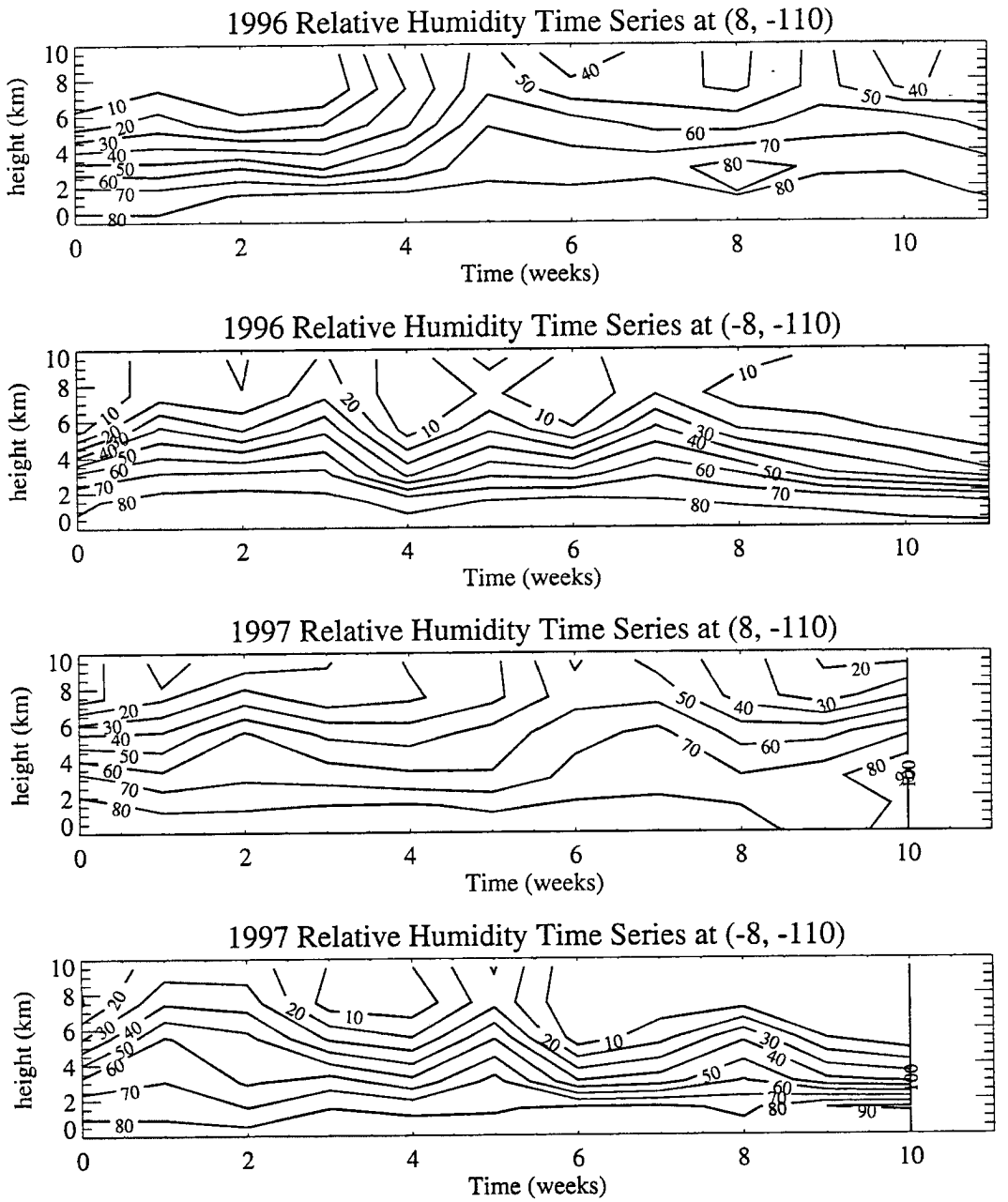

Figure 4.5. Height-Time cross sections of weekly mean relative humidity at (8° N, 110° W) and (8° S, 110° W) for March through May 1996 and 1997.

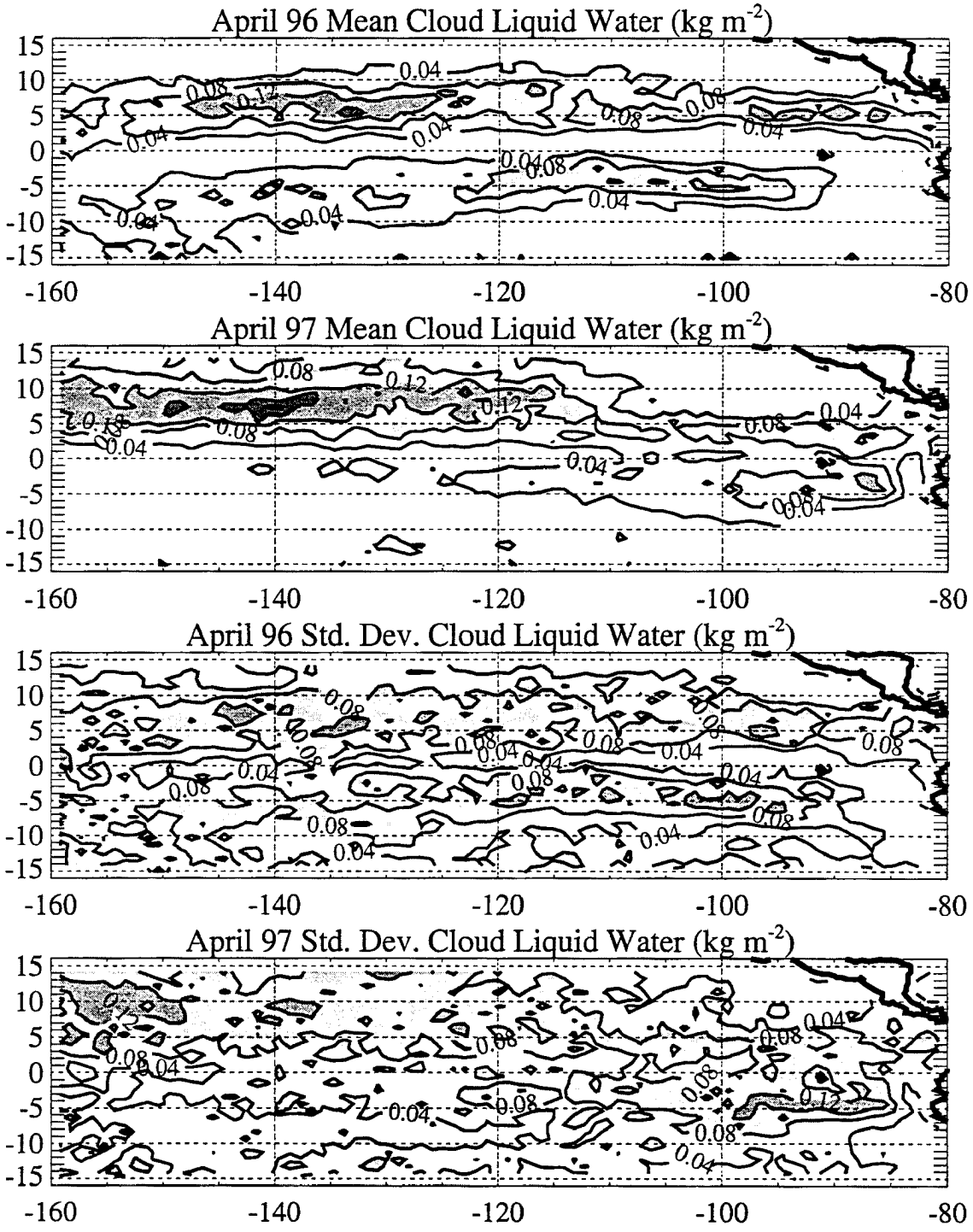

Figure 4.6. Latitude-Longitude plot of mean cloud liquid water content and standard deviation for April 1996 and April 1997.

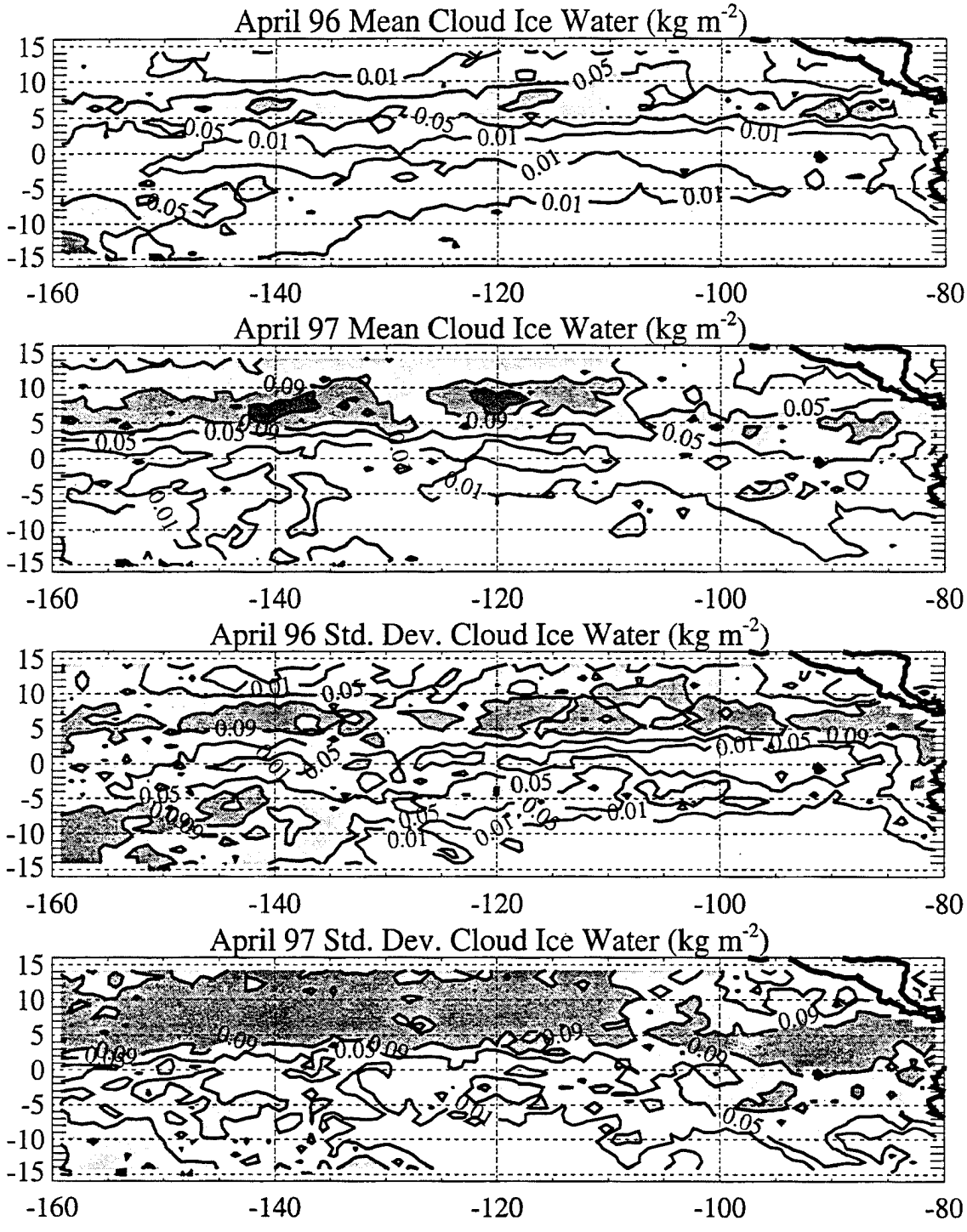

Figure 4.7. Latitude-Longitude plot of mean cloud ice water content and standard deviation for April 1996 and April 1997.

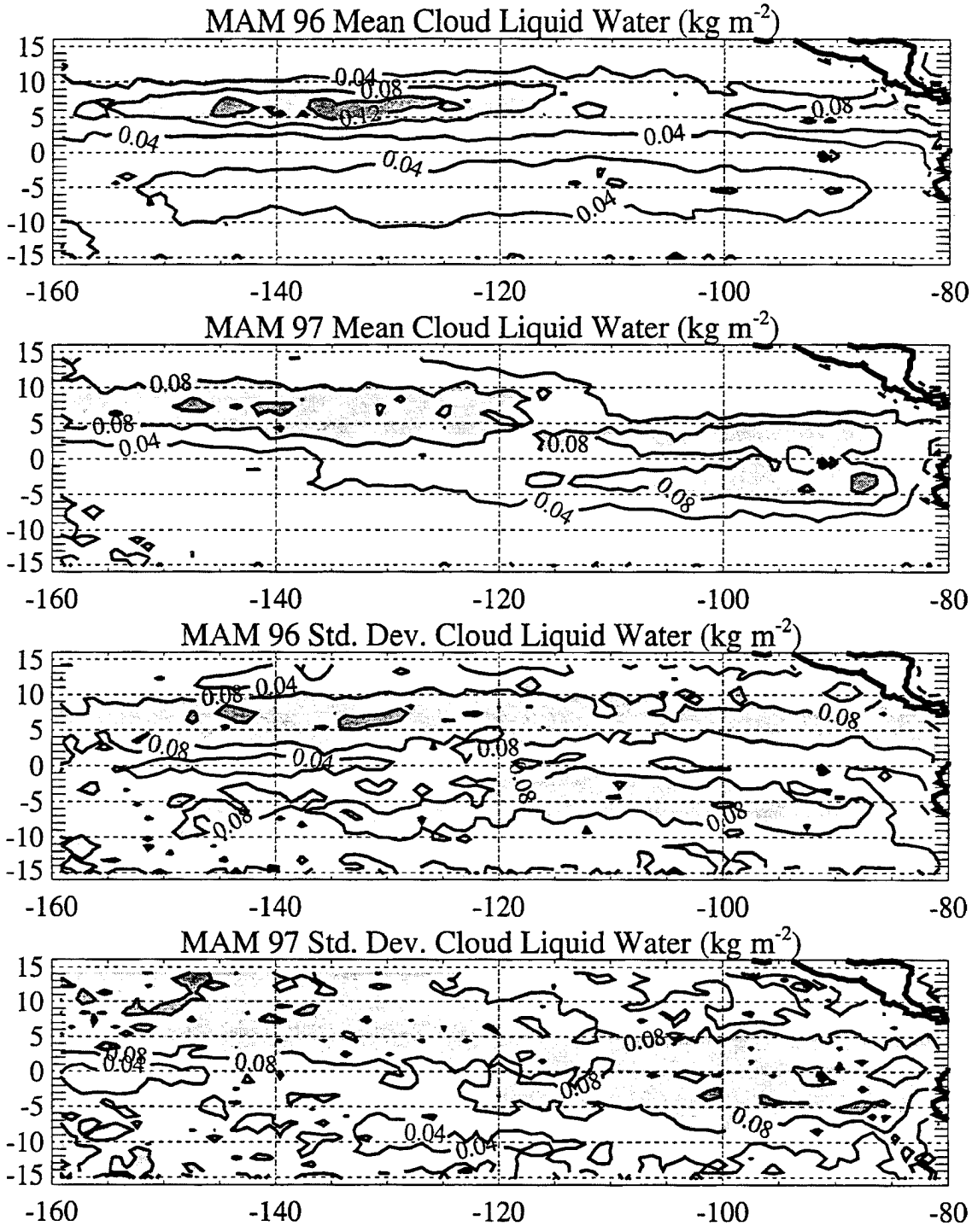

Figure 4.8. Latitude-Longitude plot of mean cloud liquid water content and standard deviation for March-April-May 1996 and March-April-May 1997.

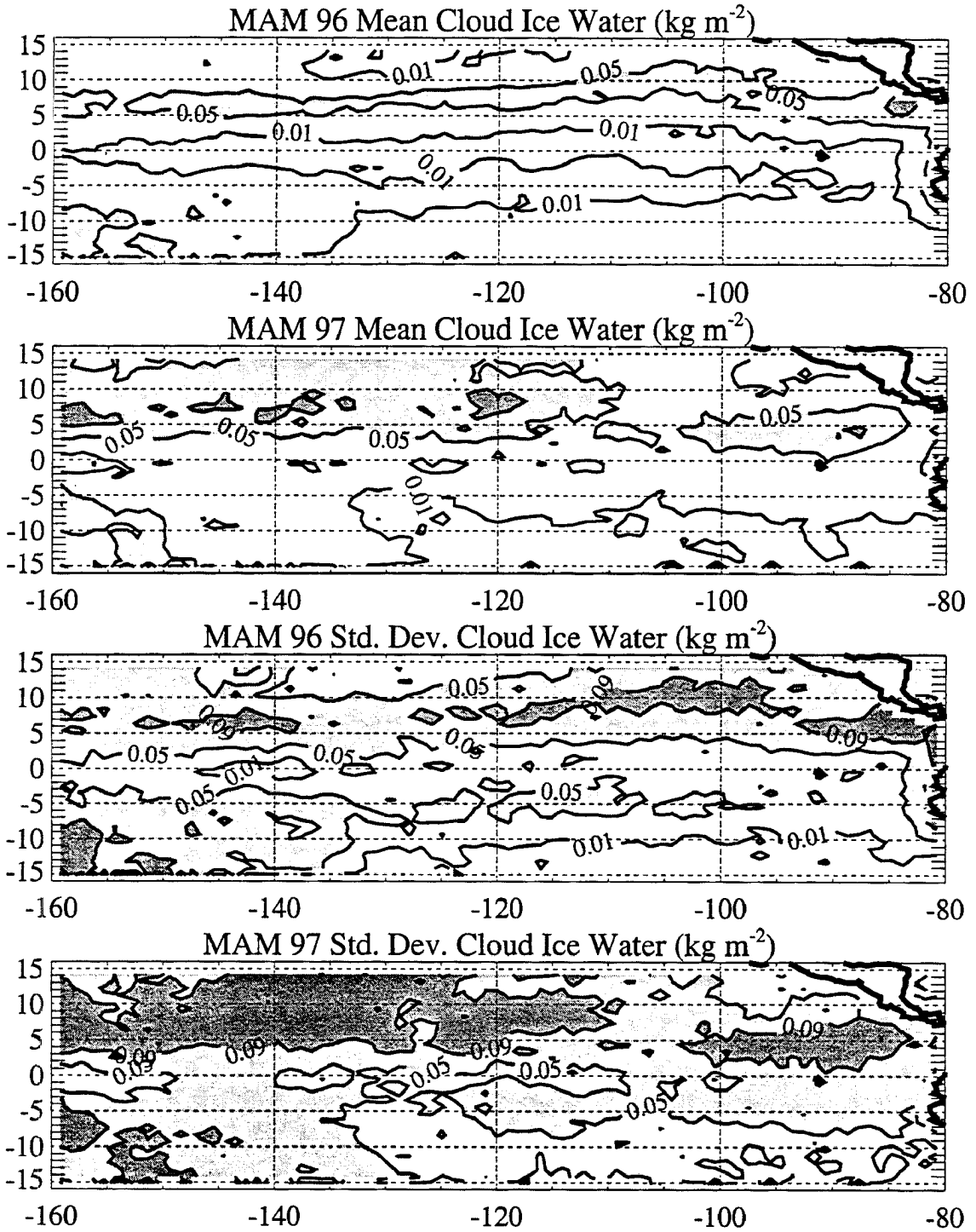

Figure 4.9. Latitude-Longitude plot of mean cloud ice water content and standard deviation for March-April-May 1996 and March-April-May 1997.

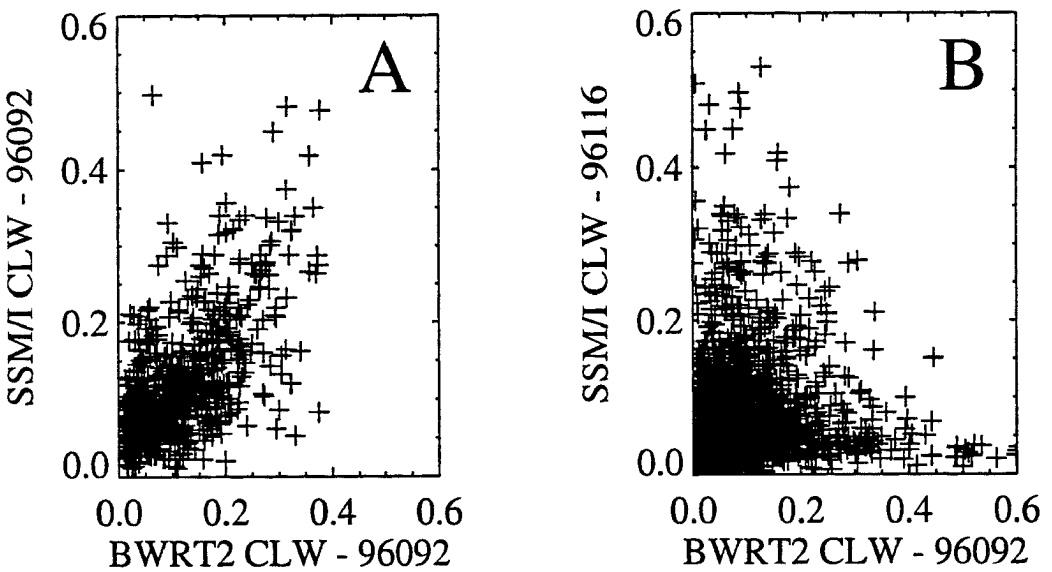

Figure 4.10. Scatter plot of SSM/I derived cloud liquid water path and BWRT2 cloud liquid water path for the eastern and central tropical Pacific for April 1, 1996 (A). Scatter plot of SSM/I derived cloud liquid water path on April 25, 1996 and BWRT2 cloud liquid water path on April 1, 1996 (B).

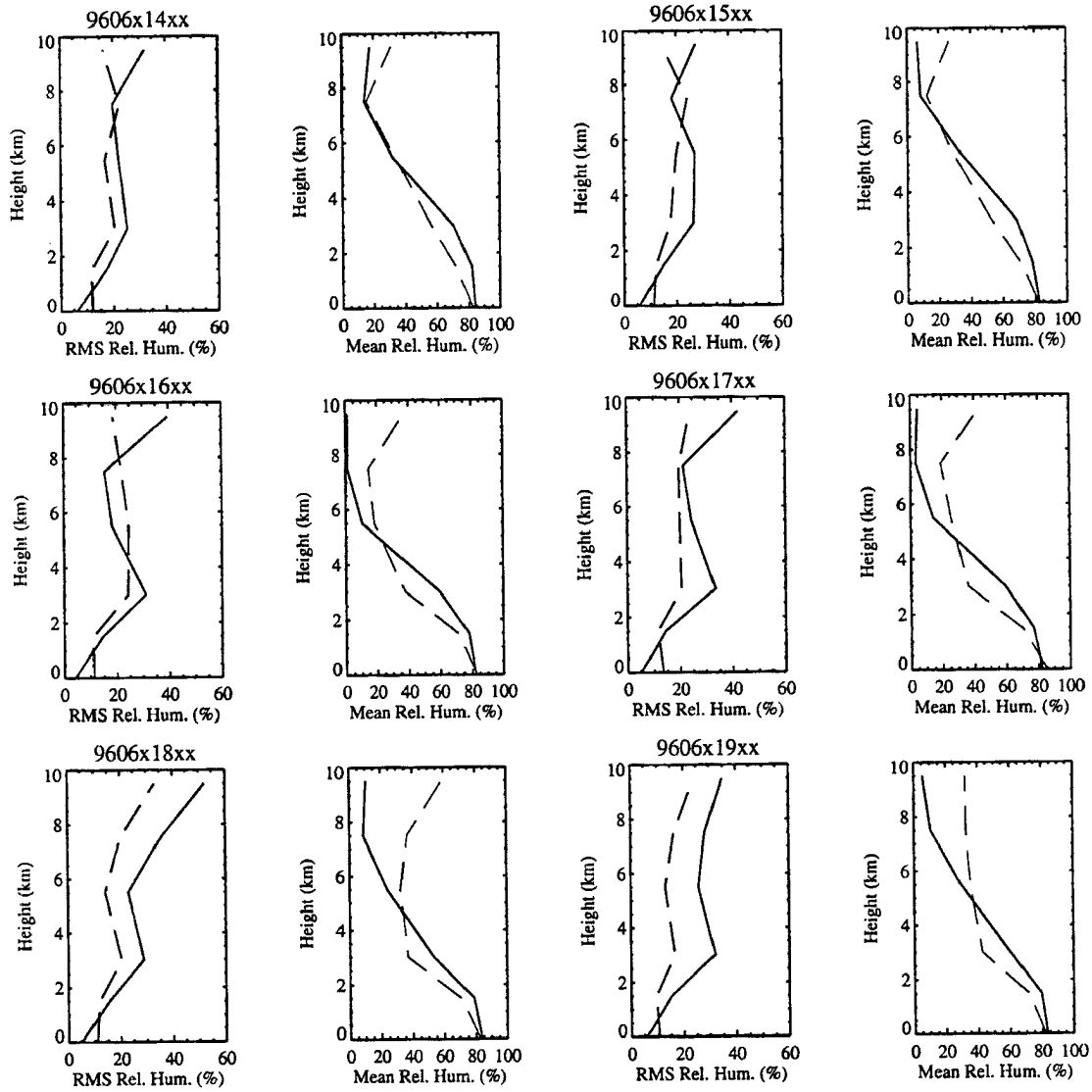

Figure 4.11. Relative humidity RMS and mean profiles for NCEP (dash) and BWRT2 (solid) for six SSM/T-2 morning overflights within the tropical eastern Pacific region during the first week in March 1996.

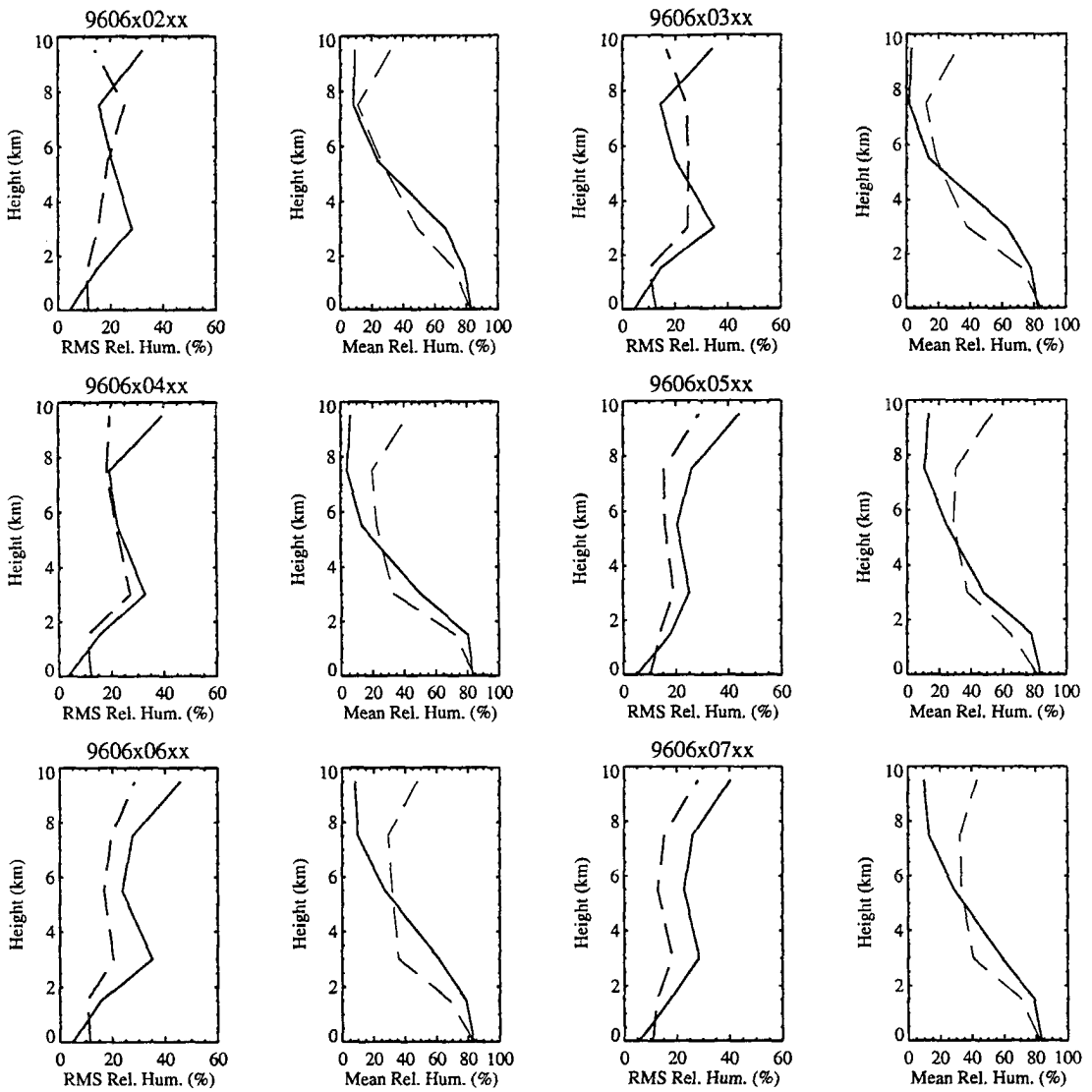

Figure 4.12 . Same as Figure 4.11 except for six SSM/T-2 evening overflights.

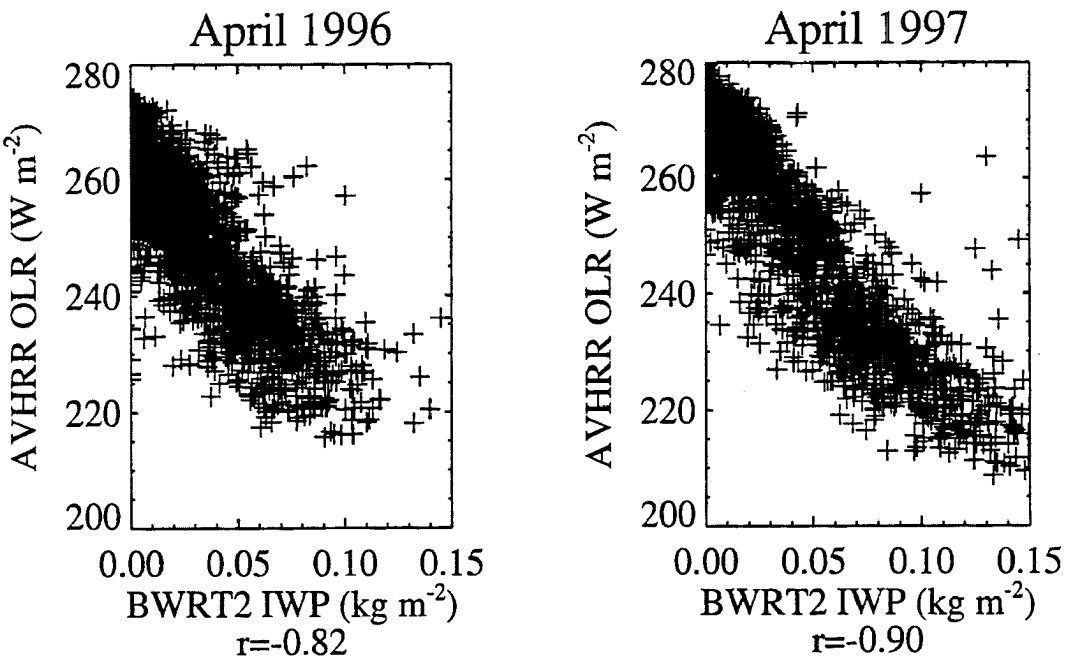

Figure 4.13. Scatter plot of the monthly mean AVHRR OLR as a function of BWRT2 IWP for April 1996 and 1997.

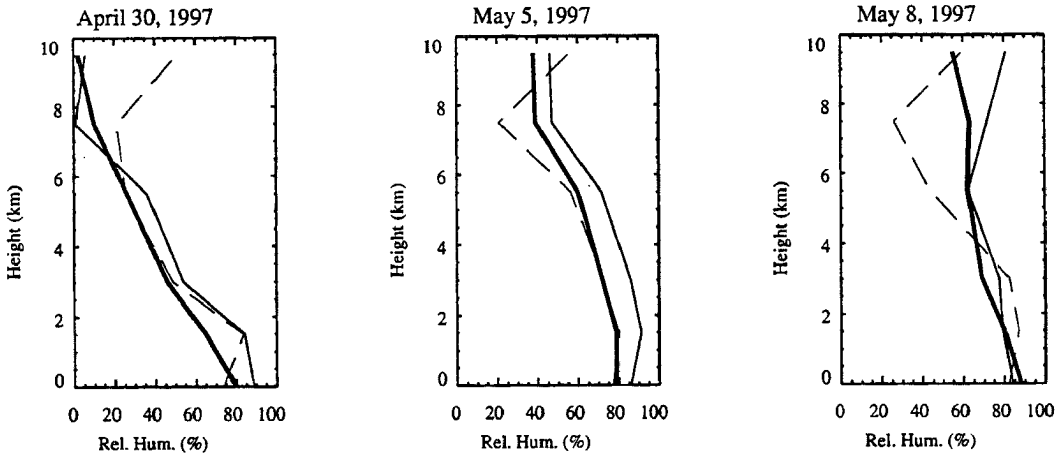

Figure 4.14. Comparison of the Cocos Island radiosonde relative humidity measurements (heavy solid) and nearby BWRT2 retrievals (thin solid). Also plotted is the nearby NCEP profile (dashed).

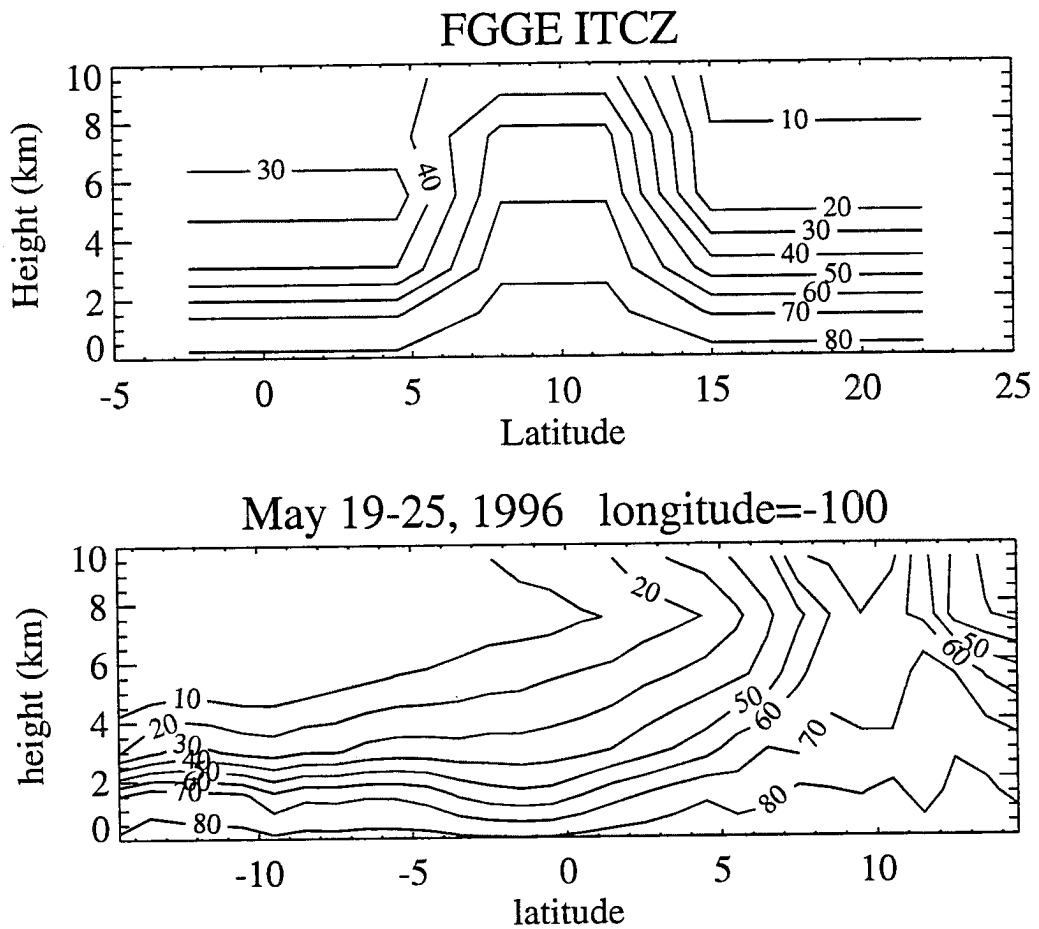

Figure 4.15. Comparison of FGGE ITCZ and BWRT2 mean relative humidity profiles.

5 Observational Analysis of the Eastern Pacific ITCZ

The inter-annual and intra-seasonal variability of atmospheric convection are evaluated using a variety of data. The inter-annual variability of convection and the ITCZ structure is inferred from outgoing long wave radiation and total precipitable water monthly means. The BWRT2 data set is used to infer the intra-seasonal aspects of convection and ITCZ structure in the eastern Pacific during boreal spring.

5.1 Inter-annual variability

The inter-annual variability of the air-sea system in the eastern tropical Pacific has been documented (Deser and Wallace, 1990; Mitchell and Wallace, 1992; Waliser and Gautier, 1993). A long record of OLR and SST derived from satellite observations is available to the climate community and has been used by many workers. Recently, a newer data set has become available for inter-annual climate studies, total precipitable water vapor (TPW) measurements retrieved from SSM/I observations (Randel *et al.*, 1996). The OLR product is an index of cloud top/surface temperature and the TPW product indicates how much water vapor is in the tropospheric column. As documented previously, OLR and TPW tend to be functions of SST over a finite range (Lau *et al.*, 1997; Stephens and Greenwald, 1991).

The purpose of this section is two-fold: the first is to define the double ITCZ structure as it appears in these variables (OLR and TPW), and the second is to illustrate the inter-annual variability of atmospheric moisture and sea surface temperature in the

tropical eastern Pacific. The presence of a double ITCZ is characterized by the following conditions in the 90° W to 150° W (Niño 3 region) zonal average: The OLR is less than or equal to 260 W m^{-2} off the equator, with at least a 15 W m^{-2} increase on the equator, while the TPW off the equator is greater than or equal to 46 kg m^{-2} with a decrease on the equator of at least 4 kg m^{-2}. When these conditions are satisfied, the SST is greater than or equal to 27.5 °C off the equator with at least a 1.5 °C depression on the equator. These SST conditions are only satisfied during the eastern tropical Pacific warm season. A double ITCZ structure, fairly symmetric about the equator is observed in the OLR and TPW fields when these conditions are met. No double ITCZ is observed when the equatorial cold tongue in the SST field is absent. As illustrated in Figure 5.1, Figure 5.2, Figure 5.3, a double ITCZ structure appeared during the warm season in the years: 1984, 1985, 1986, 1988, 1989, 1994, and 1996. 'No-double ITCZ years' tend to coincide with El Niño years, whereas, 'good ITCZ years' are coincident with La Niña years. The absence or presence of a double ITCZ appears to be determined by the El Niño (warm equatorial SST) or La Niña (cold equatorial SST) event cycle. The two best examples are the 1982-1983 warm event which had no double ITCZ (convection present on and off the equator) during the warm season, and the 1988-1989 cold event during which a well defined double ITCZ formed in April 1989.

Inter-annual variability in the meridional component of the surface wind as measured by the TAO buoy array is shown in Figure 5.4. Minima in the monthly mean meridional wind south of the equator are coincident with maxima in TPW, minima in OLR, and maxima in SST south of the equator. Unfortunately 110° W is the only longitude where a long record of winds is available. The minima in meridional wind south of the equator (at about 2° S) is only present when the double ITCZ is present during the warm season of La Niña type years. The stronger northerlies separated by weaker northerlies, at the end of March during these years, sets up a low level mass divergence pattern

(convergence at 4° N, divergence at 0° N, convergence at 4° S) consistent with that necessary for the double ITCZ presence.

It is apparent that the double ITCZ structure is controlled by the SST field—an appropriate SST field (warm off the equator, cold on the equator) is a necessary but not sufficient condition for double ITCZ formation in the central and eastern tropical Pacific. The relationship between convection and sea surface temperature will be explored in greater detail in chapter 6.

5.2 Intra-seasonal variability

A description of the temporal and spatial structure of the ITCZ using the BWRT2 data set is presented. The variables used for this description are the cloud liquid and ice water contents and the vertical structure of the humidity field. As part of the description, the latitude at which convection is frequently occurring is documented. This can be inferred from latitude-longitude plots of cloud liquid and ice water, as well as from height-latitude cross sections of the humidity field. Additionally, it is necessary to describe the depth of convection, the time evolution of the ITCZ from single to double and back again, as well as the degree of symmetry of the ITCZ about the equator. The strength and symmetry of the double ITCZ and its relationship to sea surface temperature and low-level mass flow will also be discussed.

Using daily means of TPW and CLW derived from SSM/I observations, it was determined that the time period when the double ITCZ is at its peak, in terms of zonal extent and equatorial symmetry, is during the first two weeks following the boreal vernal equinox. This post equinoctial period is encompassed by a longer period which is referred to as the warm season— the SST south of the equator is relatively higher (> 27 °C) than during the rest of the year. This is usually the time when the equatorial SST cold tongue is at its weakest. The strength of the cold tongue is dependent on the El

Niño cycle. Fortunately, three different types of warm season SST fields occurred during the BWRT2 data set time period. As depicted in Figure 5.9, the SST field during the 1995 warm season was fairly average, the 1996 SST field had a stronger cold tongue than average, and the 1997 SST field was much warmer than average on the equator. During non-El Niño warm seasons, when the equatorial sea surface temperature is cold in the eastern Pacific, atmospheric convection forms in quasi-symmetric bands about the equator, extending over most of the central and eastern tropical Pacific. This convection is well represented by bands of cloudiness which tend to form at about 6° N and 6° S and have a latitudinal width of about 4°. The latitudinal and longitudinal extent of these cloud bands is dependent on the type of cloud water: liquid water fields are observed, in the BWRT2 data, to be greater in the extent of coverage than ice water fields. These features are depicted in Figure 5.5 and Figure 5.6. Note that regions where liquid and ice clouds are present together indicates frequent deep convection (e.g. 1995; 8° N, 150° W). Locations where liquid water is present with no ice water indicate regions of marine stratus or shallow convection (e.g. 1995; 4° S, 110° W). Since stratus are typically observed over colder waters and the SST at this location is greater than 27 °C, it is believed that the subsidence from both the south Pacific high and from the strong convection present in the northern ITCZ are working together to inhibit strong convection at this location. Regions with ice clouds and no liquid clouds show areas where upper level advection is moistening a previously dry atmosphere (e.g. 1995, 1996; 6° S, 82° W). During El Niño years, when the equatorial cold tongue is very weak or absent, no double ITCZ is observed to form in the cloud water fields. This is evident in the 1997 plots of Figure 5.5 and Figure 5.6, where convection is frequent over warm ocean surfaces at and near the equator between 90° W and 110° W.

As expected, the humidity fields at lower and upper levels are observed to be fairly well correlated with the cloud liquid and ice water fields, respectively. This

correlation tends to break down near the south American coast. No cloud liquid water is present over the cold waters off the coast of Ecuador and Peru, and it is believed that the high moisture content in this region is due to the easterly advection (observed in NCEP reanalysis) of moisture from convective cells (observed in SSM/T-2 radiances) over the continent. The features described above, for the years 1995, 1996, and 1997, are depicted in Figure 5.7 and Figure 5.8.

The vertical structure of the relative humidity field in the ITCZ region as a function of latitude provides some knowledge about the mean latitude and depth of convection. Elevated humidity values are indicative of convective activity, whereas suppressed humidity values are indicative of subsidence. As seen previously in Figure 5.5 through Figure 5.8, with the vertical structure depicted in Figure 5.10, the mean latitude and strength of the post equinoctial ITCZ changes from year to year. Although the double ITCZ is represented by the cloud liquid water plot as fairly symmetric in latitudinal position and strength in 1995, the ice cloud water plot (Figure 5.6) and the height-latitude cross section of relative humidity (Figure 5.10) show that the northern branch of the ITCZ is much stronger and is displaced farther from the equator than the southern branch of the ITCZ. Notice that the 80% relative humidity contour in Figure 5.10 is elevated a 5° N and 5° S in 1995, showing low level buoyancy, but the rest of the contours south of the equator are generally suppressed, indicating strong upper level subsidence and therefore convective capping. This asymmetry in the convective strength of the double ITCZ during 1995 is coincident with a meridional asymmetry in the warmth of the SST field (28 °C in the north, 27 °C in the south). On the other hand, the 1996 double ITCZ is fairly symmetric about the equator, 5° N and 4° S, and the strength of convection, as measured by the relative humidity surfaces, is nearly symmetric about the equator with a well defined local minimum in the humidity field located at the equator near the surface, but at about 1° N at mid and upper levels. The height-latitude relative

humidity cross section in 1997 shows no double ITCZ—a single ITCZ appears to be located near the equator with suppressed humidity values present south of the equator. The high humidity at approximately 12° N, 110° W, in the upper levels is coincident with the presence of ice cloud water and the absence of liquid cloud water. It would appear that the ice clouds and coincident upper level moisture are being transported from the region of strong convection just to the west (strong upper level westerlies are present in the NCEP reanalysis, not shown). This kind of inference about the vertical structure of the moisture and cloud field could not be accurately accomplished using other data sets such as TPW, OLR , or HRC. The details in the BWRT2 data allow for a more comprehensive study of the tropical moisture profile structure.

The time evolution of the zonally averaged ITCZ is well illustrated in latitude-time plots of cloud water and humidity. Figure 5.11 through Figure 5.15 show the zonally averaged (Niño 3 region: 90° to 150° W) cloud liquid water, cloud ice water, relative humidity at 3.0 km and 7.5 km, and the SST fields as a function of latitude and time for the March-April-May time period during 1995, 1996, and 1997. Since the Reynolds SST represents the mean SST over a seven day period, the BWRT2 daily means have been averaged over each SST defined week for useful comparison. As seen in Figure 5.11, the cloud liquid water depicts a fairly symmetric (defined here as, LWC within 0.03 g m^{-3} on both sides of the equator with LWC equal to zero on the equator) double ITCZ from week 2 to week 4 in 1995 and from week 2 to week 7 in 1996. No double ITCZ is present in 1997. The deep convection, as determined by cloud ice water contents (Figure 5.12), depicts a double ITCZ for week 1 to week 5 in 1996 (using IWC within 0.02 g m^{-3} on both sides of the equator with zero IWC on the equator). No double ITCZ is present in 1995 or 1997 using this standard. Similar inferences about the presence or absence of the double ITCZ as a function of time are difficult using the relative humidity fields in Figure 5.13 and Figure 5.14. Using the above stated times for

the presence of the double ITCZ, it is apparent from the SST latitude-time plot that a symmetric (in strength) ITCZ occurs when the SST on either side of the equator is within 0.5 °C and there is a minimum on the equator that is less than or equal to 26.5 °C. Of course these general statements are made with the understanding that these latitude-time plots are zonally averaged over a large distance (60° longitude) and therefore represent a climatological-large scale perspective. The presence of the double ITCZ is also depicted in the meridional wind field. A latitude-time plot of the TAO buoy meridional surface wind (Figure 5.16) shows that northerly winds are observed south of the equator during the time when the double ITCZ is present.

5.3 Summary

The spatial and temporal evolution of the ITCZ during the warm season has been documented. It was shown that a double ITCZ (e.g., convection present on either side of the equator with no convection on the equator) occurs most often during the warm season of non-El Niño years, when the SST south of the equator exceeds 27.5 °C while the SST on the equator remains below 26.5 °C. The latitudinal symmetry of the ITCZ about the equator appears to be related to the symmetry of the SST field. SST-convection relationships observed using the BWRT2 and Reynolds SST data are discussed in section 6.1.

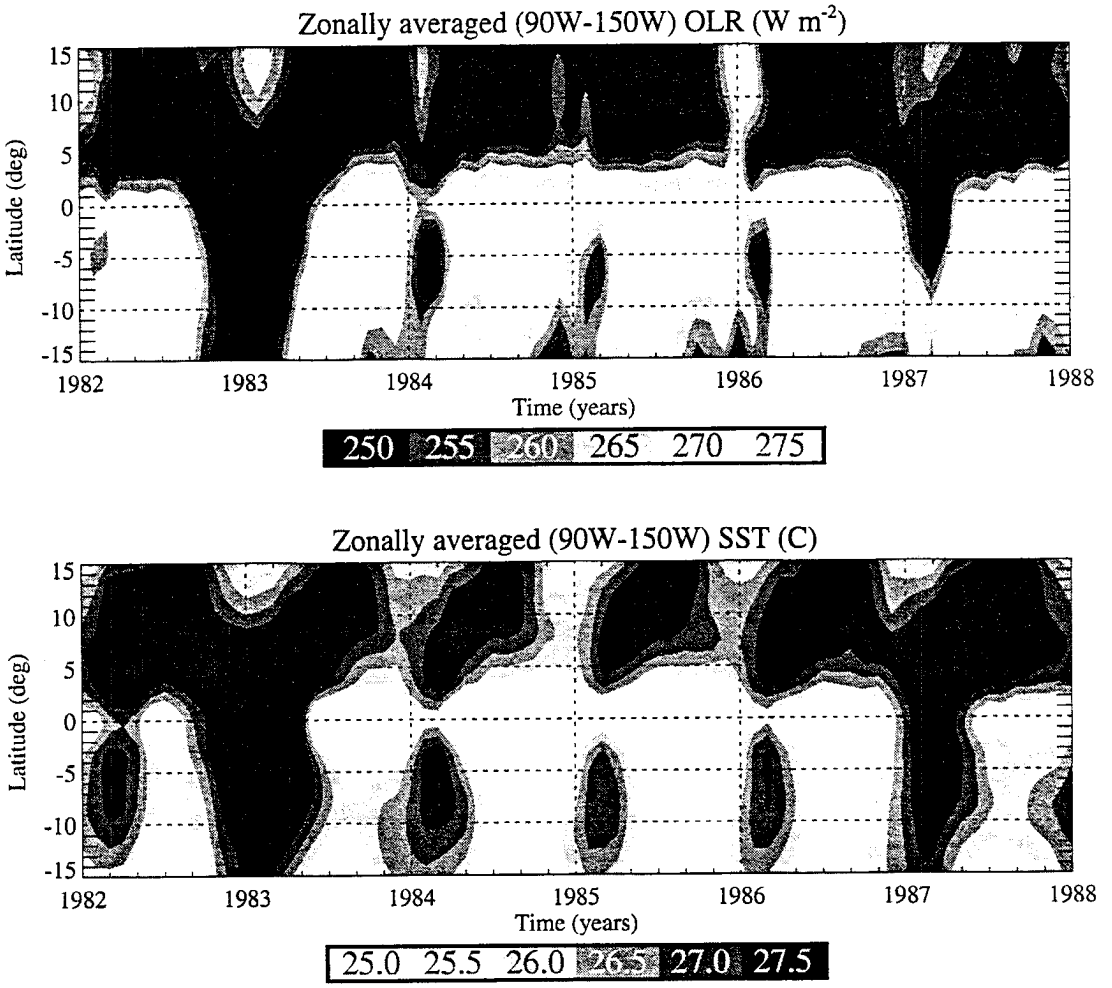

Figure 5.1. Latitude-Time plot of AVHRR OLR and Reynolds SST for 1982-1987.

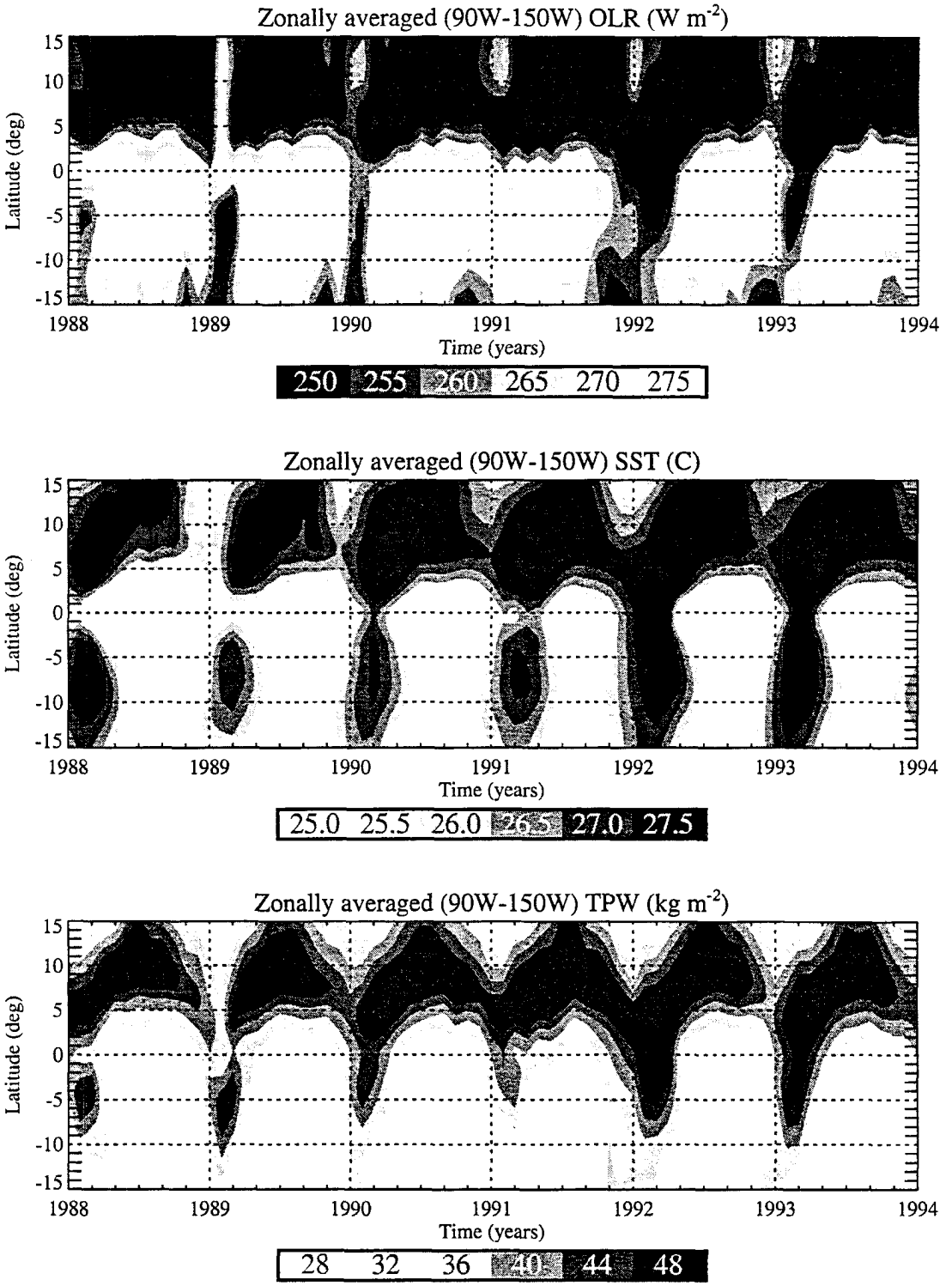

Figure 5.2. Latitude-Time plot of AVHRR OLR, Reynolds SST, and SSM/I TPW for 1988-1993.

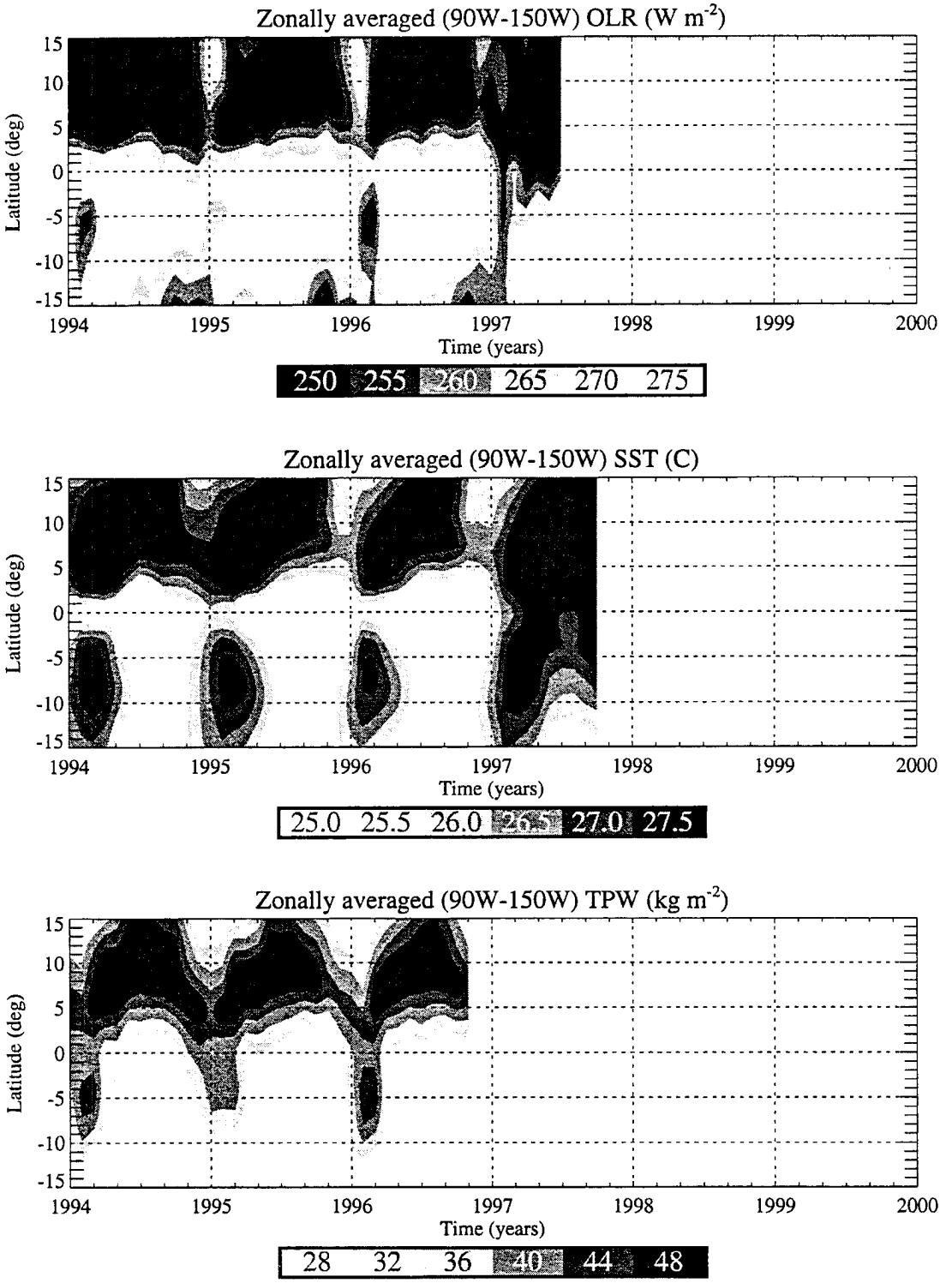

Figure 5.3. Latitude-Time plot of AVHRR OLR, Reynolds SST, and SSM/I TPW for 1994-1996.

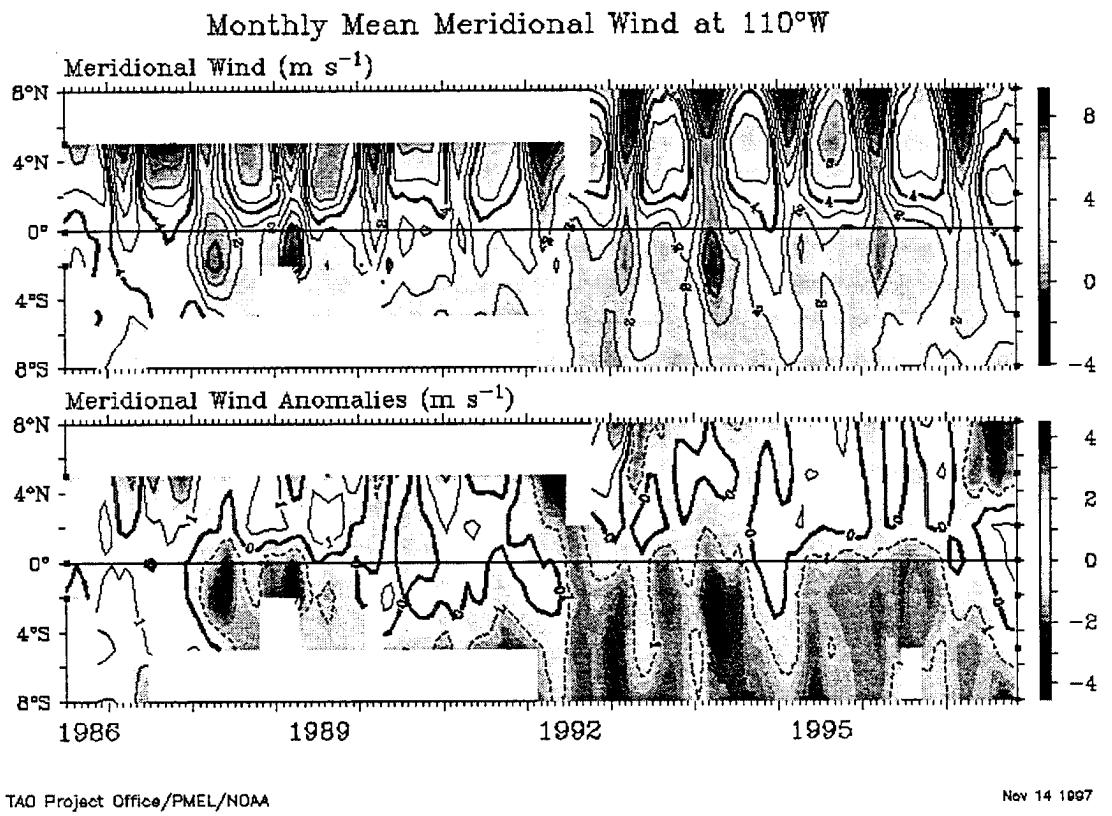

Figure 5.4. Latitude-Time plot of TAO monthly mean meridional wind for 1986-1997. Solid contours represent positive values (southerlies) while dashed contours represent negative values (northerlies).

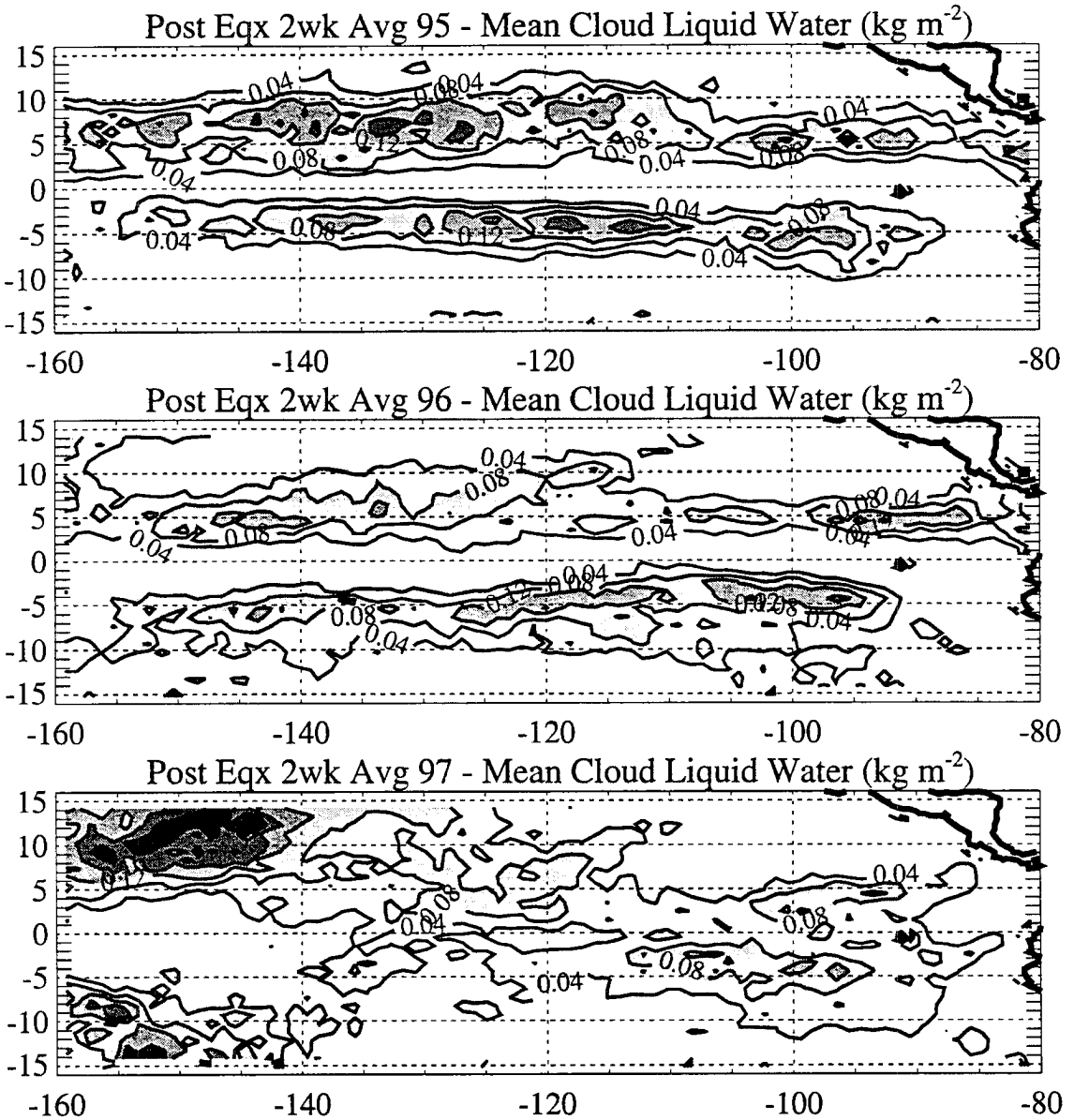

Figure 5.5. Latitude-Longitude plots of the post equinox 2 week mean BWRT2 cloud liquid water for 1995, 1996, 1997.

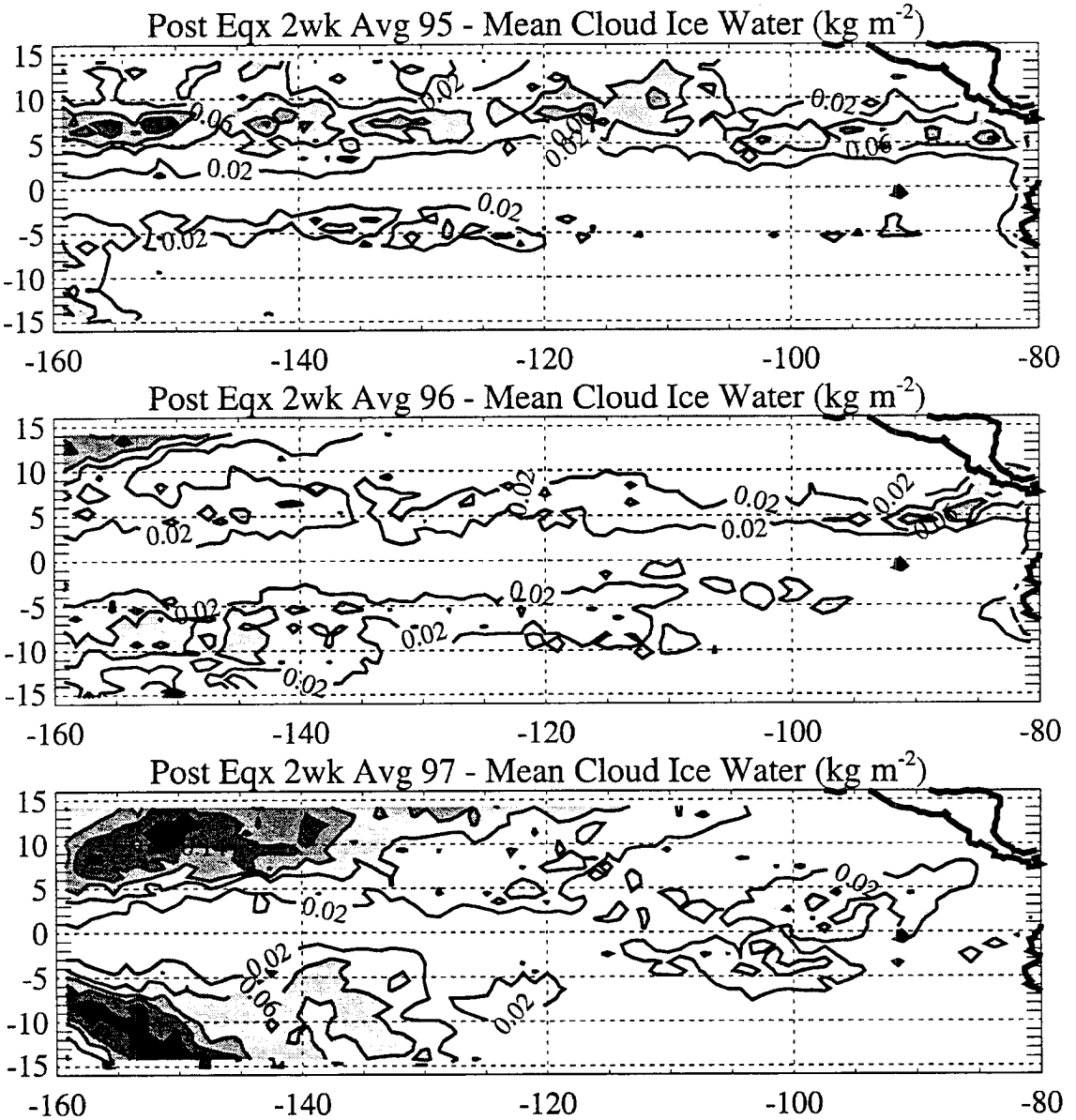

Figure 5.6. Latitude-Longitude plots of the post equinox 2 week mean BWRT2 cloud ice water for 1995, 1996, 1997.

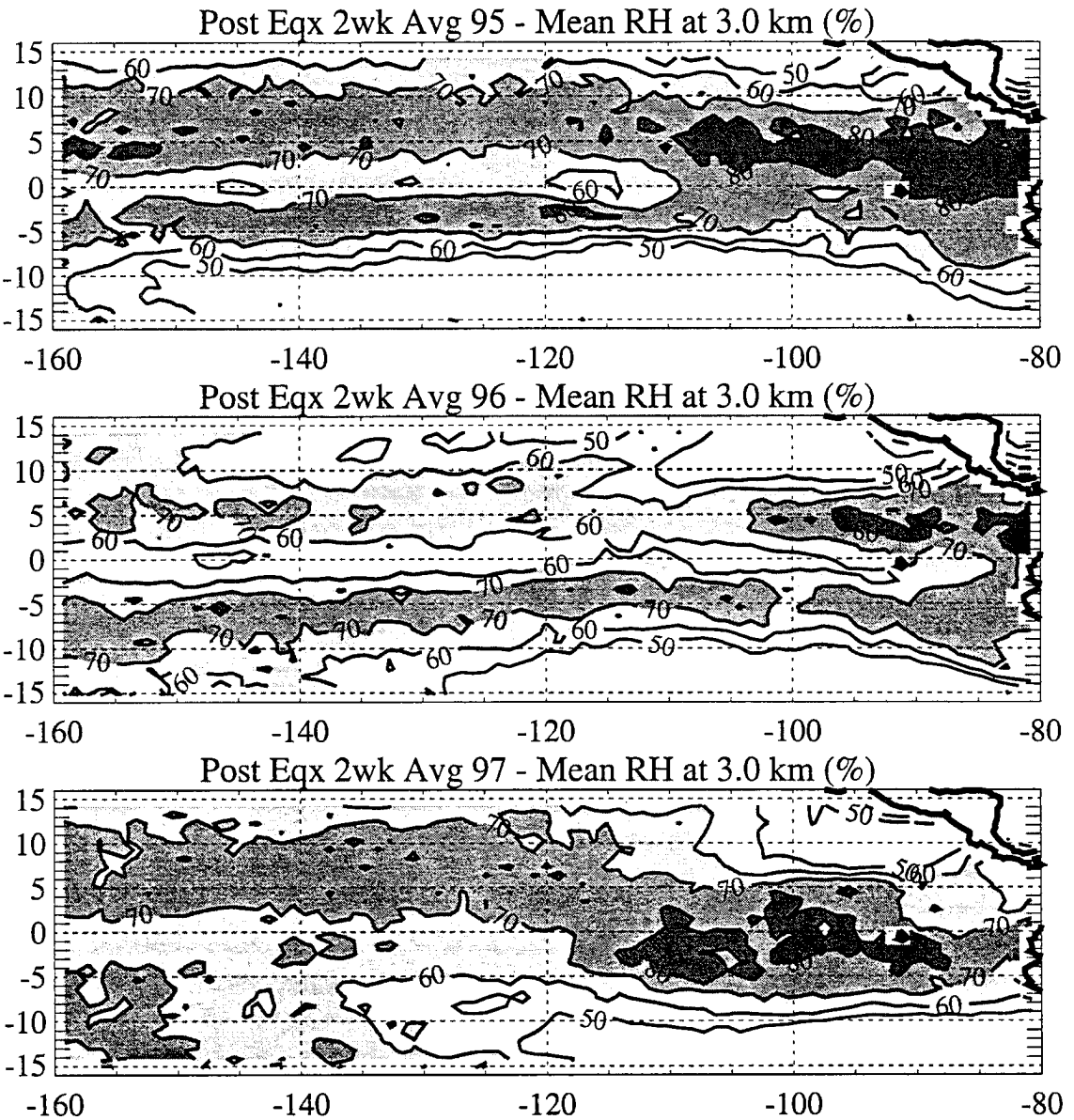

Figure 5.7. Latitude-Longitude plots of the post equinox 2 week mean BWRT2 relative humidity at 3.0 km (700 mb) for 1995, 1996, 1997.

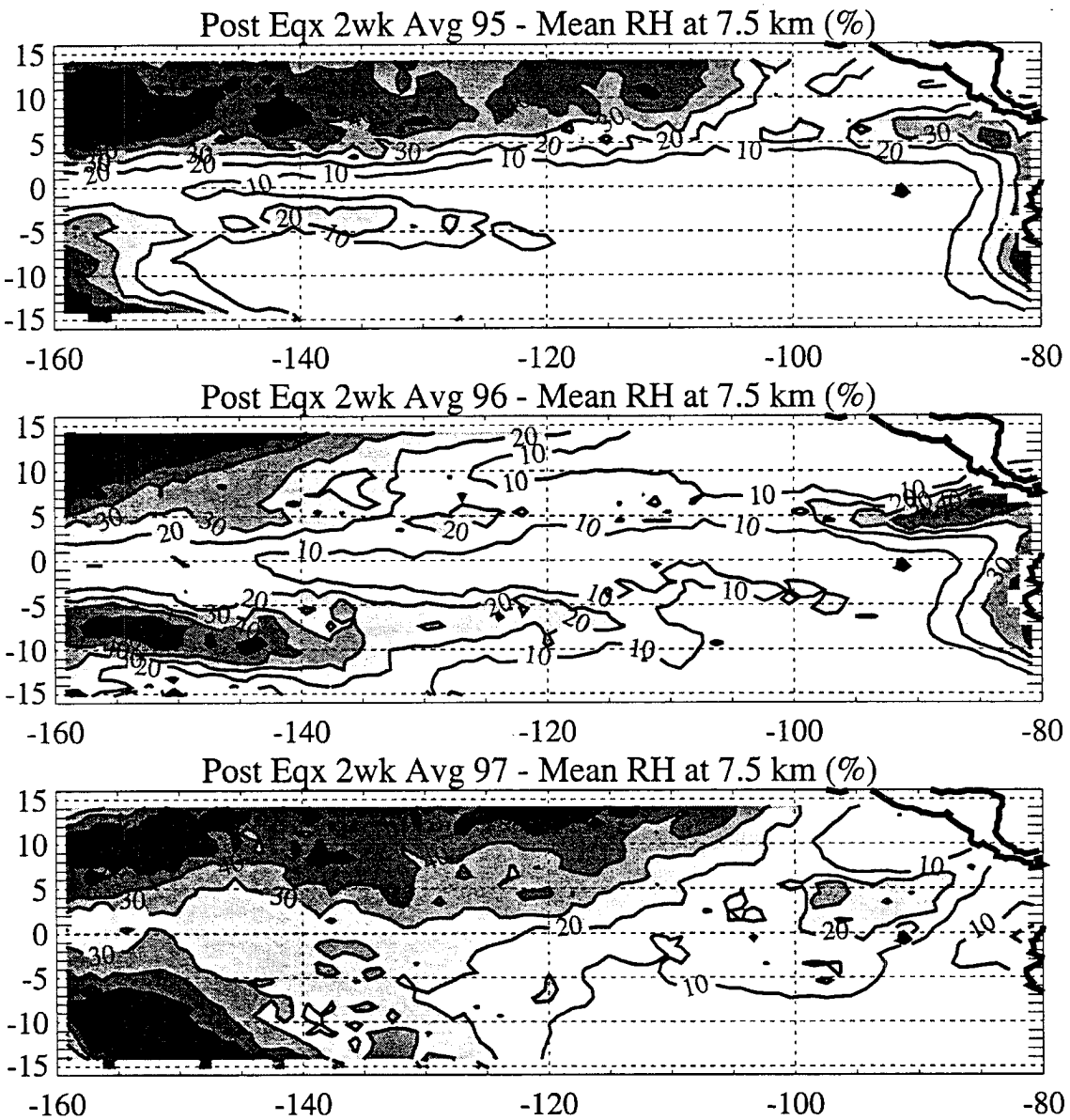

Figure 5.8. Latitude-Longitude plots of the post equinox 2 week mean BWRT2 relative humidity at 7.5 km (400 mb) for 1995, 1996, 1997.

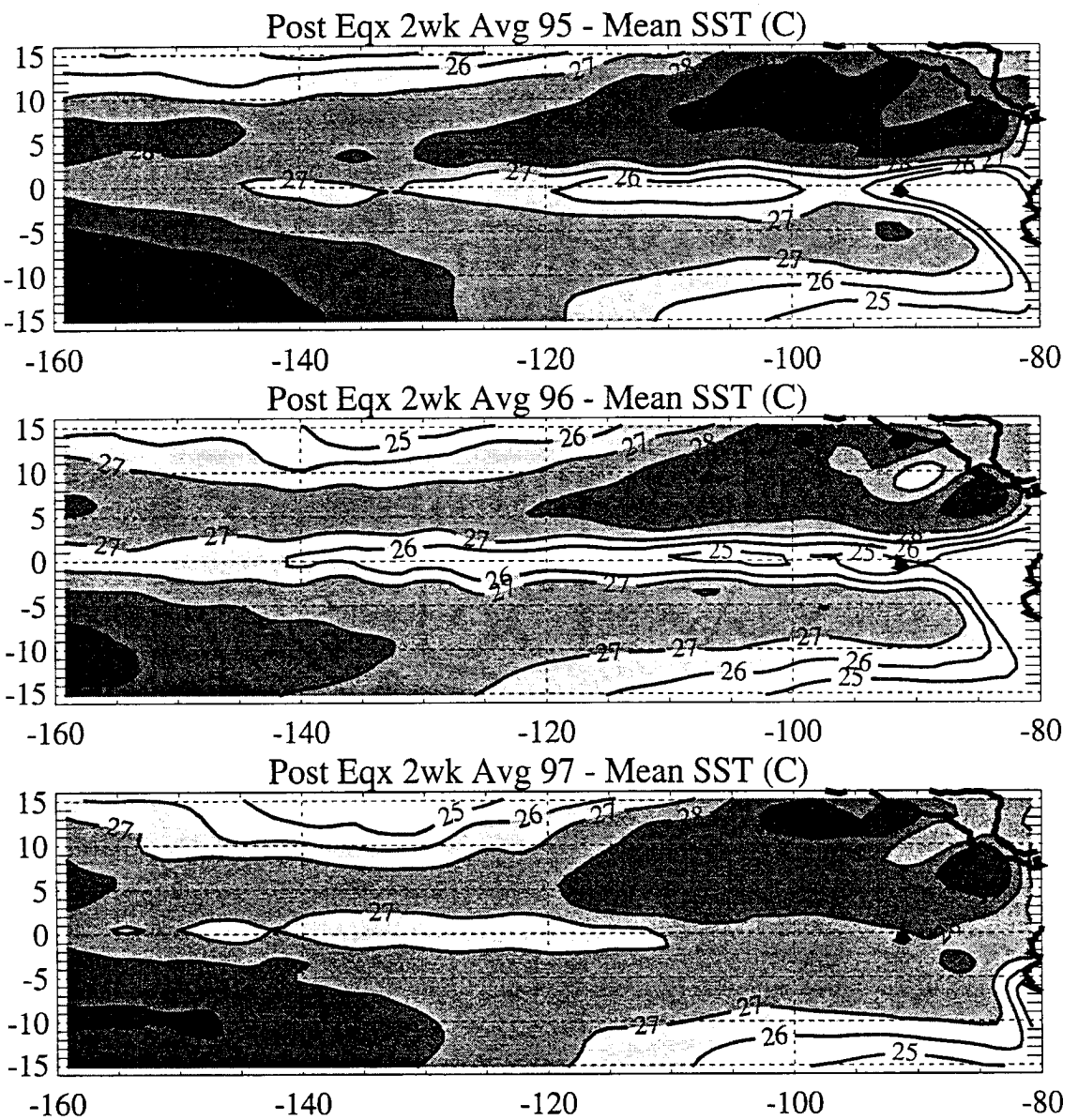

Figure 5.9. Latitude-Longitude plots of the post equinox 2 week mean Reynolds SST for 1995, 1996, 1997.

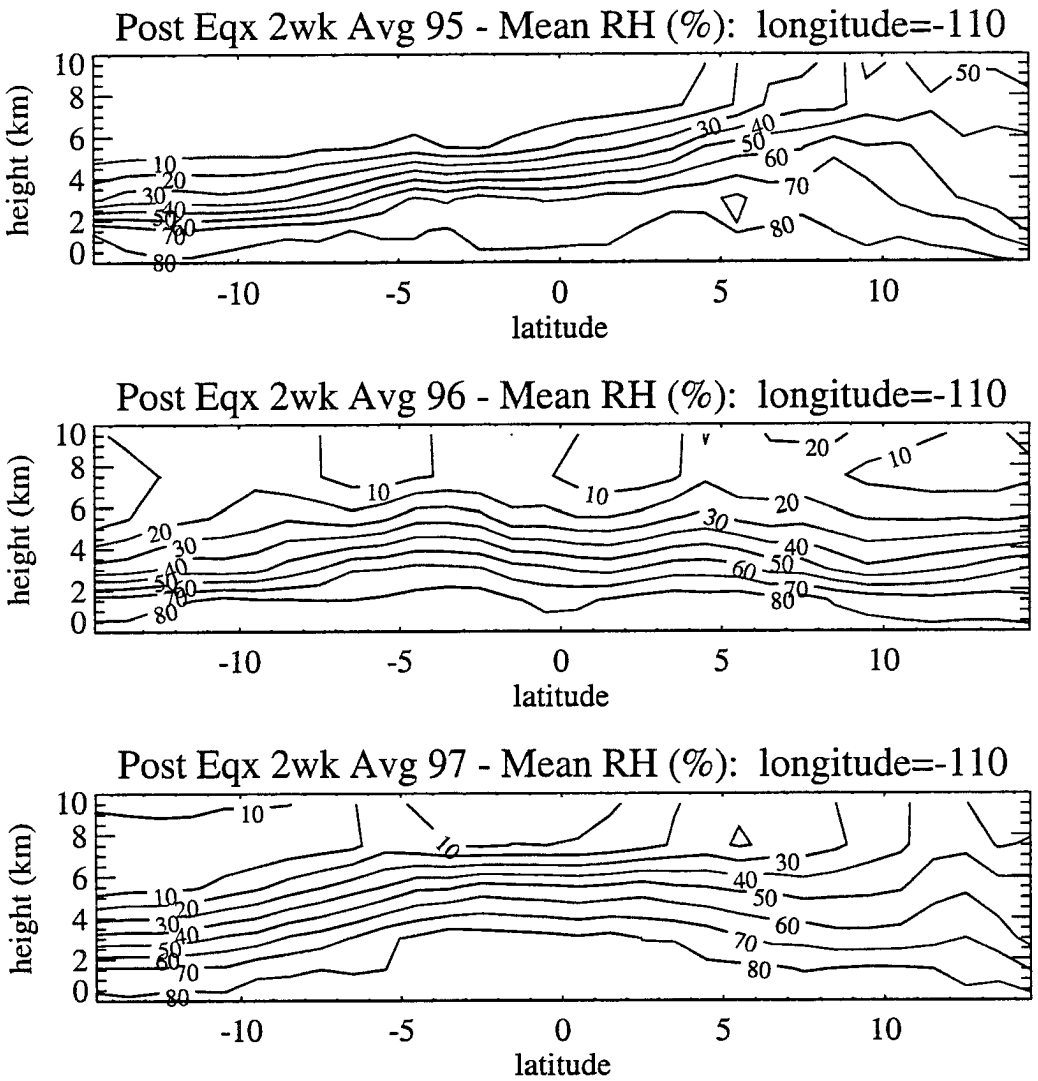

Figure 5.10. Height-Latitude plots of the post equinox 2 week mean BWRT2 relative humidity at 110° W for 1995, 1996, 1997.

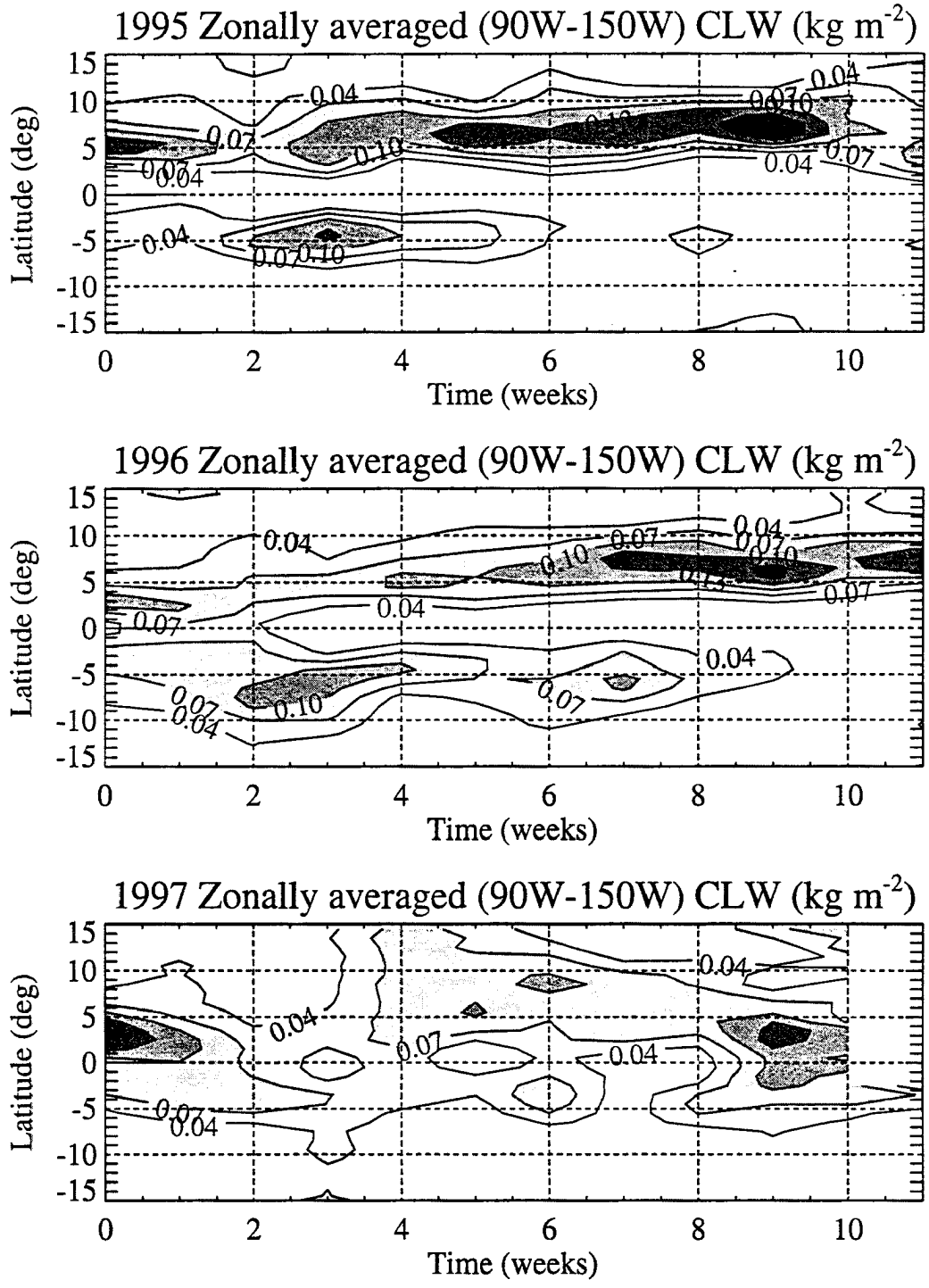

Figure 5.11. Latitude-Time plots of the zonally averaged (90° W - 150° W) weekly mean BWRT2 cloud liquid water for 1995, 1996, 1997.

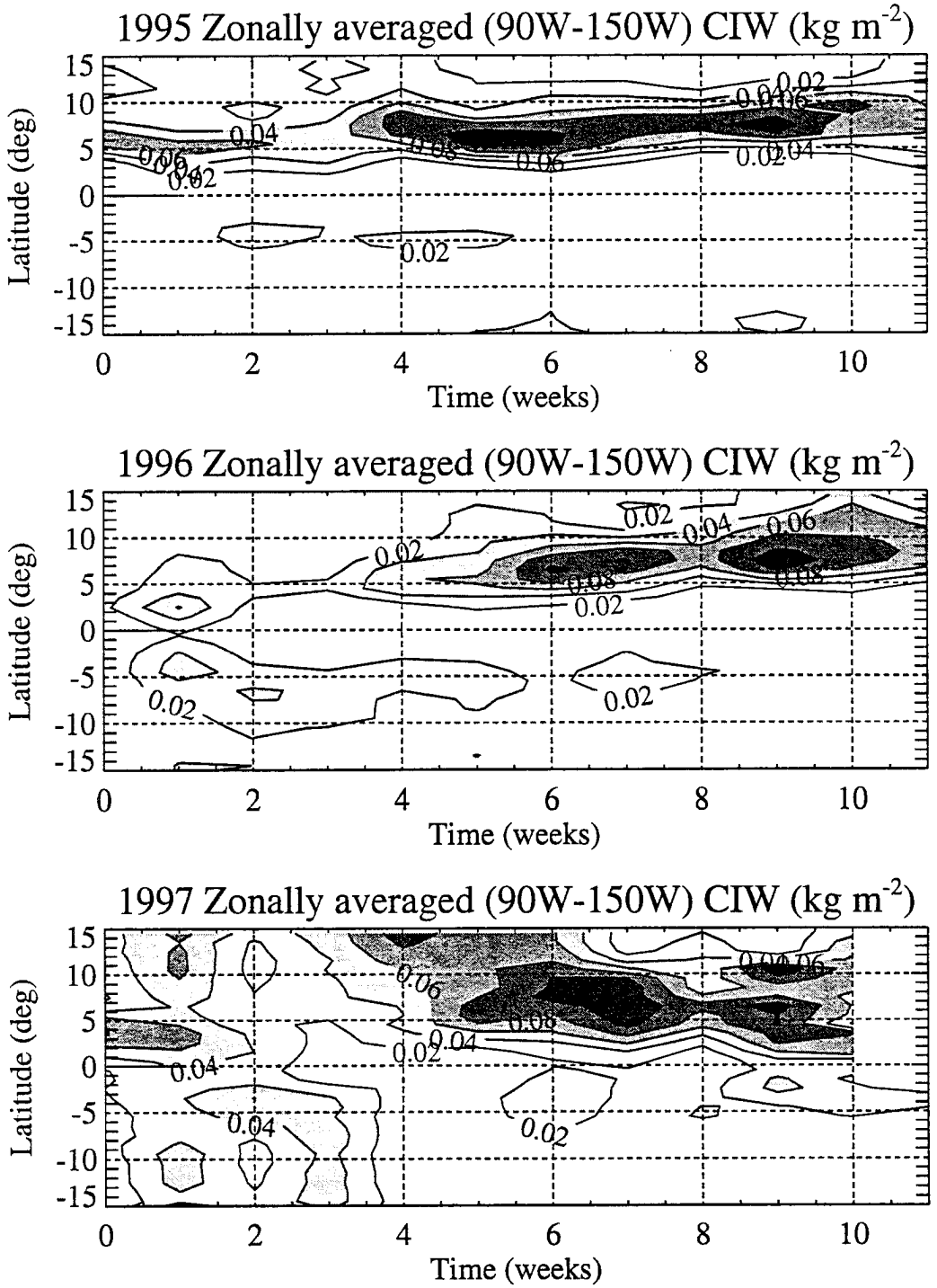

Figure 5.12. Latitude-Time plots of the zonally averaged (90° W - 150° W) weekly mean BWRT2 cloud ice water for 1995, 1996, 1997.

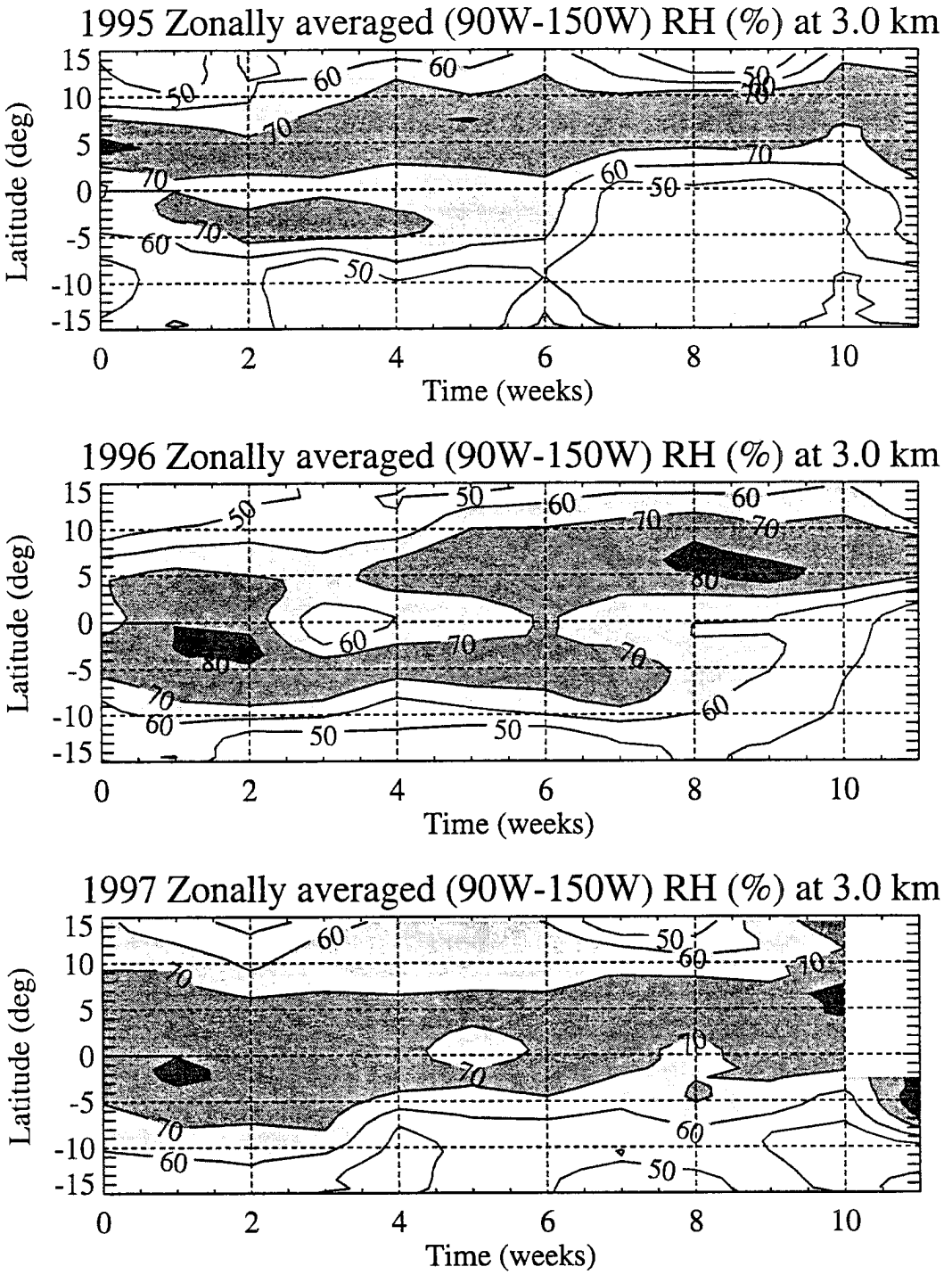

Figure 5.13. Latitude-Time plots of the zonally averaged (90° W - 150° W) weekly mean BWRT2 relative humidity at 3.0 km (700 mb) for 1995, 1996, 1997.

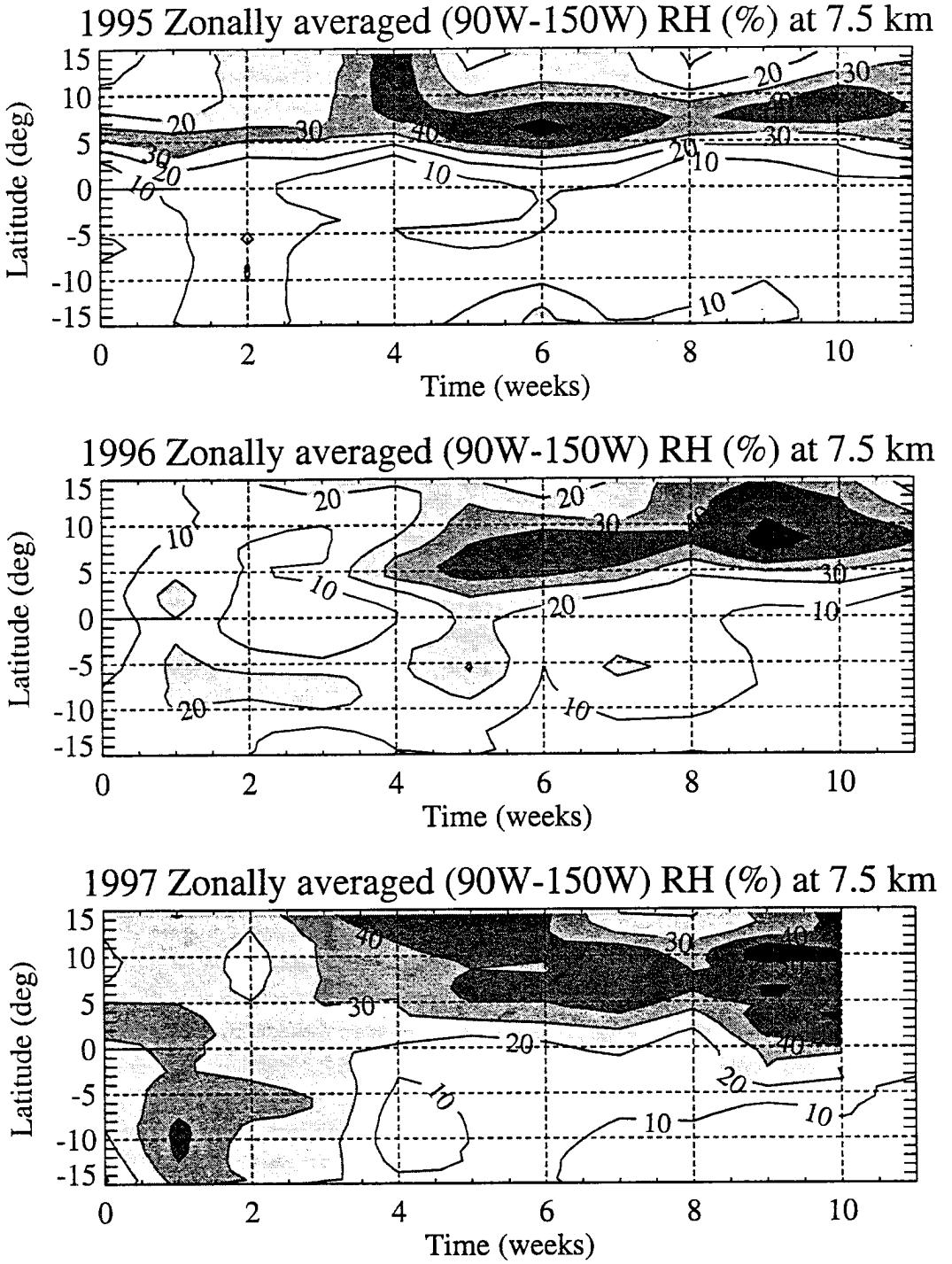

Figure 5.14. Latitude-Time plots of the zonally averaged (90° W - 150° W) weekly mean BWRT2 relative humidity at 7.5 km (400 mb) for 1995, 1996, 1997.

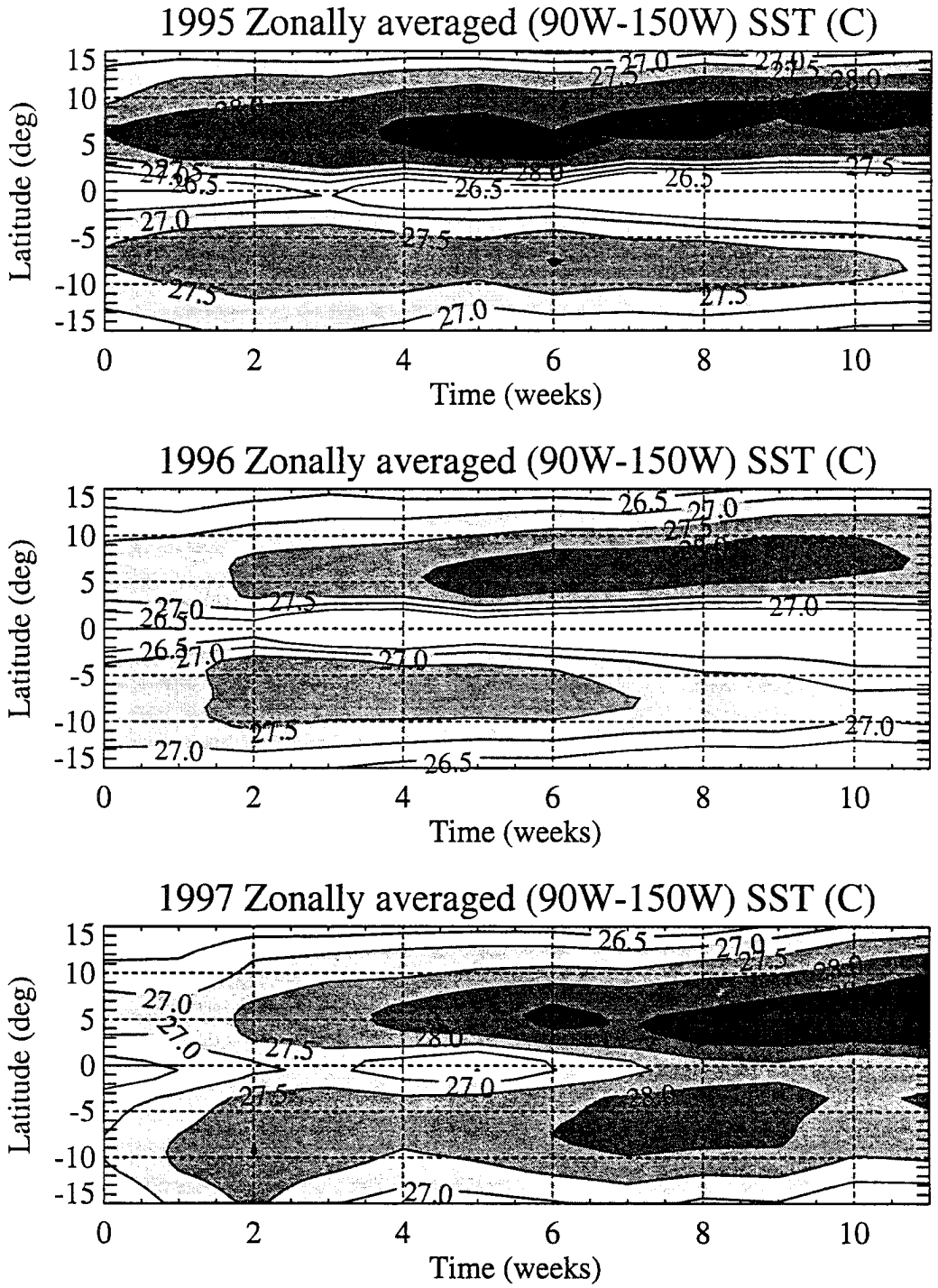

Figure 5.15. Latitude-Time plots of the zonally averaged (90° W - 150° W) weekly mean Reynolds SST for 1995, 1996, 1997.

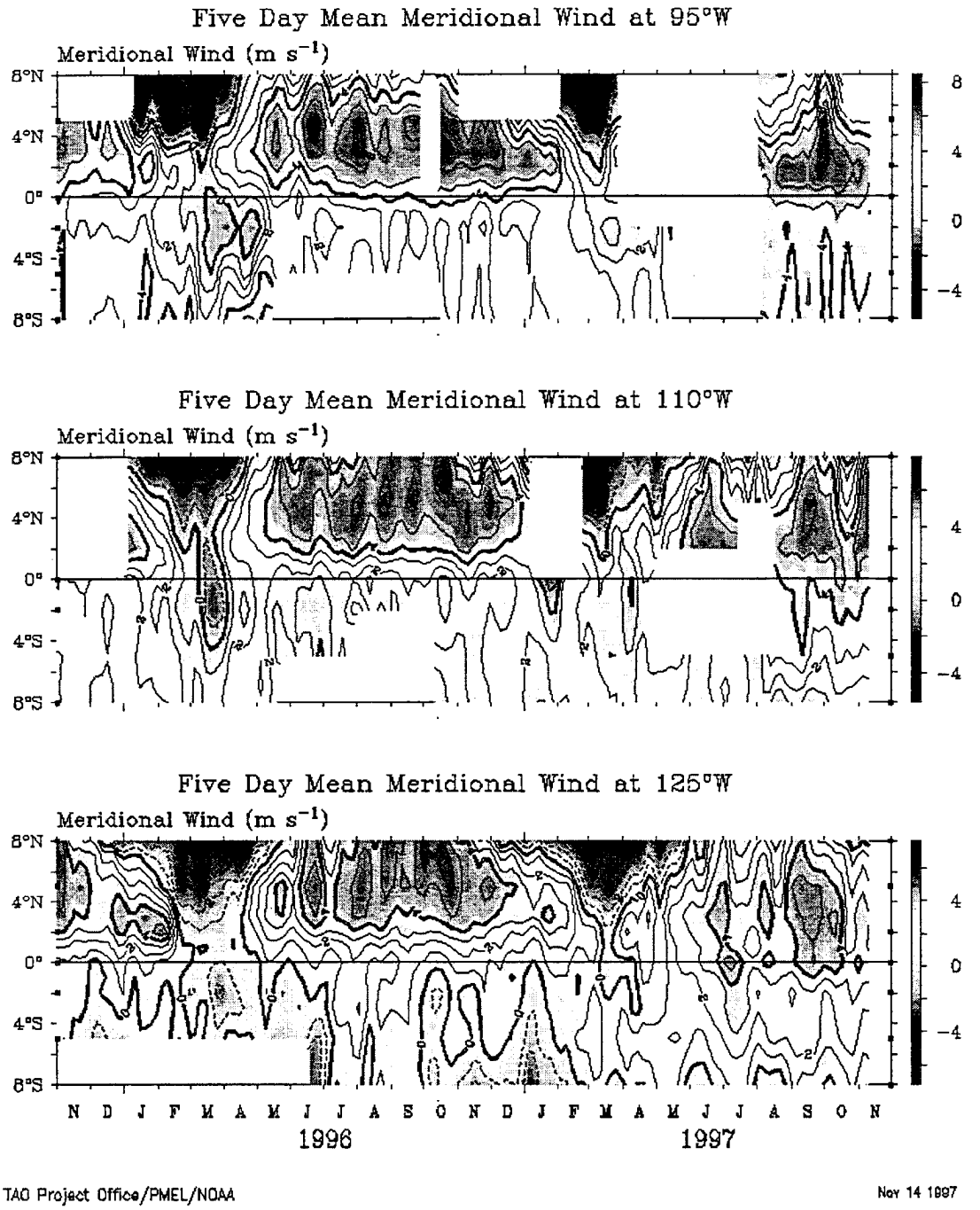

Figure 5.16. Latitude-Time plots of the TAO five day mean meridional wind at 95° W, 110° W, 125° W.

6 Structural Determination of the Eastern Pacific ITCZ

Two of the primary factors in determining the frequency of atmospheric convection and hence the structure of the ITCZ are sea surface temperature and surface wind divergence. The dependency of convection, as determined by BWRT2 cloud liquid and ice water frequency, on SST and the importance of the surface wind field are discussed. Previous observational and theoretical studies related to the structural determination of the ITCZ are presented and when appropriate, the observations made from the present work are given for comparison. Finally, a hypothesis is put forth describing how and under what conditions a double ITCZ forms in the eastern Pacific. The implications of this description on numerical modeling of the tropical atmosphere are also given.

6.1 Observed convection dependencies on SST and surface wind field

Much work has been done studying the effects of sea surface temperature and surface wind divergence on atmospheric convection in the tropics (e.g. Lindzen, 1987; Gutzler and Wood, 1990; Mitchell and Wallace, 1992; Fu *et al.*, 1994; Lau *et al.*, 1997). Many studies are heavily spatially or temporally averaged, and most regional studies are confined to the tropical Pacific warm pool. The tropical eastern Pacific has received little attention, usually only being included as part of a global climate study. The short lived warm season in the eastern Pacific, occurring at the boreal vernal equinox, represents a time of considerable variance for the ocean-atmosphere system. It is during this time when the tropical SST south of the equator warms sufficiently to promote and sustain

atmospheric convection in the south eastern Pacific. Results presented in chapter 5 showed a qualitative relationship between SST and observed atmospheric convection where OLR, TPW, and cloud liquid and ice water were used as indices of convection. Of particular note was the lack of convection on the equator when the SST cold tongue was noticeably present.

A more direct measure of the dependence of cloud water on SST is shown in the scatter plots of Figure 6.1. Unfortunately, neither cloud liquid water content, nor cloud ice water content exhibit a distinct relationship as a function of SST. The cloud water-SST dependence is further explored in plots of the frequency of cloud water as a function of SST. Figure 6.2 shows normalized histograms of cloud liquid and cloud ice water versus SST for a cloud water threshold set at 0.02 g m^{-3} (mean minus one standard deviation). Figure 6.2a and Figure 6.2b depict the cloud water-SST relationship for the entire BWRT2 region, whereas Figure 6.2c and Figure 6.2d depict the cloud water-SST relationship for the BWRT2 region west of 100° W, thereby eliminating land effects. It is clear that the continental convection can lead to spurious conclusions when evaluating the relationship with SST. As seen in Figure 6.2c and Figure 6.2d, the frequency of cloud water as a function of SST is bimodal for both species, liquid and ice. The cloud liquid water has a maximum at 27.5 °C, whereas the cloud ice water has a maximum at 28.5 °C. Figure 6.3 shows similar histograms but with a higher threshold on the cloud water, mean plus one standard deviation, meant to be an index of deeper convection. Shown in Figure 6.3a and Figure 6.3b is the frequency for the central tropical Pacific (west of 100° W, between 16° N and 16° S). Shown in Figure 6.3c and Figure 6.3d is the frequency for the central equatorial Pacific (west of 100° W, between and between 8° N and 8° S). Comparing the cloud liquid water frequency between the two regions, it is obvious that the equatorial region contains more cloud liquid water than does the encompassing tropical region. Using the relationship for OLR as a function of IWC described in section

4.3.3, an ice water content of 0.08 kg m^{-2} (mean plus one standard deviation) is equivalent to an OLR value of about 235 W m^{-2}. A typical mean OLR threshold for deep convection is about 240 W m^{-2} (Lau *et al.*, 1997). Therefore, the 0.08 kg m^{-2} threshold is a conservative estimate of the presence of deep convection. Using IWC > 0.08 kg m^{-2} as the deep convection index, it is seen that the equatorial region contains no deep convection over regions with an SST less than 26.5 °C. The tropical region does have deep convection present over region with an SST less than 26.5 °C. This figure illustrates the fact that deep convection occurs over colder SST, but not over the equatorial cold tongue (also observed qualitatively in chapter 5.2). This observation is important to the understanding of the maintenance of the double ITCZ structure in the eastern Pacific and will be discussed further in section 6.4.

Observations from the TAO buoy array and the NCEP/NCAR reanalysis product are used qualitatively to evaluate the relative importance of the surface mass divergence on convection and therefore the structure of the ITCZ in the eastern Pacific. The RMS of the NCEP - TAO difference for those data in Figure 6.4 is shown in Table 6.1. Although the NCEP/NCAR reanalysis project assimilates buoy data, the RMS difference for the meridional wind is large. Since the TAO buoy data are too sparse to use in divergence calculations, the NCEP wind field is used to calculate the low level mass divergence. Due to the lack of observations outside the TAO buoy array, and the disagreement in the meridional component of the surface wind, this divergence is only meant to be interpreted qualitatively. The majority of the BWRT2 region is convergent during the post equinoctial period (lighter areas in Figure 6.4) with divergent regions being coincident with the influx of the northeast and southeast trade winds with the TAO wind field overlaid in white. The TAO data show convergence off the equator and divergence on the equator in the eastern Pacific during the 1996 post equinoctial mean. The NCEP divergence field has a hint of divergence on the equator at 110° W during the same time

period. Figure 6.4 also shows the mean May surface wind field for 1996 and 1997. The May fields are presented to contrast those of the post equinoctial period shown in Figure 6.4. Note the considerable convergence region in the eastern Pacific at 8° N present in the May mean but not during the post equinoctial period.

6.2 Comparison to previous observational studies

Zheng *et al.* (1997) used ERS-1 scatterometer data to calculate the surface wind divergence in the Pacific during the 1992-1994 time period. Their results (figure 2) show that the surface wind at 120° W is convergent on the equator during the boreal spring of 1992, but divergent in 1993 and 1994. Short periods of surface wind convergence south of the equator, coincident with the warm season, are present during all years. The surface wind divergence reported by Zheng *et al.* (1997) looks very similar to the OLR and TPW latitude-time plots in Figure 5.2 and Figure 5.3 indicating that the surface wind divergence field is coincident with the presence or absence of a double ITCZ.

Fu *et al.* (1994) used ISCCP cloud data, NMC radiosonde data, The Florida State University surface wind data, and Climate Analysis Center (Reynolds) SST data to infer deep convection dependencies on vertical buoyancy profiles, CAPE, and surface wind divergence in a monthly mean sense. Their results show that when the SST > 28 °C, the presence of deep convective cloud is enhanced 80% (50%) of the time in the western (eastern) Pacific when the surface wind divergence is less than $-5.0 \cdot 10^{-6}$ s^{-1} and 90% (55%) of the time when the surface wind divergence is greater than $-5.0 \cdot 10^{-6}$ s^{-1} and less than $5.0 \cdot 10^{-6}$ s^{-1}. Furthermore, when the SST < 27 °C, they show that the presence deep convective cloud is enhanced 5% (35%) of the time in the western (eastern) Pacific when the surface wind divergence is less than $-5.0 \cdot 10^{-6}$ s^{-1}.

The results from the present work are in general agreement with those of Fu *et al.* It should be noted that regions of strong convergence as defined by Fu *et al.* (less than

$-5.0 \cdot 10^{-6}$ s^{-1}) are very small in areal extent in the present work. Since the quality of the winds used by Fu *et al.* and those used here are of marginal reliability due to the paucity of observed data, inferences about the surface convergence should be kept at the qualitative level. The important point about the results obtained by Fu *et al.* and those obtained here is that under the condition of mild large scale convergence, driven by the subtropical high pressure cells, in the equatorial region, in 1996, the SST cold tongue (<26.5 °C) prevented atmospheric convection and hence produced a thin band of locally generated surface wind divergence over the equatorial cold tongue. While on the contrary, in 1997, the absence of the cold tongue (SST > 27 °C) allowed for deep convection under similar large scale surface wind conditions and therefore produced no locally generated surface wind divergence on the equator in the eastern Pacific.

The double ITCZ structure has been observed outside the eastern Pacific. For example, Lin and Johnson (1996) documented a double ITCZ in the central western Pacific during November 1992 using GMS infrared brightness temperatures (their figure 2). Monthly mean Reynolds SST analysis for November 1992 indicates that the SST values were greater than 29.0 °C with no cold tongue present (not shown). The dynamic importance of the large scale wind field in producing a double ITCZ structure in the absence of an equatorial cold tongue (say in the western Pacific) is best illustrated by comparing the mean April and mean November winds for 1996 (Figure 6.5). Since the tropical western Pacific SST exceeds 28.5 °C everywhere, with no equatorial cold tongue, during November 1996, it is the large scale surface wind divergence, and not the sea surface temperature, that is responsible for suppressing convection along the equator and hence is responsible for producing a double ITCZ in the western Pacific as observed in OLR analysis (not shown). SST analysis during April 1996 shows that a very mild cold tongue (28.5 °C on the equator, 29.5 °C off the equator) is present in the western Pacific. Since no large surface wind divergence is observed during April in the NCEP reanalysis,

it is believed that these higher SST values are still capable of producing locally driven surface wind divergence as in the eastern Pacific and consequently a double ITCZ is observed in the OLR data. Comparison of Figure 6.4 with Figure 5.5 and Figure 5.6 and Figure 5.9 illustrate that the same mechanism, large scale surface wind divergence, is responsible for the maintenance of the double ITCZ observed between 140° W and 160° W. The observations presented here show that the double ITCZ can be produced by two distinctly separate forcing mechanisms:

(1.) Large scale surface wind divergence with no locally SST driven surface wind divergence present on the equator, or

(2.) Local scale surface wind divergence driven by the colder equatorial SST in the presence of large scale convergence.

6.3 Comparison to previous theoretical studies

Many theories regarding atmospheric convection and the meridional placement of the ITCZ have been put forward. Pike (1971) used a coupled atmosphere-ocean axially symmetric model to investigate ITCZ position as a function of the meridional SST distribution. He showed that for an SST profile similar to that of the eastern Pacific during a La Niña year warm season, that a double ITCZ formed in his model. However, after days of integration, it collapsed to a single ITCZ on the equator then migrated toward the pole. He attributed the double ITCZ to instability in the model and likened it to a metastable state. Due to the fact that Pike's model was axially symmetric, he was unable to represent the large scale divergence of the surface wind in his model, which shown previously, can be important in determining the ITCZ structure. Since the SST field in his model was similar to that of the eastern Pacific, which has been shown to force a double ITCZ structure until the southern equatorial SST cools, his explanation of the double ITCZ collapse appears to be inconsistent with the present observations.

Charney (1971) used CISK to describe the latitudinal position of the ITCZ. Since this framework is also zonally symmetric, like Pike, Charney is unable to account for surface wind divergence forcing the solution. Therefore, it is not believed that this model could accurately capture the dynamics of the ITCZ across the Pacific domain.

Holton *et al.* (1971) determined that easterly waves were responsible for the meridional placement of the ITCZ. Easterly waves of the mixed Rossby-Gravity wave (n=1) type are found in the present observations. These waves are readily apparent in Time-Longitude plots of cloud ice water averaged from 4° S to 8° S for all three years of the study as shown in Figure 6.6. Figure 6.7 is similar, but focuses in on the post equinoctial time period. The convection south of the equator is observed to be propagating westward during the 1995 post equinoctial period, but static (not propagating) during the 1996 post equinoctial period (Figure 6.7). The double ITCZ structure appears to be unrelated to easterly wave activity during the 1996 post equinox period. Results regarding the importance of easterly waves using the BWRT2 data set are inconclusive, however it is believed that since static convection is observed to be responsible for the double ITCZ structure during 1996, that easterly waves are unnecessary. Observations using the BWRT2 data set show that the easterly waves enhance convection only over ocean surfaces with warmer SSTs. Since the eastern Pacific is forced by large scale mildly convergent winds, it is the SST field which determines the latitude of convection enhanced by these easterly waves.

Lindzen (1974) described how wave-CISK was responsible for the latitudinal position of the ITCZ. Similar arguments to that used discussing the work of Holton *et al.* would indicate that wave-CISK may enhance convection, but only over warmer SST fields, and therefore, itself does not determine the position of the ITCZ.

Lindzen and Nigam (1987) showed that SST gradients were important in forcing low level convergence and hence convection. They state the importance of both SST and

the convergence of the wind, however they stress the importance of SST gradients on creating pressure perturbations and hence low level convergence. Unfortunately, their analysis was done only during the solstice seasons and therefore does not specifically address the double ITCZ in the eastern Pacific. Since the observations of the double ITCZ in the western Pacific indicate that it is produced by large scale divergence (observed SST gradients in the region are weak), it appears that the theory of Lindzen and Nigam would not be able to simulate the ITCZ in the western Pacific. Furthermore, they simulate convergence of the perturbation wind field in the southeastern Pacific where the FGGE data, they used for comparison, indicate a region of strong divergence. From their figure 5, it is obvious that they are not accurately simulating the southeastern subtropical high and therefore are unable to account for the large scale low level wind divergence forcing in the tropics.

Waliser and Somerville (1994) indicate that the position of the ITCZ is dependent on the latitudinal placement of the SST maximum, and that the SST maximum and the ITCZ do not necessarily coincide. In their simulation, using an axially symmetric primitive equation model, they showed that, for an SST distribution that resembled the observed zonally averaged SST but located off the equator, a double ITCZ formed and was present throughout most of the integration. Since this situation is only observed in the western Pacific under large scale surface wind divergence, it is surmised that their model can only represent the that particular situation. Observations in the eastern Pacific under generally convergent wind fields show that a single ITCZ forms and is located near the SST maximum. Since their model is axially symmetric and produces a double ITCZ without an equatorial cold tongue, it is believed that they would not be able to simulate the atmospheric processes in the eastern Pacific region. Due to the large scale forcing of the subtropical high pressure systems, the tropical eastern Pacific tends to be a region of convergence whereas, the tropical western Pacific tends to be a region of divergence.

Therefore, an axially symmetric model is going to be unable to describe the structural features of the ITCZ throughout the Pacific domain.

Numerical simulation of the ITCZ is a tricky business. It has been shown that, in general, most modeling efforts capture some of the features of the ITCZ, but are incapable of accurately simulating the ITCZ during seasonal climate change. The purpose of the previous summary of modeling efforts is not to denigrate those efforts, but to show that each effort has strengths and weaknesses. Furthermore, since the equinoctial periods are the most dynamic and difficult to simulate, it is worth studying those time periods observationally in the hope that some new information may be recognized which would help direct modeling efforts.

Simulation of the ITCZ in coupled ocean-atmosphere general circulation models is troubling. Many state of the art models produce a double ITCZ encompassing the whole planet, or for too many months of the year. This problem is so prevalent in the coupled GCM community that it has been coined the *double ITCZ syndrome* (Ma *et al.*, 1996). Mechoso *et al.* (1995) describe the successes and failures of eleven coupled GCMs in their effort to simulate the year round ITCZ including the most difficult months, April and October. Implications deduced from the present work that may aid the modeling effort are now discussed. Since the present work only involves the eastern and central tropical Pacific during the boreal spring (April), only those aspects of the GCM work will be discussed. First, Mechoso *et al.* compare the SST fields generated by the ocean model to the COADS April monthly mean SST fields (their figure 3). The problem here is that the COADS April monthly mean field never actually exists, it is an average of La Niña and El Niño SST fields which are very different, especially in the eastern Pacific. It appears that some of the models generate an equatorial cold tongue (La Niña) while others do not (El Niño). Since observations from the present work show that the strength of the SST cold tongue and the warmth of the southern equatorial sea surface determines

the presence or absence of a double ITCZ, it is paramount that the ocean component of a coupled GCM simulate the correct SST field. Eastern Pacific tropical rainfall predicted by the GCMs is indicative of the latitudinal position of the ITCZ and varies widely in latitudinal extent between models. Most of the GCMs which produce an equatorial cold tongue during April with a warm southern tropical eastern Pacific do produce a double ITCZ during April (their figure 5) as the present work indicates they should. Due to the fact that the 'observation' for rainfall comparison (in their figure 5), is derived from cloud top temperature, it is not an accurate assessment of the actual precipitation. The primary problem, as stated by Mechoso *et al.*, is that many models produce a double ITCZ for much of the year. Since only the April and October SST fields for the GCMs are presented in their paper, nothing can be inferred about the other ten months of the year from the present work. Only two of the GCMs produce substantial double ITCZs year round. Both of these models (MRI and MPI) have SST values far exceeding those observed in the southeastern tropical Pacific (10° S, 100° W - 150° W). Given the SST distribution in October by these two GCMs it is not surprising that they produce a double ITCZ during October. Mechoso *et al.* concur, stating that the ocean models have serious deficiencies in the eastern Pacific. Until the ocean model in these coupled GCMs accurately simulates the sea surface temperature, both spatially and temporally, the double ITCZ syndrome will continue. Both the earth's atmosphere and the atmospheric component of coupled GCMs have at least one thing in common, they are both very sensitive to the boundary condition of sea surface temperature.

6.4 Hypothesis of the eastern Pacific ITCZ mechanism

For reasons described herein, it is the sea surface temperature that is the primary forcing mechanism which determines the structure of the ITCZ in the eastern Pacific during the boreal spring. It was shown in Figure 6.4 that the large scale surface winds

eastern tropical Pacific are mildly convergent during the post equinoctial period. Given this forcing mechanism by the subtropical highs, it was shown that the SST is the controlling factor in frequency and strength of convection. When the equatorial cold tongue is present, with SST values below 26.5 °C, convection is suppressed along the equator but enhanced over warmer SST regions off the equator. This process is illustrated in Figure 6.8. When the equatorial cold tongue is not present, typically during El Niño years (cf. Figure 5.1 - Figure 5.3 and Figure 5.5), the convection occurs over the warm SST regions across the equator. This situation forms one area of large scale ascent as depicted in Figure 6.9. Immediately following the non-El Niño post equinoctial period, the double ITCZ begins to fade, and the situation is as illustrated in Figure 6.10. The SST in the north continues to warm, and although the southern SST is still warm, it is relatively cooler than that in the north. As a result the convection in the north is stronger in intensity and slightly suppresses convection in the south through large scale subsidence. Finally, near the end of a non-El Niño boreal spring the ITCZ is a single band of convection situated north of the equator as depicted in Figure 6.11. Since the BWRT2 data only extends to 15° N, the strength of the descending branch of this single ITCZ can not inferred north of the equator. However, the work of Hack *et al.* (1989) indicates that the southern cell, with cross equatorial flow, runs stronger than the northern cell. The impact of the time varying SST on the tropical general circulation was explored using a variety of observations. The reason for the seasonal march of SST was beyond the scope of this work, but is a research topic of current interest.

Table 6.1. Comparison of NCEP and TAO wind fields.

	RMS(NCEP-TAO) [m s^{-1}]	Mean(ABS(TAO)) [m s^{-1}]	RMS/Mean*100 [%]
U	0.6 - 0.9	4.0	15-22
V	1.0 - 1.5	2.0	50-75
$(U^2+V^2)^{1/2}$	0.6 - 1.2	5.0	12-24

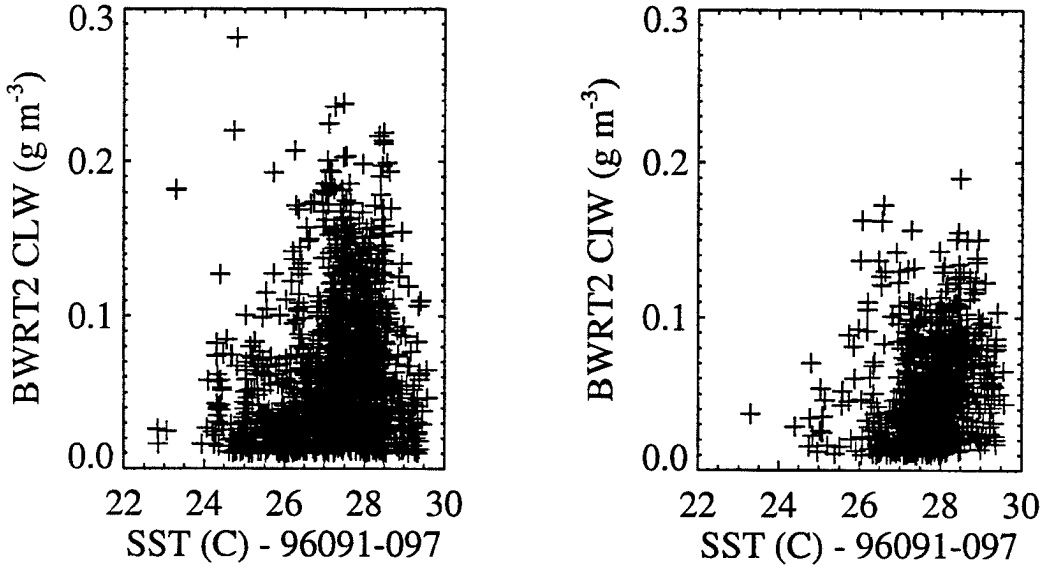

Figure 6.1. Scatter plots of cloud liquid water content versus SST and cloud ice water content versus SST during first week in April, 1996, for the entire BWRT2 region.

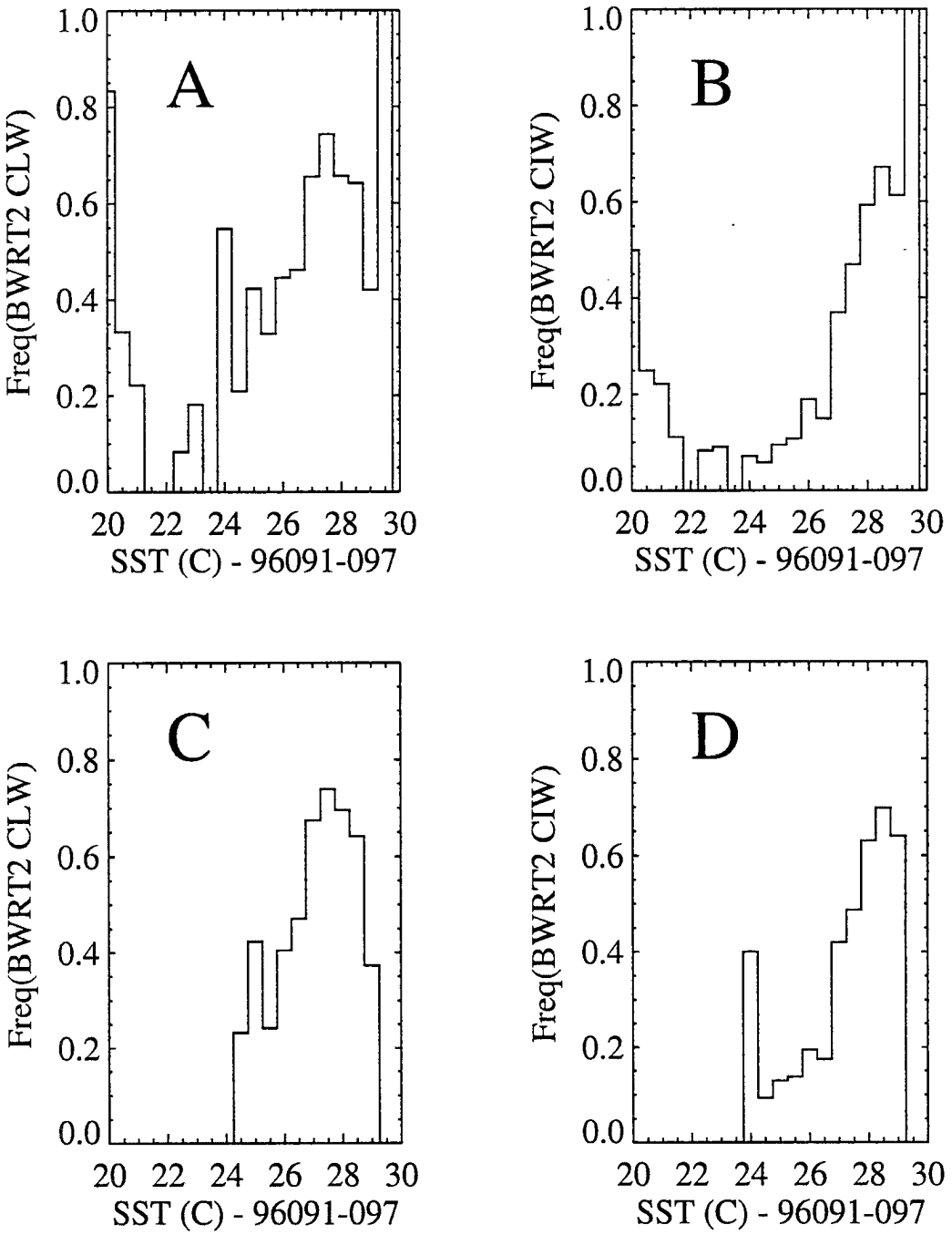

Figure 6.2. Cloud liquid water frequency-SST histogram (CLW > 0.02 g m^{-3}) and cloud ice water frequency-SST histogram (CIW > 0.02 g m^{-3}) during the first week of April 1996, for entire BWRT2 region (A&B) and for BWRT2 region west of 100° W (C&D).

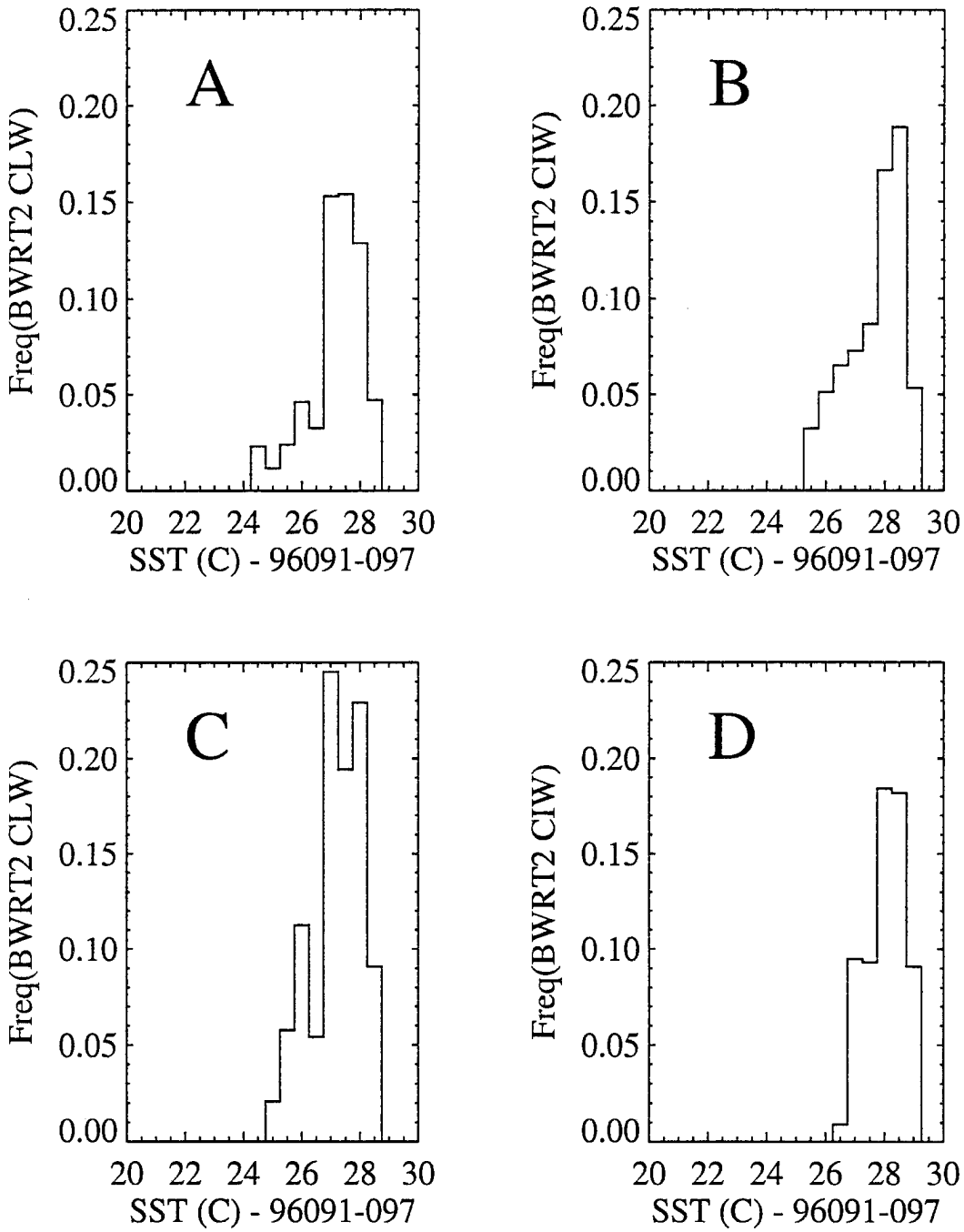

Figure 6.3. Cloud liquid water frequency-SST histogram (CLW > 0.10 g m^{-3}) and cloud ice water frequency-SST histogram (CIW > 0.08 g m^{-3}) during the first week in April 1996, for the BWRT2 region west of 100° W (A&B) and for the BWRT2 region west of 100° W between 8° N and 8° S (C&D).

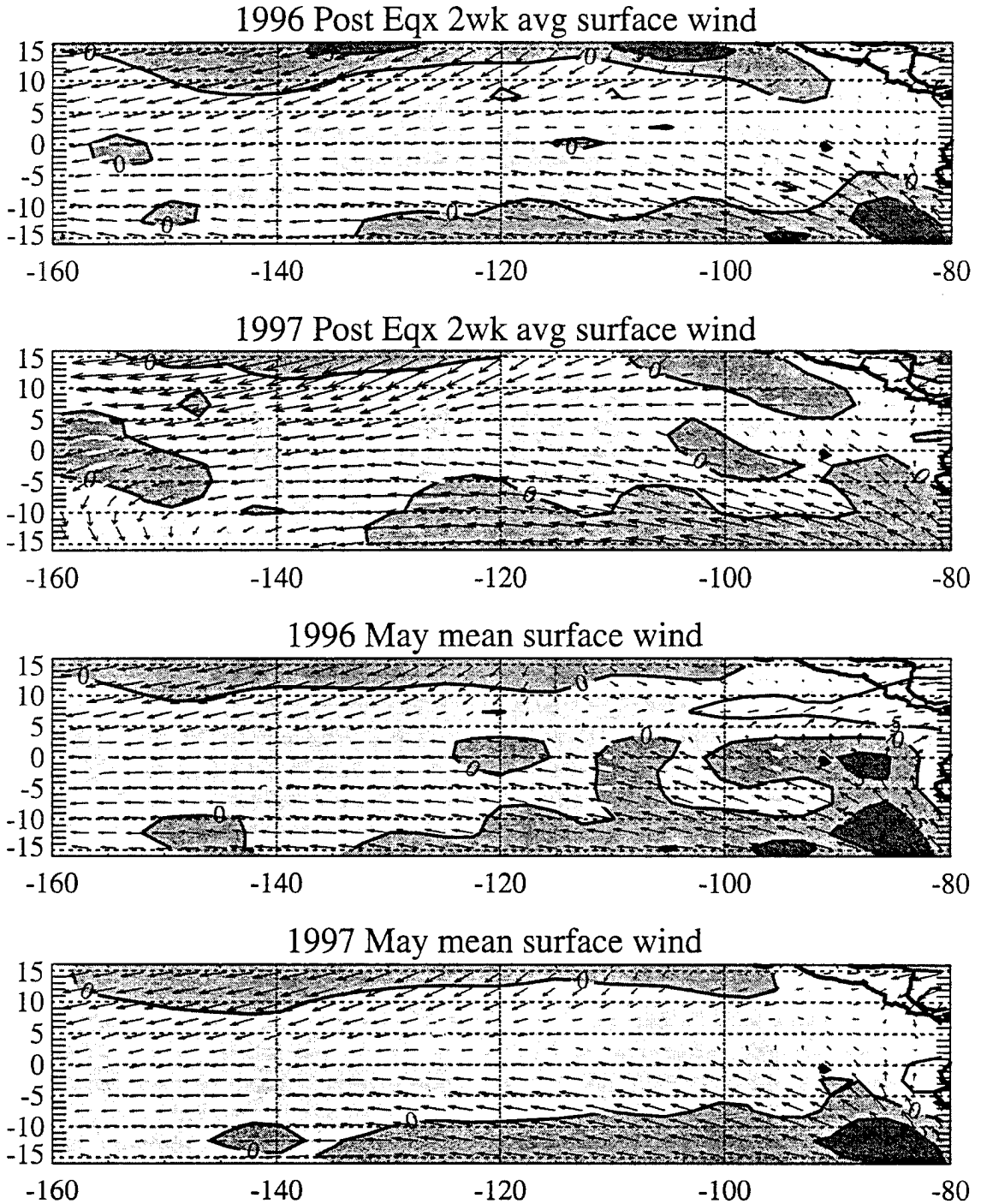

Figure 6.4. Surface winds (max. vec. = 10.9 m s^{-1}) and divergence (x10^{-6} s^{-1}) for the post equinox two week average (top) and for the May mean (bottom). TAO buoy winds for the same time period are overlaid in white.

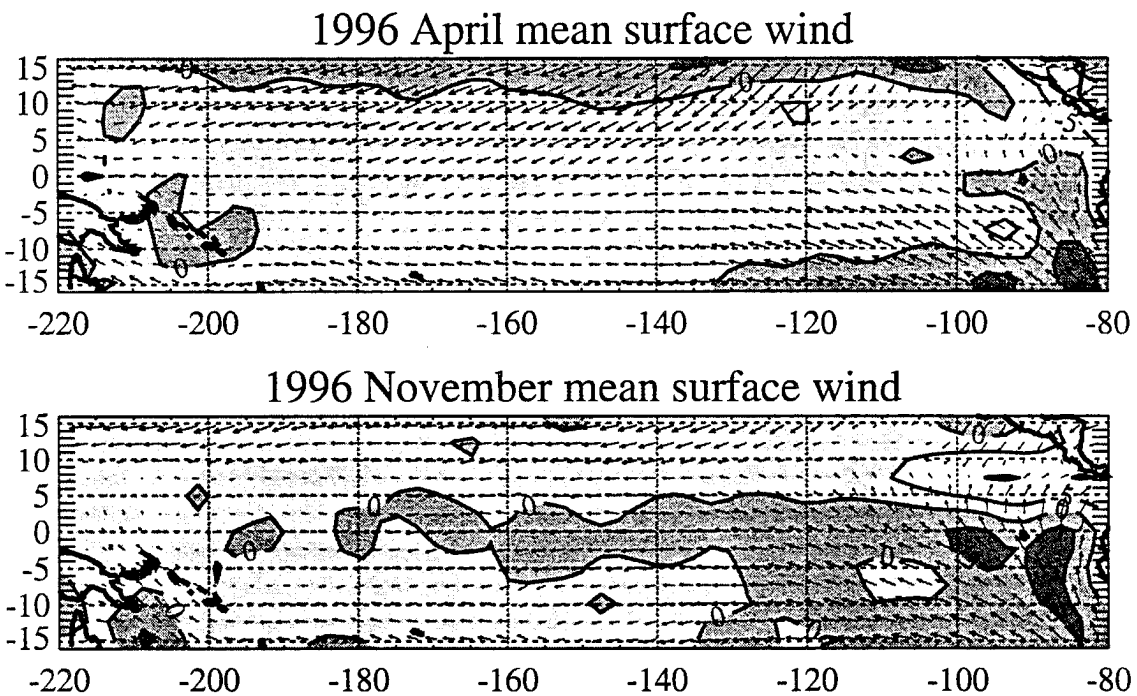

Figure 6.5. Surface winds (max. vec. = 11.5 m s^{-1}) and divergence (x10^{-6} s^{-1}) for the April and November 1996 means.

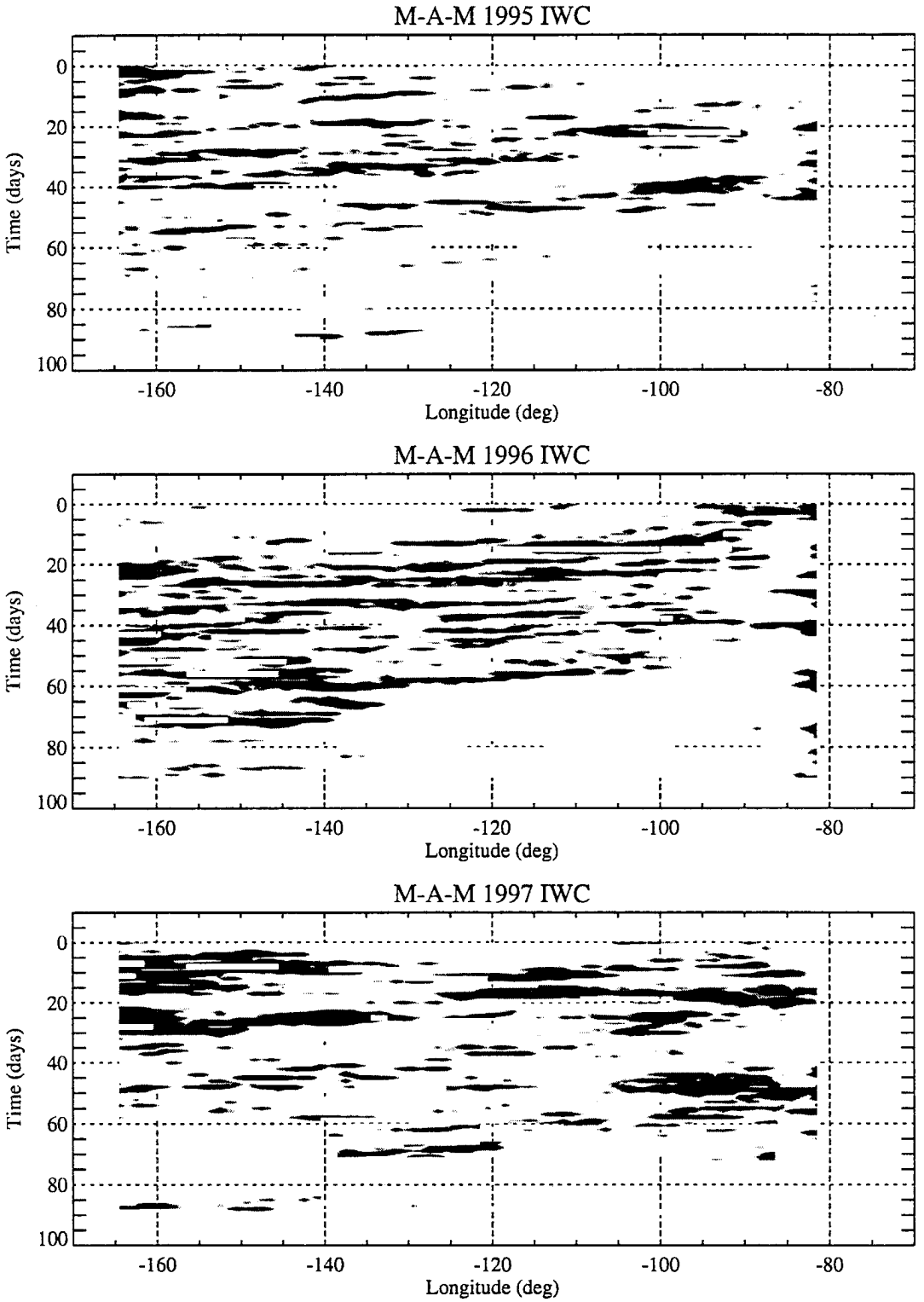

Figure 6.6. Time-Longitude plots of cloud ice water content for MAM 1995, 1996, 1997 averaged over the 4° - 8° S latitude band. Gray shading from 0.01 to 0.05 g m^{-3}.

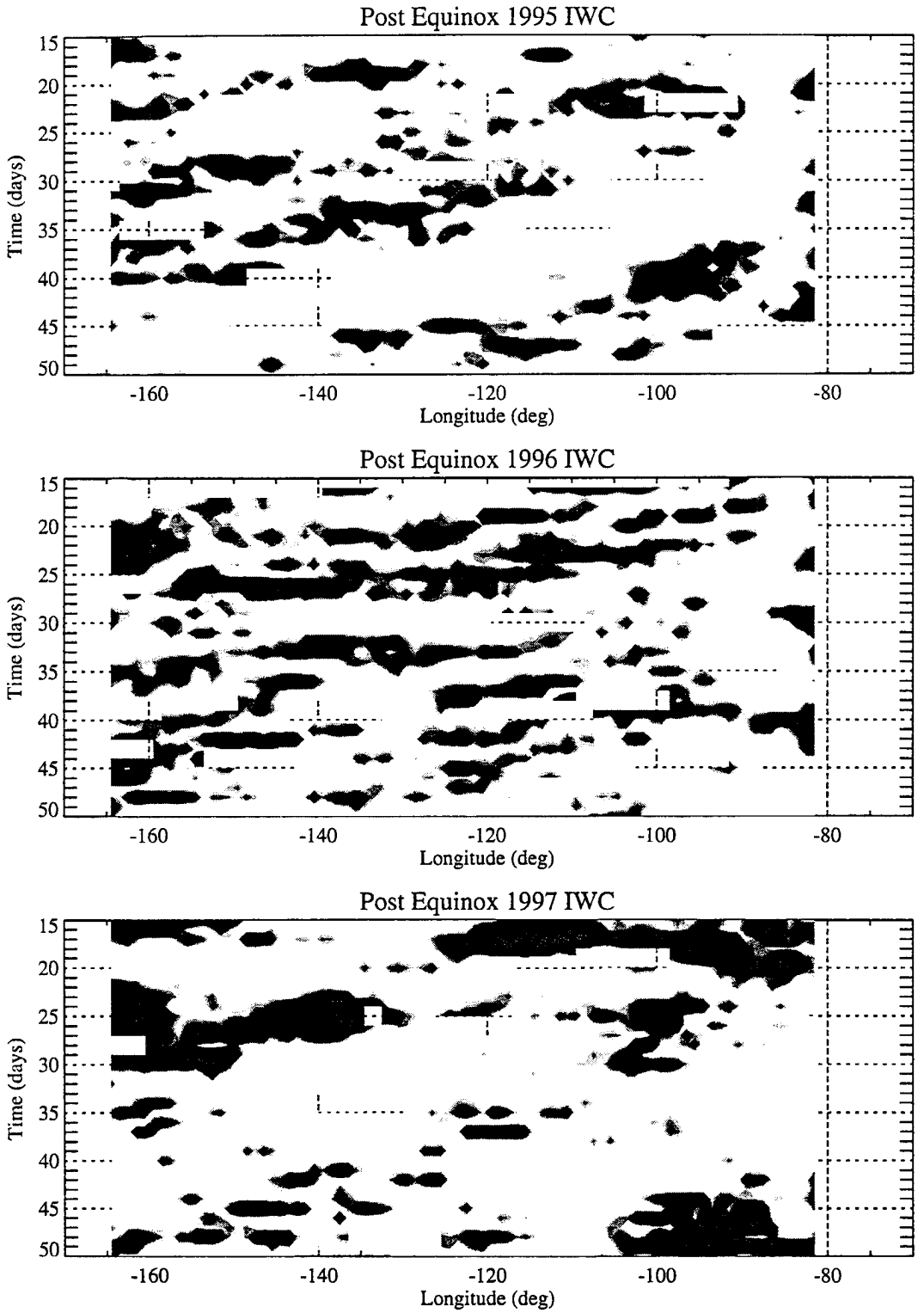

Figure 6.7. Time-Longitude plots of cloud ice water content for the post equinoctial period 1995, 1996, 1997 averaged over the 4° - 8° S latitude band. Gray shading from 0.01 to 0.05 g m^{-3}.

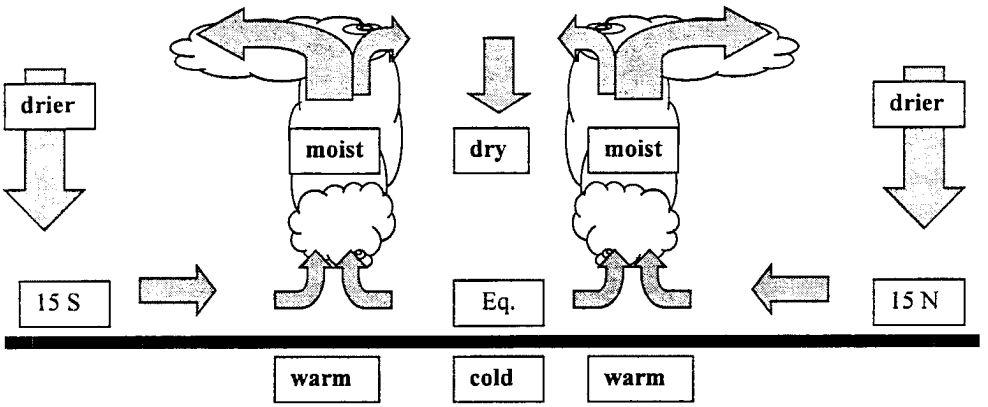

Figure 6.8. Illustration of the primary mechanisms determining the structure of the eastern Pacific ITCZ during a La Niña boreal spring.

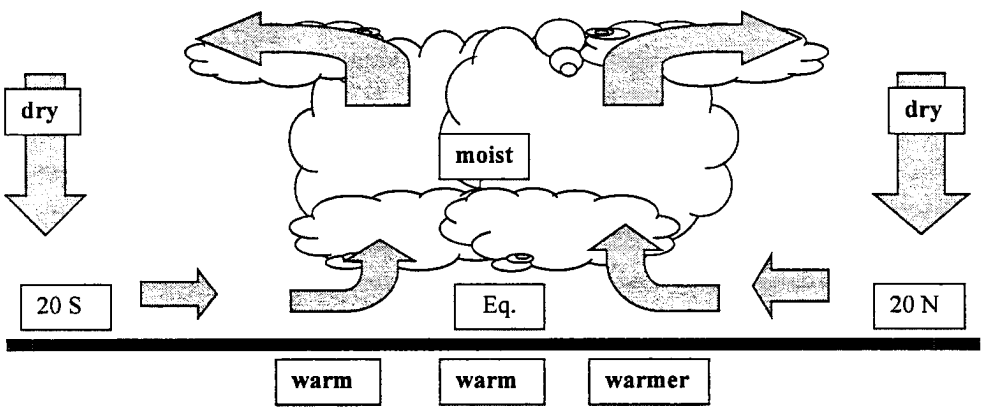

Figure 6.9. Illustration of the primary mechanisms determining the structure of the eastern Pacific ITCZ during an El Niño boreal spring.

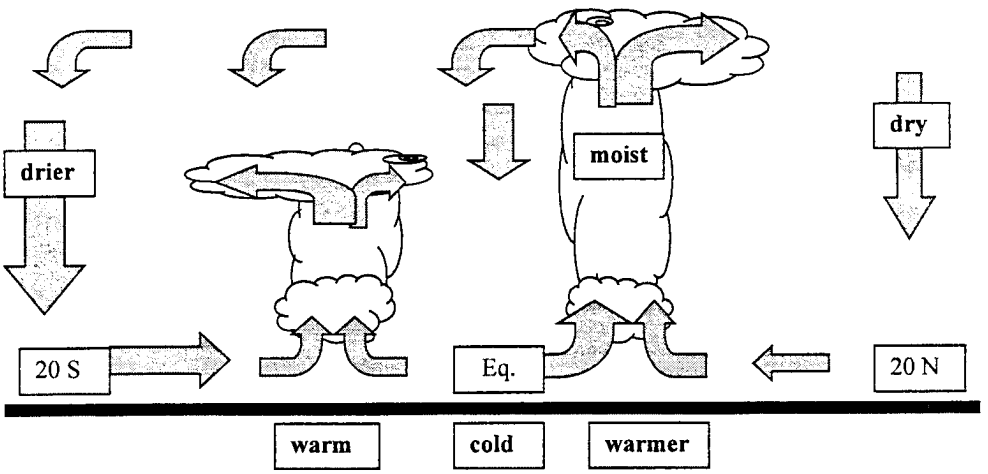

Figure 6.10. Illustration of the primary mechanisms determining the structure of the eastern Pacific ITCZ during a La Niña boreal spring when the northern equatorial SST is warmer than the southern equatorial SST.

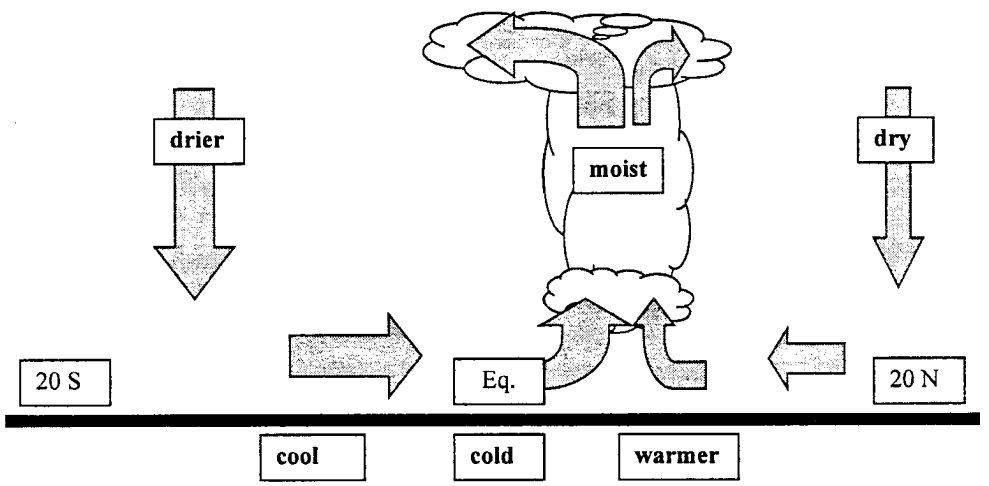

Figure 6.11. Illustration of the primary mechanisms determining the structure of the eastern Pacific ITCZ at the end of a La Niña boreal spring when the northern equatorial SST is warm and the southern equatorial SST is cool.

7 Conclusion

An algorithm, based on the application of Bayes theorem, to retrieve water vapor and cloud water profiles from satellite radiances was described and then evaluated using radiosonde data. Climatological statistical information derived from other sensors was used to constrain the inversion. SSM/T-2 microwave sounder and GOES-8 infrared imager satellite radiances were used together to retrieve moisture profiles over continental and oceanic surfaces. Comparisons of retrieved and radiosonde measured relative humidity profiles indicate that the use of the infrared imager radiances improves retrievals in cloudy skies under some conditions. However, the combined microwave-infrared retrieval method did poorly near the Barbados radiosonde site in the Caribbean. Since the microwave-only method performed quite satisfactorily in the Caribbean, it is believed that the BWR algorithm was unable to model infrared optically thin clouds properly, resulting in poor cloud top height assignment and therefore poor overall retrieval performance.

Upon completion of the evaluation process, an application for the algorithm was necessary to illustrate its usefulness. To maximize the usefulness of satellite retrieved moisture profiles while minimizing errors in those profiles, a tropical oceanic environment was chosen. Based on results from the radiosonde comparisons, the BWR algorithm was used in the microwave-only mode to retrieve relative humidity profiles and cloud water information. The application was to investigate the spatial and temporal structure of the intertropical convergence zone in the eastern Pacific during the boreal spring. The BWR algorithm used SSM/T-2 radiances and NCEP/NCAR temperature

analyses to produce a data set (BWRT2) of relative humidity profiles and cloud liquid and ice water contents for three seasons (March - May, 1995 - 1997). These daily fields, averaged to a one degree latitude-longitude grid, were used along with other observational and model derived analyses to investigate the processes responsible for the occurrence of a double ITCZ in the eastern Pacific.

The BWRT2 data were used to document the frequency and strength of atmospheric convection in the eastern tropical Pacific region. Along with the BWRT2 data, outgoing long wave, total precipitable water, surface wind field, and sea surface temperature analyses were used to infer the convection forcing mechanisms which determine the structure of the ITCZ. The surface wind data indicated that the equatorial eastern Pacific is a region of large scale mass convergence during the boreal spring. Comparisons of convection frequency and sea surface temperatures indicated that the equatorial cold tongue is responsible for the suppression of convection on the equator. Furthermore, it was shown that when the sea surface was sufficiently warm off the equator with an equatorial cold tongue present, a double ITCZ formed. The double ITCZ, a cloud structure quasi-symmetrically located about the equator at about 6° N and 6° S, exists during the post equinoctial period for approximately two weeks. As the SST north of the equator warms, so does the strength of the northern ITCZ. The southern ITCZ begins fade under increased subsidence before the disappearance of the warm southern equatorial SST. Since the eastern Pacific is observed to be a region of large scale mass convergence, it is the presence or absence of the equatorial SST cold tongue which determines whether or not a double ITCZ will form. Generally, it is observed that the cold tongue is weak or absent during El Niño years while it is strongly present during La Niña years. Therefore, no double ITCZ structure in the cloud field is observed during El Niño years while very well defined double ITCZ structures are observed during La Niña years. Double ITCZs have been observed in the western Pacific during the austral

spring. It was shown that a different forcing mechanism is responsible for the presence of the double ITCZ over the western Pacific warm pool. The sea surface temperature in the equatorial western Pacific is observed to be greater than 28.5 °C everywhere. Observed large scale divergence of the surface wind field is shown to be coincident with the observation of a double ITCZ in the western tropical Pacific. Thus, in the eastern Pacific it is the sea surface temperature which determines the presence of the double ITCZ, whereas in the western Pacific it is the large scale low level mass divergence which determines the presence of the double ITCZ. Since these two forcing mechanisms are zonally varying, it is not possible to simulate the spatial structure of the ITCZ in an axially symmetric numerical model. The erroneous presence of a double ITCZ in coupled atmosphere-ocean general circulation models was discussed. The coupled GCM modelers believe that poor simulation of the SST field is responsible for non-realistic ITCZ behavior within these coupled models. The observations made here regarding the presence or absence of the double ITCZ tend to support their conclusions. The application of a satellite remote sensing algorithm in the data sparse tropical eastern Pacific was shown to aid an observational study of the forcing mechanisms responsible for the spatial and temporal structure of the ITCZ.

The work presented here has illustrated the need for a variety of future research. Combining data from an infrared imager with a microwave sounder to retrieve water vapor profiles in the presence of clouds achieved limited success. The simplistic infrared radiative transfer modeling of clouds is believed to be responsible for the poor performance in some cases. This shortfall resulted in inaccurate cloud height assignment and overall poor retrieval performance. It is believed that using an infrared sounder with several spectral bands would greatly improve the ability to model optically thin clouds and therefore improve retrieval performance over a microwave only method.

As part of the algorithm evaluation, the natural temporal variability of the relative humidity profile was measured using ARM radiosonde data. It was shown that the temporal variability of the profile greatly affected the algorithm validation results. As part of the effort to launch future satellite borne remote sensors, a comprehensive validation study data set must be produced. This data set should include temporally and spatially collocated data from all *in situ* and remote sensors available. The advancement of the science of atmospheric remote sensing is greatly impeded by not producing these comprehensive validation data sets.

The SSM/T-2 microwave moisture sounder is a very capable but under utilized instrument. The SSM/T-2 has been in orbit continuously since 1991, however few papers have been published illustrating its profiling capabilities. Furthermore, observational studies using retrieved moisture profiles from SSM/T-2 radiances has failed to appear in the literature. The work presented here is just one example of how the SSM/T-2 can be used to further our knowledge of atmospheric moisture processes and thus the earth's climate system in general.

8 References

Alpert, L., 1945, The intertropical convergence zone of the eastern Pacific region (I), *Bull. Amer. Meteor. Soc.*, **26**, 426-432.

Chahine, M. T., 1992: The hydrological cycle and its influences on climate, *Nature*, **359**, 373-380.

Charney, J., 1971: Tropical cyclogenesis and the formation of the intertropical convergence zone, *Mathematical Problems of Geophysical Fluid Dynamics, Lectures in Applied Mathematics, Vol. 13, W. H. Reid, Ed., Amer. Math. Soc.*, 355-368.

Coughlan, M., and R. Avissar, 1996: The Global Energy and Water Cycle Experiment (GEWEX) Continental-Scale International Project (GCIP): an overview, *J. Geophys. Res.*, **101**(D3): 7139-7147.

Deeter, M. N. and K. F. Evans, 1997: A hybrid Eddington-single scattering radiative transfer model for computing radiances from thermally emitting atmospheres, Submitted to *J. Quant. Spectosc. Radiat. Transfer.*

Deser, C. and J. M. Wallace, 1990: Large-scale atmospheric circulation features of warm and cold episodes in the tropical Pacific, *J. Climate*, **3**, 1254-1281.

Evans, K. F., J. Turk, T. Wong, G. L. Stephens, 1995a: A Bayesian approach to microwave precipitation profile retrieval. *J. Appl. Meteor.*, **34**, 260-279.

Evans, K. F., and G. L. Stephens, 1995b: Microwave radiative transfer through clouds composed of realistically shaped ice crystals. Part I: Single scattering properties, *J. Atmos. Sci.*, **52**, 2041-2057.

Eyre, J. R., 1989: Inversion of cloudy satellite sounding radiances by nonlinear optimal estimation: application to TOVS data, *Q. J. R. Meteorol. Soc.*, **115**, 1027-1037.

Eyre, J. R., 1990: The information content of data from satellite sounding systems: A simulation study. *Q. J. R. Meteorol. Soc.*, **116**, 401-434.

Falcone, V. J., and co-authors, 1992: SSM/T-2 calibration and validation data analysis, Phillips Laboratory Technical Report 92-2293.

Fernandez-Partagas, J., and M. A. Estoque, 1985: Characteristics of the ITCZ over the eastern Pacific, 5-8 June 1979, *Mon. Weather Rev.*, **113**, 99-105.

Fu, R., A. D. Del Genio, and W. B. Rossow, 1994: Influence of ocean surface conditions on atmospheric vertical thermodynamic structure and deep convection, *J. Climate*, 7, 1092-1108.

Garcia, O., 1985: Atlas of highly reflective clouds for the global tropics: 1971-1983, *U. S. Dept. of Commerce, NOAA, Environmental Research Lab, Boulder, Co*, 365 pp. [NTIS PB-87129169].

Greenwald, T. J., G. L. Stephens, T. H. Vonder Haar, and D. L. Jackson,1995: A physical retrieval of cloud liquid water over the global oceans using Special Sensor Microwave/Imager (SSM/I) observations, *J. Geophys. Res.*, **98**, D10: 18471-18488

Greenwald, T. J., S. A. Christopher, and J. Chou, 1997: SSM/I and GOES-8 imager comparisons of cloud liquid water path over water: Assessment of sub-field of view effects in microwave retrievals, *J. Geophys. Res.*, **102**, 19585-19596.

Grody, N.C., 1988: Surface identification using satellite microwave radiometers, *IEEE Trans. Geosci. Remote Sensing*, **26**, 850-859.

Gruber, A., 1972: Fluctuations in the position of the ITCZ in the Atlantic and Pacific Oceans, *J. Atmos. Sci.*, **29**, 193-197.

Gutzler, D. S., and T. M. Wood, 1990: Structure of large-scale convective anomalies over tropical oceans, *J. Climate*, **3**, 483-496.

Hack, J. J., W. H. Schubert, D. E. Stevens, and H. Kuo, 1989: Response of the Hadley circulation to convective forcing in the ITCZ, *J. Atmos. Sci.*, **46**, 2957-2973.

Holton, J. R., J. M. Wallace, and J. A. Young, 1971: On boundary layer dynamics and the ITCZ, , *J. Atmos. Sci.*, **28**, 275-280.

Hubert, L. F., A. F. Krueger, and J. S. Winston, 1969: The double intertropical convergence zone— Fact or fiction?, *J. Atmos. Sci.*, **26**, 771-773.

Jones, A. S., K. E. Eis, T. H. Vonder Haar, 1995: A method for multisensor-multispectral satellite data fusion. *J. Atmos. Oceanic Technol.*, **12**, 739-754.

Kakar, R. K., 1983: Retrieval of clear sky moisture profiles using the 183 GHz water vapor line, *J. Climate Appl. Meteor.*, **22**, 1282-1289.

Kashiwagi, K., 1987: On the impact of space-based observing systems in the JMA global forecast/analysis system, *J. Meteor. Soc. Japan*, **65**, 189-220.

Kornfield, J., A. F. Hasler, K. J. Hanson, and V. E. Suomi, 1967, Photographic cloud climatology from ESSA III and V computer produced mosaics, *Bull. Amer. Meteor. Soc.*, **12**, 878-883.

Kratz, D. P., 1995: The correlated k-distribution technique as applied to the AVHRR channels, *J. Quant. Spectrosc. Radiat. Transfer*, **53**, 501-518.

Kuo, C. C., D. H. Staelin, and P. W. Rosenkranz, 1994: Statistical iterative scheme for estimating atmospheric relative humidity profiles,
IEEE Trans. Geosci. Remote Sensing, **32**, 254-260.

Lau, K.-M., H.-T. Wu, and S. Bony, 1997: The role of large-scale atmospheric circulation in the relationship between tropical convection and sea surface temperature, *J. Climate*, **10**, 381-392.

Liebe, H. J., 1989: MPM – An atmospheric millimeter wave propagation model, *Int. J. Infrared and Millimeter waves*, **10**, 631-650.

Lin, X. and R. H. Johnson, 1996: Kinematic and thermodynamic characteristics of the flow over the western Pacific warm pool during TOGA COARE,
J. Atmos. Sci., **53**, 695-715.

Lindzen, R. S., 1974: Wave-CISK in the tropics, *J. Atmos. Sci.*, **31**, 156-179.

Lindzen, R. S. and S. Nigam, 1987: On the role of sea surface temperature gradients in forcing low-level winds and convergence in the tropics, *J. Atmos. Sci.*, **44**, 2418-2436.

Lutz, R., T. T. Wilheit, J. R. Wang, and R. K. Kakar, 1991: Retrieval of water vapor profiles from microwave radiometric measurements near 90 and 183 GHz,
IEEE Trans. Geosci. Remote Sensing, **29**, 602-609.

Ma, C-C, C. R. Mechoso, A. W. Robertson, A. Arakawa, 1996: Peruvian stratus clouds and the tropical Pacific circulation: a coupled ocean-atmosphere GCM study,
J. Climate, **9**, 1635-1645.

Mechoso, C. R. and co-authors, 1995: The seasonal cycle over the tropical Pacific in coupled ocean-atmosphere general circulation models,
Mon. Weather Rev., **123**, 2825-2838.

Mitchell, T. P. and J. M. Wallace, 1992: the annual cycle in equatorial convection and sea surface temperature, *J. Climate*, **5**, 1140-1156.

Mo, K. C., X. L. Wang, R. Kistler, M. Kanamitsu, and E. Kalnay, 1995: Impact of satellite data on the CDAS-Reanalysis system, *Mon. Weather Rev.*, **123**, 124-139

Muller, B. M., H. E. Fuelberg, and X. Xiang, 1994: Simulations of the effects of water vapor, cloud liquid water, and ice on AMSU moisture channels brightness temperatures, *J. Appl. Meteor.*, **33**, 1133-1154.

Musk, L. F., 1976: Rainfall variability and the Walker cell in the equatorial Pacific Ocean, *Weather*, **31**, 34-47.

Philander, S. G. H., D. Gu, D. Halpern, G. Lambert, N-C. Lau, T. Li, R. C. Pacanowski, J., 1996: Why the ITCZ is mostly north of the equator, *J. Climate*, **9**, 2958-2972.

Pike, A. C., 1972: The intertropical convergence zone studied with an interacting atmosphere and ocean model, *Mon. Weather Rev.*, **99**, 469-477.

Press, W. H., S. A. Teukolsky, W. T. Vetterling, B. P. Flannery, 1992: *Numerical Recipes in FORTRAN: the art of scientific computing.* Cambridge University Press, UK.

Randel, D. L., T. H. Vonder Haar, M. A. Ringerud, G. L. Stephens, T. J. Greenwald, and C. L. Combs, 1996: A new global water vapor data set, *Bull. Amer. Meteor. Soc.*, **77**, 1233-1246.

Rodgers, C. D., 1990: Characterization and error analysis of profiles retrieved from remote sounding measurements, *J. Geophys. Res.*, **95**, D5: 5587-5595.

Stephens, G. L. and T. J. Greenwald, 1991: The Earth's radiation budget and its relation to atmospheric hydrology. Part 1: Observations of the clear sky greenhouse effect, *J. Geophys. Res.*, **96**, 15311-15324.

Waliser, D. E., and C. Gautier, 1993: A satellite-derived climatology of the ITCZ, *J. Climate*, **6**, 2162-2174.

Waliser, D. E. and R. C. J. Somerville, 1994: Preferred latitudes of the intertropical convergence zone, *J. Atmos. Sci.*, **51**, 1619-1639.

Wang, J. R., S. H. Melfi, P. Racette, D. N. Whiteman, L. A. Chang, R. A. Ferrare, K. D. Evans, and F. J. Schmidlin, 1995: Simultaneous measurements of atmospheric water vapor with MIR, Raman lidar, and rawinsondes, *J. Appl. Meteor.*, **34**, 1595-1607.

Wilheit, T. T., 1990: An algorithm for retrieving water vapor profiles in clear and cloudy atmospheres from 183 GHz radiometric measurements: Simulation studies, *J. Appl. Meteor.*, **29**, 508-515.

Winston, J. S., 1971: The annual course of zonal mean albedo as derived from ESSA 3 and 5 digitized picture data, *Mon. Weather Rev.*, **99**, 818-827.

Zheng, Q., X.-H. Yan, W. T. Liu, W. Tang, D. Kurz, 1997: Seasonal and interannual variability of atmospheric convergence zones in the tropical Pacific observed with ERS-1 scatterometer, *Geophys. Res. Letters*, **24**, 261-263.